UNIVERSITÀ DEGLI STUDI DI PAVIA

DOTTORATO IN SCIENZE CHIMICHE E FARMACEUTICHE E INNOVAZIONE INDUSTRIALE
(XXXIII Ciclo)

Coordinatore: Chiar.mo Prof. Giorgio Colombo

Design and application of multifunctional, non-wetting smart surfaces

Tesi di Dottorato di
Giulio Boveri

AA 2019/2020

Tutor
Chiar.mo Prof. Vittorio Berbenni

Co-tutor
Chiar.ma Dott.ssa Mariarosa Raimondo

Summary

Abstract

Ice nucleation and accretion lead to multiple problems such as freezing of the streets which can cause traffic collisions or people injuries, collapse of high voltage power lines leading to black-out and icing of aircraft components causing major aeronautic accidents. The most widespread strategies for the removal of accumulated ice layers result in most cases expensive, time-consuming and hazardous for the environment. In this thesis I present the design of hydrophobic hybrid inorganic-organic coatings via Lotus leaf-like and Slippery Liquid Infused Porous Surfaces (SLIPS) approaches with reduced, lasting wetting performance in cold environments. Static and dynamic wetting behavior has been evaluated at room and sub-zero temperatures. The main target was the selection of the most suitable design approaches and formulations of coatings to be applied on metals or alloys when the contact time between the droplet and the material surface has to be minimized or the adhesion of ice has to be decreased. In the temperature range from -10 to 0°C, an evidence of a stable hydrophobicity and a low water contact angle hysteresis (below 15°) of all the SLIPS developed is reported.

Moreover, this work includes the evaluation of the icing nucleation delay and the ice adhesion force of the designed coatings. Surfaces with anti-wetting behavior infused in lubricant oils exhibited a consistent increase of ice nucleation delay time if compared with bare substate and a huge decrease of ice adhesion force, even if compared with commercially available anti-

wetting products (i.e PTFE). In conclusion, designed samples are characterized in Icing Wind Tunnel to simulate the impact of supercooled drops on the designed anti-wetting materials. The achieved results confirmed the efficiency of the SLIP surfaces in glaze ice regime, with a consistent decrease of ice accumulation with respect the base substrate.

SLIPS also achieved good performance stability during freeze/and frost/thaw durability cycles stood out as a key issue for further development at larger scale.

1.Introduction

1.1 Anti-wetting state

The repellence towards liquids is a key aspect of materials engineering, finding applications in many industrial fields such as aeronautic, naval, energetic, etc.

The typical way used in the past years to obtain superhydrophobic (SH) surfaces is to mimic the behavior of the Lotus Leaf.

Many scientists and industries attempted to recreate water repellence on different surfaces, especially on textiles. Furthermore, authors like Wenzel [1], Cassie and Baxter [2] published their theories between the 1930s and the 1940s, hinting at the role of roughness and surface structure in wetting. However, a deeper light was shed on this topic only in the paper published by Barthlott and Ehler [3]. They studied the surface morphology of the lotus leaf surface with a Scanning Electron Microscope (SEM), revealing a peculiar structure [4]. Bumps called papillae, about 10-20 μm tall and 10- 15 μm wide, uniformly covered the surface. At higher magnifications, nano-scale epicuticular waxes were observed on papillae surface. As described below in this chapter, such dual-scale, hierarchical structures are crucial for the achievement of the property of repelling water. The morphology of the lotus leas is shown in Figure 1:

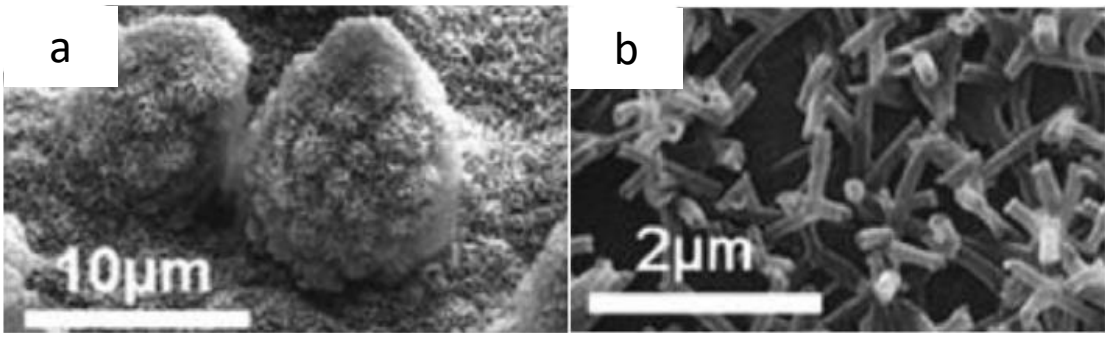

Figure 1. SEM image of microbumps which cover the lotus leaf (a). High magnification (b) exhibits the presence of nanopapillae covering the microbumps [4].

The replication of the lotus leaf morphology and behavior has been a big challenge for different research groups all over the world.

As described before hierarchical structure plays a key role in the formation of a stable Cassie-Baxter wetting regime, able to trap pockets air between the nano-features. The entrapment of the air avoids the surface wetting if coupled with a chemical modification able to decrease the Surface-Energy. The schematization of Cassie-Baxter wetting state is shown in Figure 2:

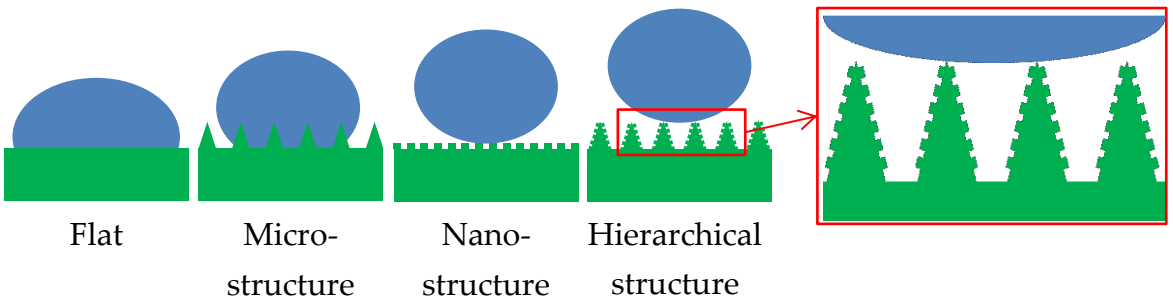

Figure 2. Schematization of the hierarchical micro-nanostructure typical of the Cassie-Baxter wetting state

The water drops floated on the surfaces supported by the air bubbles which are trapped in the structure.

Typically, a superhydrophobic surface has Water contact angle (WCA) higher than 150° and Contact angle Hysteresis (CAH) lower than 10° which means a high mobility of the drops on it, with no sticking phenomenon appearance. WCA and CAH will be described in the next chapters of this thesis.

In order to achieve the proper morphology on the surfaces there are two types of approaches for the structuration [5]. The first one is a top-down approach, in which the surface of the starting substrate is modified by subtraction of material.

Typical examples are lithographic processes [6–8] and techniques based on templates utilization [9]. Also etching is considered as top-down approach and can be carried out by plasma treatment [10,11] or by chemical attack [12–14]. This process is really interesting for the industrial transfer due to the easy method and the low cost needed to reach superhydrophobic behavior.

The second approach used to fabricate anti-wetting materials is a bottom-up approach which starts from molecules able to self-organize or self-assemble on the bare substrate giving different morphologies needed for the anti-wetting property achievement. Usually bottom-up approaches include the fabrication of structured coating that transfers its properties to the substrate. The scientific community devoted huge efforts to the optimization of adhesion, which can be improved by adding a primer layer [15] or creating

chemical bonds between the substrate and the coating [16]. The literature reports countless attempts of superhydrophobic coatings. Some of the used techniques include electrospinning [17], sol-gel [15,18,19], Layer-by-Layer assembly (LbL) [20,21], anodization [22], electrochemical processes [23,24], chemical vapor deposition [25,26] and deposition of colloids or composites [27–29].

After the physical surface modification, the substrates get the proper structure able to achieve a stable Cassi-Baxter wetting state but to repel liquids the decrease of the surface energy is needed. Many authors report successful modification of metal oxides with fatty acids [22,30] or thiols [31]. However, the interaction between these molecules and the oxides is often too weak, causing poor chemical and mechanical resistance. Meanwhile, silanes proved to be extremely effective in forming a strong bond with oxides [32], therefore providing more resistant hydrophobization [33]. Fluoroalkylsilanes (FAS), e.g. fluorine-substituted alkylsilanes, establish excellent superhydrophobic properties [13]. The grafting of the fluorine rich molecules results very easy and reproducible for statistical studies, coupled with the low cost of the FAS solution, usually prepared in isopropanol with standard concentration.

The chemical modification leads to surfaces with surface energy close to 0 mN/m which means a complete repelling of liquids.

Another way to obtain superhydrophobic surfaces is the chemical modification of the ceramic oxide nanoparticles with silane-based

compounds. In the last years, a common approach is the grafting of silane molecules on Silica Nanoparticles[34,35]. The deposition of the functionalized NPs results one-step, avoiding the conventional multi-step processes needed to achieve hybrid inorganic organic multi layers on the substrate. The direct NPs modification finds interest in the industry due to the gain of time and especially to the reduction of the process cost.

When practical applications for SH materials are taken into account, the main hindrance is generally represented by their durability since under abrasion, erosion or other severe conditions the peculiar structural features might be easily destroyed [36–38], allowing water drops to penetrate into the structure annihilating the Cassie-Baxter wetting state with a consequent loss of the anti-wetting behavior. Moreover, in environments with high relative humidity, condensation of tiny water drops can occur between the surface features of SH surfaces, again leading to the disruption of the Cassie-Baxter wetting state [39].

In order to overcome the issues connected to the structural weakness of Lotus leaf-like surfaces, in the last years many studies considered new design approaches and, among them, the one leading to the Slippery Liquid Infused Porous Surfaces (SLIPS) [40]. SLIPS are inspired on the behavior of the Nephentes pitcher plant [41] which presents an anti-adhesive layer on its walls, used to slip the insects directly into the mouth. These innovative surfaces are based on the infusion of a liquid, e.g., a lubricant, that penetrate into a porous material to make it repellent to a wide range of liquids in

conditions where SH usually fail, like humid and high-pressure environments. Due to the nature of the working interface, SLIPS usually exhibit lower Static contact Angle against water with respect to the standard superhydrophobic surface. Using SLIPS the interface turn from solid-liquid-air to liquid-liquid composed of the test liquid and the lubricant which cover the surface. The two liquids are immiscible, lead to the floating of the water on the oil, guaranteeing a complete absence of adhesion and an extraordinary mobility of the water drops on it. Figure 3 shows the schematization to fabricate SLIPS:

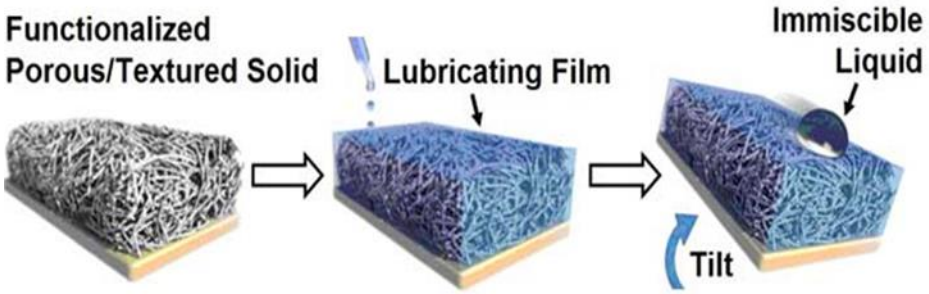

Figure 3. SLIPS schematization (T.-S. Wong et al., Nature 477 (2011), 443)

To have a proper efficiency, the lubricant should be included in a porous structure, in order to limit the oil depletion and increase the durability. In the last years many research groups began to study this kind of surfaces which present a huge potential in many fields. The main route to form porous surfaces is still the modification of the substrate forming a coating with the proper morphology to include lubricants between their pores. The voids should have a proper size to keep the oils between them exploiting the effect

of the capillarity pressure. Another way to graft the lubricant on the surface is to create a chemical affinity between the bottom coating and the lubricant itself.

In my Ph.D. project we made an inner hybrid coating on the surfaces presenting a porous morphology and a chemical composition suitable with the used lubricant oils. In this way, we tried to exploit both capillarity effect and chemical affinity.

Superhydrophobic surfaces, thanks to the complete repellence against liquids, can be utilized in the anti-icing application to prevent or reduce the nucleation and grow of ice in materials exposed in sub-zero environment. Recently, SHS has been studied as anti-icing materials to replace the traditional de-icing method and in particular the removal of accumulated ice layers basically based on the Joule effect, mechanical removal, electro-impulse methods and application of chemical de-icing fluids [42–45]. However, the traditional procedures as well as the utilization of large amounts of chemicals result to be in most cases expensive, time-consuming and dangerous for the environment. In the project I focalized my attention on the anti-icing solution for the aeronautic field, adopting different type of coating to minimize the ice nucleation and accretion on the aircraft features. Although, to better understand the role of SHS in anti-icing application an explanation of the concepts of ice formation and nucleation theory are described below.

1.2 Nucleation theory and ice formation on surfaces

In literature two different type of nucleation theories have been explained and precisely homogeneous and heterogeneous ice nucleation.

Ice nucleation can be divided in two processes [46]; the ice nucleation when the ice embryo is formed in the liquid phase and the formation of critical ice nuclei which lead to the phase transition of water from liquid to solid phase.

Under the thermodynamic driving force, ice nucleation will occur once a sufficient number of relatively long-lived hydrogen bonds spontaneously develop at the same location to form a compact nucleus. After, the nucleus alters the shape and size until reaching a stage that allows the rapid expansion, causing the freezing of the entire system [47,48].

In homogeneous nucleation the first step is the formation of different ice nuclei in a region of a water drop. The formed ice nuclei grow slowly changing their shape allowing the water transition from liquid to solid state. Furthermore, the formation of micro-ice nuclei leads to the decrease of free energy of the system, and the growth of them can cause an increase in interface free energy between nuclei and liquid water. These two effects compete with each other, resulting in the formation of a nuclear energy barrier. During this process, metastable states play an important role in the process of homogeneous freezing. Meta-stability is related to the transition process from high entropy water to low entropy solid ice. Based on the theory of Gibbs free energy [49] the nucleation starts in favorable situation, when the energy barriers are overcome[50].

The critical Gibbs free energy barrier for homogeneous nucleation ΔG* f is defined by [51]:

$$\Delta G^{*} = \frac{16\pi\sigma_{iw}^{3}}{3\Delta G_{f,v}^{2}}$$

The assumptions used to obtain the equation are that the ice embryo is spherical, and interfacial tension (σ_{iw}) is analogous to a macroscopic system. In the formula σ_{iw} represents the interfacial tension ice-water and $\Delta G_{f,v}$ indicates the difference of volumetric free energy between bulk ice and bulk liquid, which can be calculated from the Gibbs–Helmholtz.[52,53]

The nucleation rate in a homogeneous icing process is defined by the following equation:

$$J_{homo} = KNexp\left(-\frac{\Delta G}{K_b T}\right)$$

K is the kinetic factor indicating the attraction between free water molecules to be transferred into an ice germ. The variable N is the volume-based number density of water molecules in the liquid phase. K_b and T represent the Boltzmann constant and ambient temperature of the droplets,

respectively, and $\Delta G = \Delta G^* + \Delta G_{act}$ is the sum of the critical Gibbs free energy barrier and activation energy barrier.

The process schematization is shown in Figure 4:

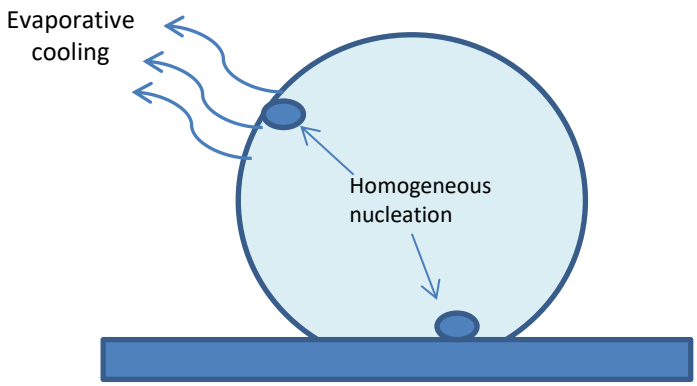

Figure 4. homogeneous nucleation process on a solid surface

In heterogeneous ice nucleation [54,55] the formation of nuclei also required the overcome of an energy barrier but the presence of some agents and impurities lead to the decreasing of energy barrier needed to ignite the process.

The heterogeneous process is shown in Figure 5:

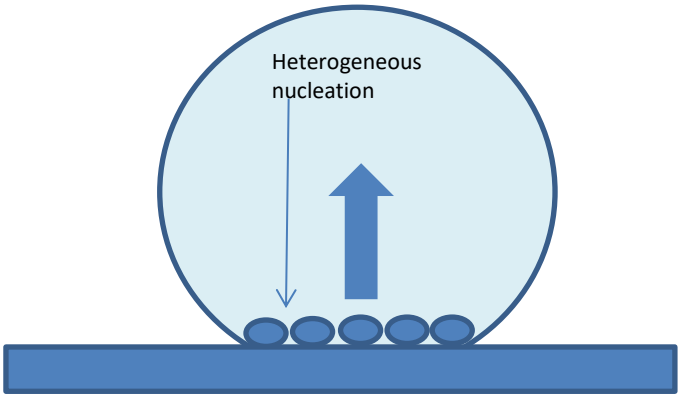

Figure 5. heterogeneous nucleation process on a solid surface

The energy barrier for the heterogeneous nucleation ΔG_{het} is defined as follow:

$$\Delta G_{het} = \Delta G^{*}_{hom} f(R, \theta)$$

$f(R, \theta)$ represent the dependence of the heterogeneous nucleation barrier on the static water contact angle θ and the surface roughness radius of the curvature R and f values is place between 0 and 1. Having f values between 0 and 1 is pretty clear that the energy barrier of the heterogeneous nucleation can't be higher than the homogeneous one.

1.3 Ice nucleation on superhydrophobic surface (LF) and SLIPS

Superhydrophobic surfaces use their micro-nano features to achieve the anti-wetting state. The presence of the proper morphology can also be exploited for anti-icing application. In particular the presence of air pockets trapped between the micro-nano structure minimize the contact area between the solid fraction and the liquid one during the freezing process leading to smaller supercooling gradient, and a lower tendency towards ice nucleation [56,57].

The first study concerning the ice nucleation theory on SH surfaces was performed by Alizadeh and colleagues which recorded the transient temperature of a water drops on Lotus-leaf like material during the freezing process [58]. The comparison between the SHS with flat hydrophobic and hydrophilic surfaces clearly demonstrated the effect of the trapped air on delaying the ice nucleation due to the formation of local supercooling gradients along the surface.

Micro-nanostructured superhydrophobic surface (named LF in this thesis) , sindicate also that ice nucleation rate and the capacity for its inhibition is determined by the actual solid / liquid contact area and the size of the nanostructures [59–61].

The main hindrance of the SHS is that they are very susceptible to frosting coupled with the possible increase of ice adhesion due to the presence of the asperities of the hierarchical structure [62–64].

SLIPS have been widely studied for their anti-icing properties [65–69]. Because of the infused low surface energy lubricant that poses a higher free energy barrier, SLIPS is considered a promising candidate to inhibit ice nucleation.

Comparing SLIPS with typical LF surfaces, the first ones exhibited an higher amount of supercooling which leads to a depression of the freezing temperature [70]. It was reported [67]a loss of lubricant during icing/de-icing cycles due to the displacement of the oil transported away by the freezing water but the reservoirs of lubricant trapped in the porous structures can replace the oil-naked zones, driven on the top of the surface by the effect of the capillary forces [71–73].

Due to these aspects the utilization of SLIPS concerning the anti-icing application overcame the typical SHS in the last decade.

1.4 Ice accretion on a solid surface

During an icing process a lot of variables have an effect in the formation and accretion of ice. There are three principal regime of ice which can occur during a freezing phenomenon:

- Glaze ice
- Rime ice
- Mixed ice

The equation which governs the ice regime type formation is found by Makkonen [74] and is the following:

$$\frac{dM}{dt} = \alpha_1 \alpha_2 \alpha_3 \omega v A$$

dM/dt indicates the rate of icing. A is the cross-sectional area which depends on the direction of the particle velocity vectors v. ω is the particles concentration on the cold flux and the product of v and ω gives the flux density (F). α_1, α_2 and α_3 are correction factors which may have values from 0 to 1.

α_1 represents the efficiency of collision of the particles and depends on the dimension on the drops in the cold flux. The small particles follow the air streamlines with no collision with the surfaces. Instead, large particles collide on the solid starting the icing processes.

α_2 represents the efficiency of collection of the impacting drops also known as sticking efficiency. This correction factor is reduced from unity when the drops bounce off from the surfaces.

α_3 represents the efficiency of ice accretion and reach the unity when the heat flux from the accretion is not enough high to cause freezing. In some case the mass flux of the particles is lost from the surface run-off.

In the case of α_3=1 there is not liquid layer in contact with the surfaces and no drops run-off. The icing process takes place in dry conditions leading to the formation of rime ice. Rime ice is usually formed at temperature below -4°C and presents a low Liquid Water Content (LWC). Rime ice appears as a transparent crystalline layer with pockets air trapped.

When α_3<1 there is a liquid layer upon the surfaces and the icing process begin from this layer. This case is known as wet growth leading to the appearance of the glaze ice. This ice regime is typical in a temperature range from 0 to -4°C. Glaze ice presents a high LWC and an opaque resemblance.

When the environments condition is close to the middle of the glaze and rime ice regimes appearance mixed ice is formed. Mixed ice presents intermediate properties between glaze and rime ice and is typically formed in a temperature range between 0 and -20°C [75].

Concerning the aeronautic field, the icing regime obviously depends on the temperature which have a key role in the formation of different type of cloud. The most common clouds are the stratiform and the cumuliform clouds. The first ones present mostly solid phase particles giving rise to the formation of rime ice. When an aircraft pass through a cumuliform cloud, which presents mostly liquid phase particles glaze ice is formed[76].

The risk linked to the environment which an airplane passes through during the first and last period of fly depending on temperature and altitude is schematize in Figure 6:

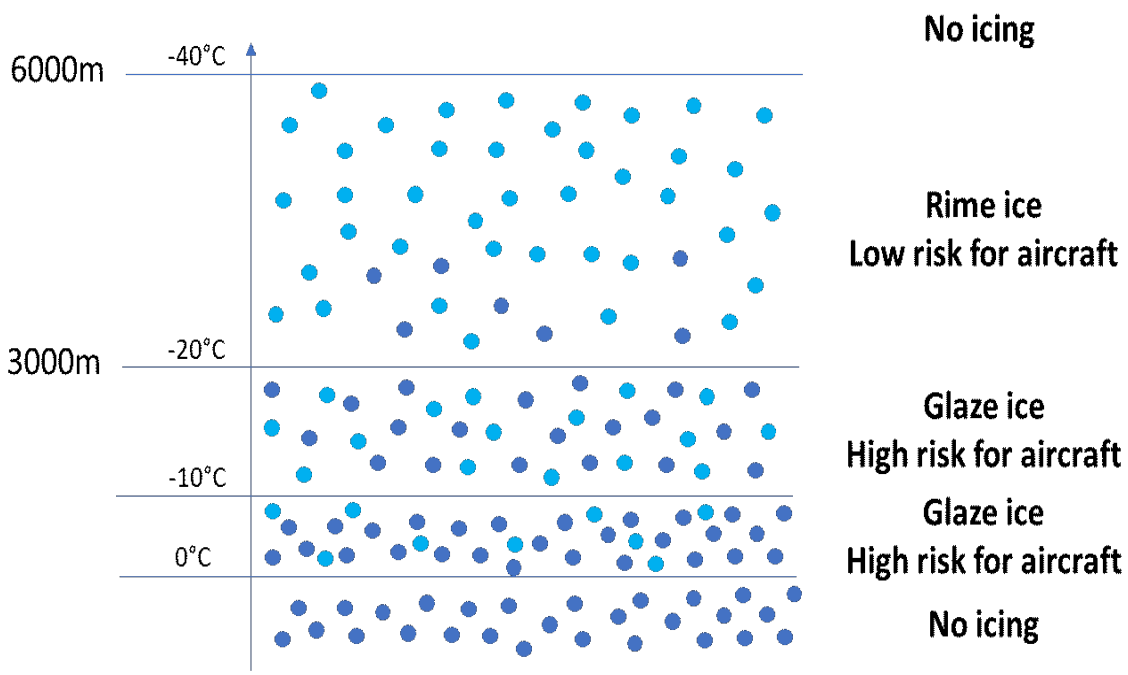

Figure 6. Schematization of the different environments in the atmosphere depending on temperature and altitude

The different ice regimes also lead to the formation of different shapes of ice particles. In particular glaze ice is an agglomerate of rounded freeze drops while glaze ice crystals exhibit irregular shape when grow on a surface.

Due to the irregular shape and the high LWC glaze ice is more difficult to remove with respect to rime ice [77]. In particular the drops are able to coalescence in liquid form leading to the formation of a continuous layer

with strong bond to the surface. As a consequence, different levels of the risk depending on the ice regime meet at the different altitudes.

The concentration and distribution of the supercooled water drops and ice crystal vary with the temperature and altitude. As the temperature decreases, so does the vapor density while the probability of the droplets freezing increase, leading to a low possibility of icing (freeze droplets do not stick to the surfaces). Ice accumulation can reduce the lift up to 30% and increase the drag by 40% [78].

In the last years anti-wetting surfaces gained a lot of interest as passive anti-icing method to avoid the hindrances due to the typical de-icing and anti-icing method [79–84]

Three main methods were used in order to prevent or decrease icing phenomenon on surfaces, and respectively:

- **Ice nucleation delay**, based on the formation of a quasi-static equilibrium on the liquid water droplets placed a T lower than 0°C which retard the nucleation of the ice.
- **Ice adhesion decrease**, based on the utilization of products able to limit the adhesion force between the formed ice and the surfaces.
- **Decrease of the contact time between super-cooled drops and surfaces**, based on the drops rebound due to the high dynamic properties of the surfaces (Low Contact Angle Hysteresis).

The described routes are schematized in Figure 7:

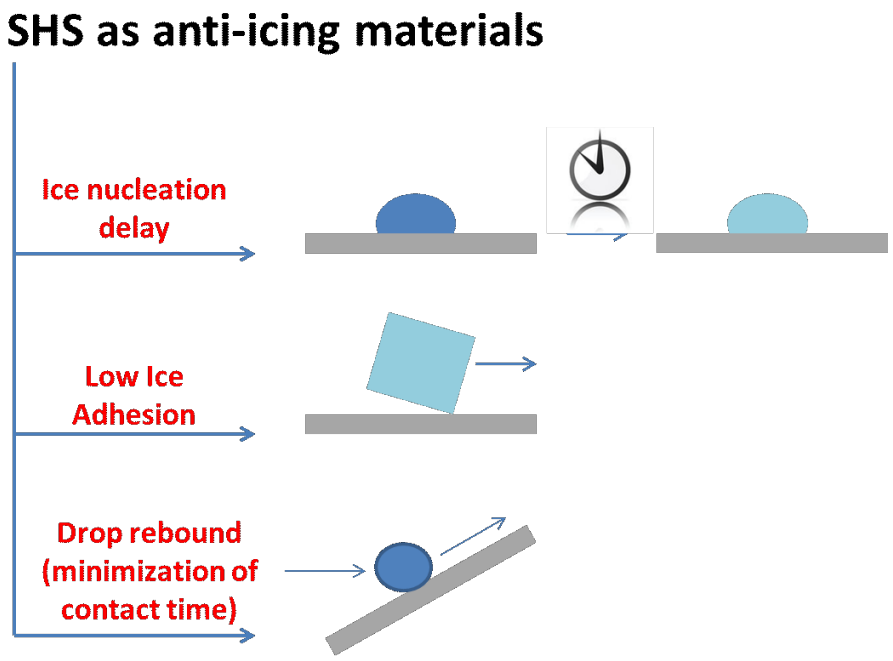

Figure 7. Schematization of the routes usually adopted to limit the ice nucleation and accretion on surfaces

1.5 Ice nucleation delay theory

The delay of ice nucleation is one of the main method to obtain anti-icing and is closely related to the ability of thermal transmission at the apparent contact interface of solid/liquid [85,86]. Freezing delay time (DT) is defined as the time from the impact of the drop on the surface to the onset of the freezing. It is usually evaluated by visual analysis carried out by CCD camera, which follows the behavior of the drop at temperature below 0°C. Many factors can interface with the delay time such us heat transfer between the liquid and the surface, surface energy, surface roughness, nucleus curvature, water drop size, surface area and the interfacial energy barrier. [46,49,50,87–91]. To increase the delay time the strategies usually adopted are:

- Utilization of low surface energy chemicals able to modify the wettability of the surface
- Utilization of chemical or physical methods to modify the surface morphology and roughness

Numerous studies [92,93] have demonstrated that the surface wettability can play an important role in icing delay time and in some cases, superhydrophobicity caused huge delays in ice nucleation if compared with the bare substate.

Andrei et al [88] studied the effect of wettability on delay time at temperature from 0 to -30°C. They found that the water drops can remain in a metastable supercooled liquid equilibrium up to 30 minutes, even on hydrophilic

surfaces. Despite this the superhydrophobic materials exhibited a larger DT if compared with the hydrophilic ones.

Guo et al [94] studied the effect of different morphologies on DT. They found a positive effect of the hierarchical micro-nanostructure on delay the ice nucleation probably due to the presence of the air pockets between the nano-features which act as barrier between the liquid and the surface, reducing the contact area.

Yue et al [93]demonstrated that the DT on hierarchically structured surfaces was 4 time bigger than bare substrate.

Over the past years SLIPS overcame the typical SH surfaces concerning the delay of nucleation time for different reasons such is better homogeneity, higher resistance and larger insulator effect with respect to the air bubbles trapped on the nano-features of the typical SH materials hierarchical structure. [95–98] Moreover the size of the condensed drops are too small to be supported by the air bubble trapped in the hierarchical structure.

For example, Wei at al [99] compared superhydrophobic coatings and SLIPS in terms of DT. Surfaces infused in lubricant oils shown DT of about 1500s while the delay on SH was maximum 300s.

1.6 Ice adhesion decrease theory

A material is defined anti-icing when the adhesion force between ice and the surface is W_{adh}<100KPa. [100]

One of the most important roles in decreasing ice adhesion is played by surface wettability and more precisely by the dynamic abilities of the materials. If the drop is inclined or its volume changes in time, two different angles will be observed: the advancing contact angle ACA or θA, referred to the movement of contact line towards a non-wetted area; the receding contact angle RCA or θR, referred to the movement of contact line towards a wetted part of the surface[101]. It will always be true that ACA ≥ RCA. The difference ACA - RCA is called contact angle hysteresis CAH or Δθ and is related to drop mobility on the surface. It was found that if the receding angle θR of the droplet on the solid surface exceeds 118.2◦, it leads to a distinct reduction in ice layer adhesion. Therefore, the superhydrophobic surface with appropriate rough microstructure can effectively reduce the ice adhesion [5,102]

Ice adhesion force is usually calculated via self-made devices able to find the shear strength to separate ice from the substrates. [103,104]

The correlation between the shear force and ice adhesion is given by the equation $W_{adh} = F/A$, where A is the area of the surfaces which underwent to the analysis. The adhesion between a water droplet and surface on a stationary substrate was calculated by McCarthy and Meuler [105,106]:

$$W_{adh} = \sigma_{LV}(1 + cos\theta)$$

σLV represents the liquid surface tension in air while θ is the liquid receding water contact angle. The equation highlights the strong dependence of the ice adhesion force with the receding contact angle, which means that the adjustment of the surface morphology and chemistry should lead to a decrease of the receding angle and of the W_{adh} as a consequence.

Despite that, not only externally forces and adhesion between the ice and substrate in the process of deicing have to be considered, but also van der Waals interaction and hydrogen bonds which plays an important role in the total ice adhesion. In fact, the latter is much greater than the macroscopic adhesion, and therefore, the mechanical interlock between ice dominates the ice adhesion.

Mechanical interlocking of within an anti-wetting surfaces with a certain roughness enhanced adhesion but the formation of micro-crack can be use as interface stress concentration point, which would decrease the adhesion. [107]

The anti-wetting behavior can increase the resistance of supercooled water droplets adhering and the heterogeneous nucleation on the solid surface. Ice formation and accumulation under the Cassie–Baxter state after the solid surface is modified with low surface energy materials will ensure minimum contact area between the ice and substrate surface for efficient and quick ice removal. To confirm the effect of the anti-wetting state, ice adhesion on a

Wenzel wetting state material is much larger than the Cassie-Baxter wetting state one.

Despite that, it was found that the SLIPS achieved much greater results in terms of ice adhesion reduction if compared with the typical superhydrophobic surfaces. [69,108–111]. The deposition of a lubricant layer on the surfaces lead to the floating of the formed ice on it with a really low adhesion force between them.

The better homogeneity achieved depositing lubricant oils has an effect on the presence of adhesion spots along the surface, covering the asperities of the substrate which can work as favorable points for the ice adhesion, increasing the force need for the ice detachment.

Moreover, SLIPS have a higher resistance in icing environment with respect to the conventional LF surfaces as discussed before in the thesis.

1.7 Decrease of the contact time between super-cooled drops and surfaces

This method is focused on the decrease of the contact time between the surface and the supercooled water drops impacting on it. Differently with the other characterization methods, which are static tests, this process and observation are performed in dynamic conditions and precisely with the supercooled drops whit a certain speed, LWC and hit a surface at a temperature below 0°C. The impact of the drops with the consequent rebound or sticking on the substrate is governed by different variables such

us temperature of the liquid, temperature of the surface, drops velocity, liquid water content and diameter. In particular LWC plays a key role on it, because due to the anti-wetting nature of the coatings, it will be more easily repel supercooled drops with high liquid water content on it with respect to particles containing a larger amount of solid water on it. The surface parameter which governs the drops rebound capacity is the Contact angle Hysteresis[112]. Materials with low CAH allows the drops to roll of from the surface, limiting the contact time and then the possibility of ice nucleation and accretion on them.

The effect of CAH on drop rebound is shown in Figure 8:

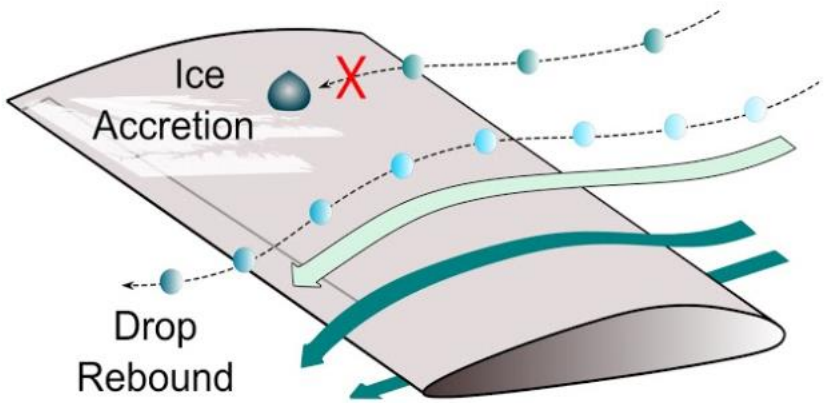

Figure 8. Effect of CAH on drop rebound. As lower CAH as higher is the ability to repel impacting water

Several recent papers concern the dependence of ice nucleation and accretion on the contact time between supercooled water droplets and low-wettable surfaces. Mishchenko et al. [113] specifically highlighted the relationship between the dynamic repellency to liquids and the attitude to ice nucleation and accretion of different coated surfaces. On surfaces with CAH as low as 15°, a full retraction of the supercooled drops is expected before ice nucleation occurs. Khedir et al. [114] found a complete drop rebound at temperatures as low as -10°C on SH Teflon-coated surfaces, suggesting their potential anti-icing properties in aeronautical applications. Poulikakos's group [46] studied the impact of supercooled droplets on SH surfaces, highlighting the role of water viscosity on the penetration in the structural features of coatings occurring at subzero temperature.

The test is carried out usually via icing wind tunnel test, controlling speed, LWC, drop diameter and temperature. The liquid dynamic behavior is monitored via CCD camera focalized on the impact area of the sample.

In this Ph.D. project I focused on the hybrid nanostructured coatings obtained via sol-gel synthesis of Alumina and Fluorinated Silica Nanoparticles (NPs) and deposited via dip-coating technique. Al_2O_3 NPs were synthetized following a sol-gel process published by Minami et al [115–117] while fluorinated SiO_2 NPs were prepared via sol-gel technique optimized in ISTEC-CNR.

The deposition of ceramic oxide nanoparticles, followed by some thermal treatments, lead to the formation of the typical hierarchical micro-nano

structure on the surfaces with different morphologies depending on the suspension nature, fundamental to achieve the Cassie-Baxter wetting regime.

The final step to form lotus-leaf like materials (LF in the next chapters) is the chemical modification, carried out by deposition of commercial fluoroalkylsilane solution (FAS). Such change in surface chemistry caused a drop in Surface Energy (SE), therefore a switch from superhydrophilicity to superhydrophobicity. After each step of the process, the surface was characterized in terms of wetting properties to assess the evolution of parameters like Water Contact Angles (WCA) and Contact Angle Hysteresis (CAH).

The main hindrance of SHS based on mimic of Lotus leaf is the durability. [118,119]

In order to overcome this problem LF surfaces underwent to a further infusion in lubricant oils with different viscosity and chemical composition giving SLIP surfaces, which present higher resistance towards severe icing conditions.

Lubricant oils are able to enter between the LF structure features replacing the air pockets of the Cassie-Baxter wetting state. In this way the working interface pass from solid-liquid-air to liquid-liquid because the layer exposed to fluids become the lubricant instead of the nano features of the LF based surfaces. The wetting behavior of SLIPS result quite different with respect to the LF and precisely exhibit a lower water contact angle but outstanding

dynamic water repellence with the drops which easily roll off from the surfaces with no sticking evidences. The key parameters for the anchorage of lubricant within the porosity of the surface structure are the capillarity force and the chemical linking. To trap lubricant the holes, present in the nano structure, has to be of the right size; wide spaces don't allow the right entrapping of the oils due to the poor capillarity force.

2.Materials and methods

2.1 Sol-gel synthesis of ceramic oxide nanoparticles sol

A sol is a colloidal suspension of solid particles in a liquid [83]. Such particles are so small (diameter < 1 μm) that gravitational forces acting on them can be neglected.

Sols of ceramic oxides are obtained from different precursors, either inorganic [120] or organic. Among the latter, metal alkoxides $M(OR)_n$ [121], where M is a metal or a metalloid (e.g. Si) and OR is an alkoxy ligand, are the most commonly used. These compounds undergo hydrolysis spontaneously with ambient humidity. However, water is usually added to the reaction mixture, possibly with either acidic [122–124] or basic [19,125] catalyst.

$$M(OR)_n + H_2O \rightarrow M(OR)_{n-1}(OH) + ROH$$

Not necessarily all OR groups are hydrolyzed. Water content in the mixture, catalysts and chelating agents like acetoacetates [117] are able to influence the degree and the rate of hydrolysis. Specifically, complete hydrolysis is undesired as it leads to sol instability and precipitation of metal hydroxides in a short time. This is true especially for alumina precursors, while silicon alkoxides are much more unreactive and rather need catalysts to hydrolyze [126,127]. Furthermore, the dispersing medium has a strong influence on the

nature of the coating sol. Alcohols are the most widespread media, but water allows for greener routes.

After hydrolysis, condensation reactions lead to the formation of M-O-M bonds and either a water or alcohol molecule. Indeed, condensation is a polymerization reaction, whose product is a macromolecule.

$$M(OR)_{n-1}(OH)+M(OR)_n \rightarrow (RO)_{n-1}M-O-M(OR)_{n-1}+ROH$$

$$2M(OR)_{n-1}(OH) \rightarrow (RO)_{n-1}M-O-M(OR)_{n-1}+H_2O$$

Condensation reactions can go on until hydrolysable OR groups are available. When the macromolecule reaches macroscopic dimension, a transition from sol to gel occurs. In a gel, the solid phase is continuous and encloses a continuous liquid phase. Further, deposition of a sol on a surface followed by rapid evaporation of the solvent leads to a gel film. Gelation times depend on parameters such as pH [128]. Even after gelation, hydrolysis and condensation reactions still happen, involving the sol phase entrapped within the continuous gel phase. This phenomenon is called ageing.

Sol-gel syntheses find massive application in ceramic materials science, due to the facile fabrication and low-cost applications, giving materials with unique properties [129]. The most common oxides obtained via sol-gel are silica SiO_2 [130,131], alumina Al_2O_3 [123] and titanium oxide TiO_2 [132,133] but is possible to obtain ceramic sols of many others oxides [134,135].

There are two ways of preparing sol-gel coatings. The first one is to form the coating in situ, on the substrate surface [136]. Typically, the surface is coated

with precursors, which react and form a gel film. However, this procedure cause a big loss of chemicals increasing the waste production and the process cost. Therefore, it is better to synthesize a stable suspension of ceramic oxide nanoparticles which can be used for deposition in a much longer time spun, until the aggregation of the nanoparticles.

During my work I focalized my attention in the synthesis of Al_2O_3 and SiO_2 nanoparticles sol to create two different morphologies which might impact the anti-icing ability of the surfaces.

2.2 Synthesis of Alumina Nanoparticles sol

Al_2O_3 NPs were synthetized in alcoholic media and precisely in Isopropyl alcohol (i-PrOH) using Aluminum-sec-butoxide $(Al\text{-}sec\text{-}but)_3$ as precursor. It is widely used in the synthesis of Alumina compounds because provides highly pure products. The only problem of this precursor is the high sensibility to the humidity and promptly forms white $Al(OH)_3$ precipitates when exposed to air. To overcome this the synthesis of Al_2O_3 NPs was carried out in a glove box where relative humidity was kept at 5%.

Ethyl acetoacetate (EAcAc) was chosen as ligand because promoted alkoxide stability in water. Specifically, EAcAc forms an extremely stable, six-membered complex with an Al atom through donor-acceptor interactions. The choice of EAcAc:Al ratio has an influence on the average size of particle size [115]. Specifically, particles become smaller with an increase in this molar ratio since the chelating agent prevents the growth of particles and delays their aggregation.

The synthesis was performed as follow. Aluminum-tri-sec-butoxide (97%, Sigma-Aldrich) was stirred in isopropyl alcohol (99%, Sigma-Aldrich) for 1 h at room temperature. Then, ethyl acetoacetate (99%, Sigma-Aldrich) as the chelating agent was added and the solution was stirred for 3 h. Finally, water was gradually added to the solution to promote the hydrolysis of the alkoxide, keeping the sol under stirring for 24h at room temperature. The molar ratios of EAcAc, water and i-PrOH with respect to Aluminum-sec-butoxide were 1, 4 and 20 respectively.

After 24 hours, the stirring was interrupted and the sol collected for characterization. Average particle size was determined by Dynamic Light Scattering (DLS, Zetasizer Nano S, Malvern Instruments). This technique is based on the scattering of a laser beam by a suspension of nanoparticles. From the analysis of the scattered signal, the distribution of hydrodynamic diameters for suspended particles is calculated [137,138]. The measured distribution is reported in Figure 9:

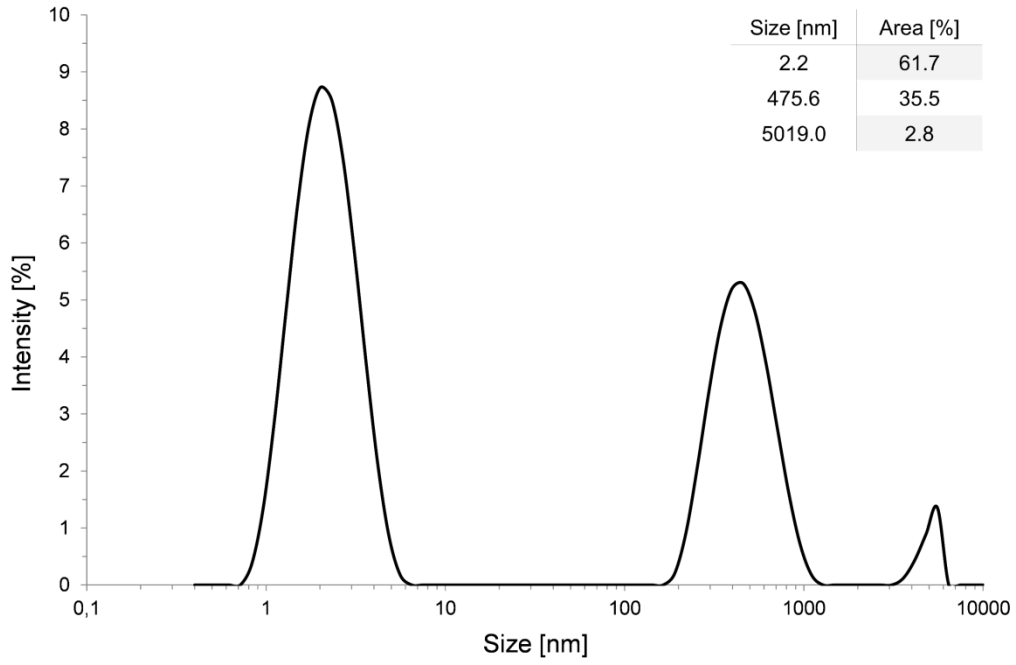

Figure 9. DLS spectrum showing the particle size distribution in the alumina

The DLS spectra exhibit a multimodal nanoparticles distribution with the main peak centered at 2.2 nm with smaller amounts of aggregated particles.

2.3 Synthesis of Silica Nanoparticles sol

The suspension of fluorine-bearing silica nanoparticles was prepared as follows: ammonium hydroxide NH4OH (30%, Sigma-Aldrich) was added to ethanol (99%, Sigma-Aldrich) and stirred to complete dissolution. Then, tetraethylorthosilicate (TEOS 98%, Sigma-Aldrich) was introduced in the solution, setting the temperature at 60°C. Once the temperature was reached,

perfluoroctyltriethoxysilane (PFOTS 98%, Sigma Aldrich) was added in the solution enhancing the hydrophobic behavior of the silica nanoparticles. The particle size distribution of the suspension was evaluated by DLS. The spectrum of the nanoparticle suspension exhibits a monodisperse size distribution (PdI = 0.1) with a clear peak positioned at 481nm (Figure 10).

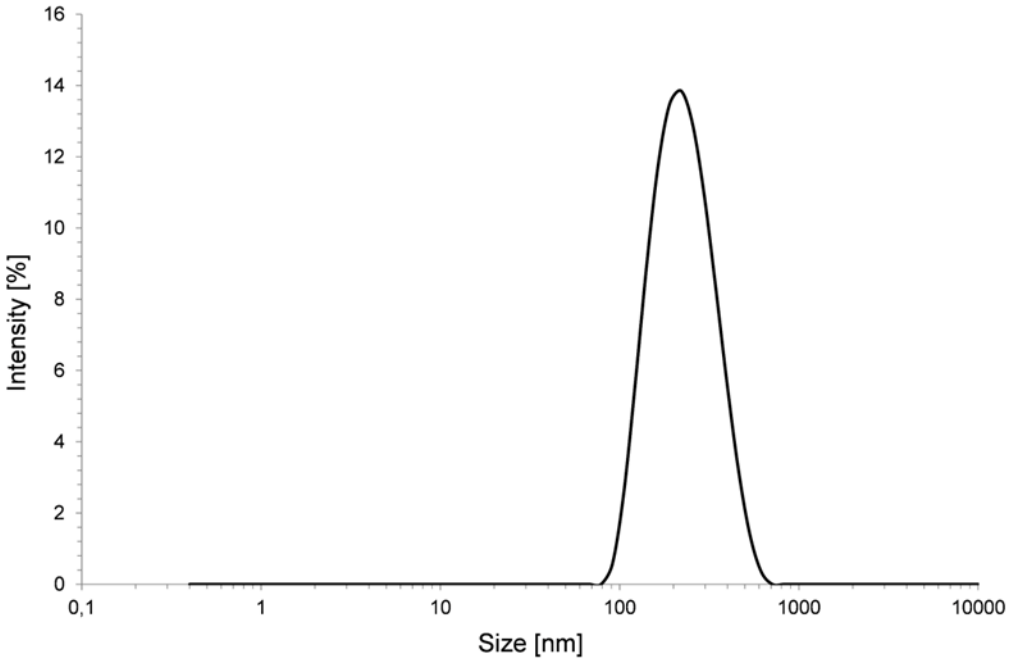

Figure 10. DLS spectrum showing the particle size distribution in the silica

2.4 Coating deposition and processing

During my Ph.D. project I used dip coating as deposition method mainly because is:

- simple deposition method
- low cost
- adaptable to different substrate shapes
- easily transferable to industry

Dip coating includes the soaking of the substrate in the ceramic oxide nanoparticles suspensions for a certain time.

Notwithstanding this apparent triviality, it is a complex process in which many parameters must be controlled to achieve reproducible results. Withdrawal speed is the most important parameter, as it strongly influences the gel film thickness. Landau and Levich [139] studied the relationship between film thickness h and withdrawal speed u:

$$h = \frac{0{,}94\,\eta^{2/3}}{\gamma^{1/6}(\rho g)^{1/2}}\ \mathrm{u}^{2/3}$$

η, γ and ρ are sol viscosity, surface tension and density, respectively. This relationship was obtained for withdrawal speeds above 1 mm/s. In such conditions, viscous drag by gravity is the most important factor (viscous regime). For lower speeds (draining regime), evaporation becomes faster than the motion of the drying line, inducing the feeding of coating sol from the reservoir by capillary. Such phenomenon causes deviations from predictions. Indeed, for speeds in the order of 0.1 mm/s the tendency is

reversed, as film thickness increases with decreasing speed. Grosso et al. [140,141] published papers to describe this phenomenon and eventually established a more accurate relationship between u and h:

$$h = K\left(\frac{E}{Lu} + Du^{2/3}\right)$$

this equation, k is a composition constant (proportional to concentration), E is the evaporation rate, L is the substrate length and D contains the physical-chemical characteristics of the coating solution. Both the capillary regime (E/u term) and the viscous regime ($Du^{2/3}$ term) contribute to final thickness.

The control of the coating thickness is very important when the optical properties of the substrate must be unaltered. Using coatings with thickness smaller than the wavelength of visible light, the transparency can be equal or even increased, leading to the appearance of the anti-reflective property [136,142].

To coat the substrates during my Ph.D. I mainly use two different type of dip coaters, maintaining the same methodology.

The main concept of dip coating is shown in Figure 11:

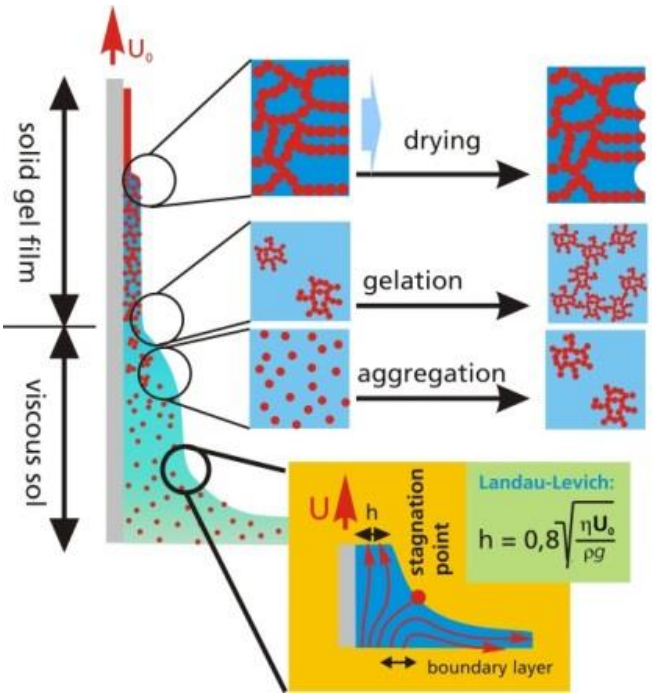

Figure 11. schematization of the dip coating process (Grosso, J. Mater. Chem., 2011, 21, 17033)

For small substrate the dip coating was performed using a homemade device composted of a steel arm moving vertically along a screw. The speed of dip coating was controlled modifying the voltage of a potentiometer. The device is shown in Figure 12:

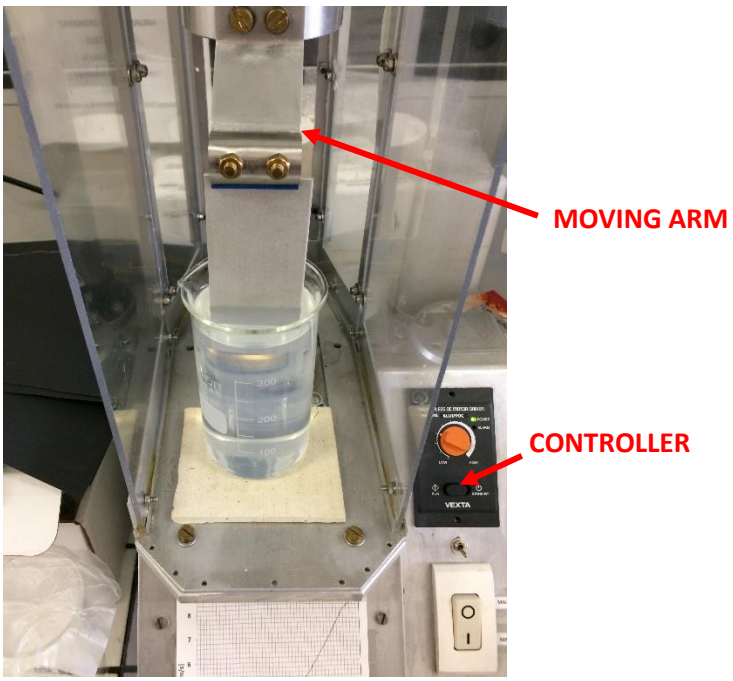

Figure 12. Home-made dip coater used for small sizes samples

For substrate larger than 150mm an automated dip coater was purchase from Aurel Automation (Modigliana (FC), Italy). It is a tailored dip coater, designed and developed according to the requests of the research group. This dip coater features a large chamber (internal overall size 1700 x 1000 x 700 mm) and two linked steel arms moved along a rail by an electric engine. All operations are computer-driven and the user can set all the parameters, such us dipping and withdrawal speed, immersion time, starting, intermediate and immersion position and drying time. This allows for maximum repeatability of the dipping process. The limitations in sample size are mainly linked to the chosen vessel, which also determines the necessary volume of coating liquid.

The device is shown in Figure 13:

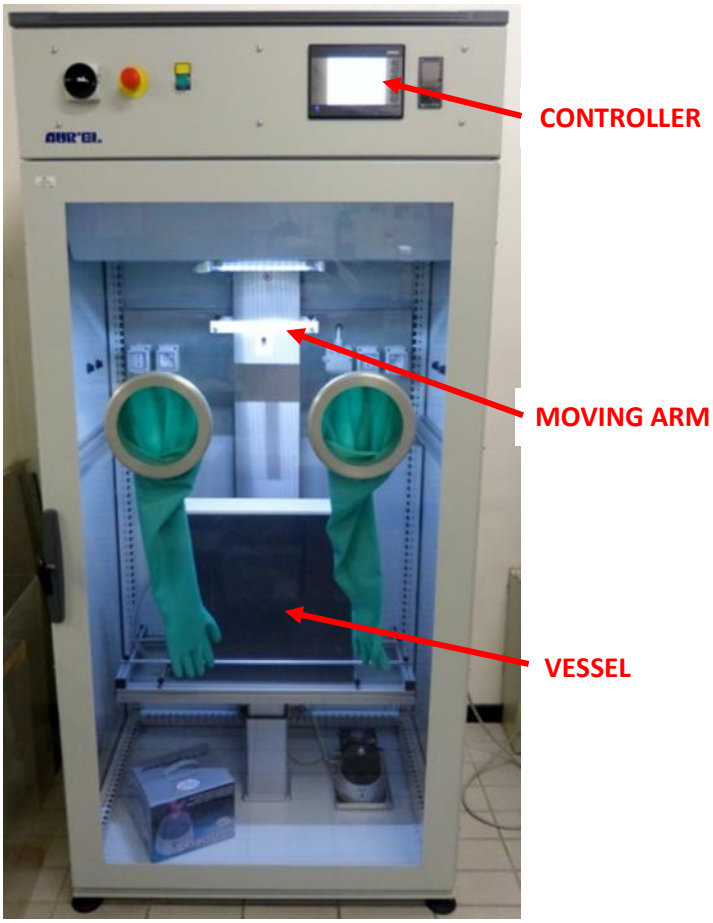

Figure 13. Automated dip coater purchased from Aurel Automation (Modigliana (FC) Italy)

The immersion/withdrawal speed was set at 2mm/s for each deposition process because is an optimized value obtained after different past experiments in ISTEC. The soaking time depend indeed on the composition of the nanoparticles sol. As for the immersion/withdrawal speed the soaking time were optimize through different tests, arriving to soaking times of 5s in

Alumina nanoparticles sol and 1min in the Silica one. These times provide us samples with layers reasonably thin and uniform in the end of the process. The deposition parameters are shown in Table 1:

Table 1: Parameters adopted for dip coating deposition of Alumina and ilica nanoparticles suspensions

Ceramic oxide suspension	Immersion/withdrawal speed (mm/s)	Soaking time (s)
Al_2O_3	2	5
SiO_2	2	60

After dip coating the samples followed different process steps depending on the nature of the deposited suspension.

2.4.1 Alumina based coated substrate process

After dip coating in the Alumina suspension the samples underwent to a first thermal treatment (TT) at 400°C for 1 h. This annealing step allowed for a complete drying of the film, removal of organic components, completion of condensation and densification, with positive effects on mechanical properties [143].

The morphology of the coating after the first TT is shown in Figure 14:

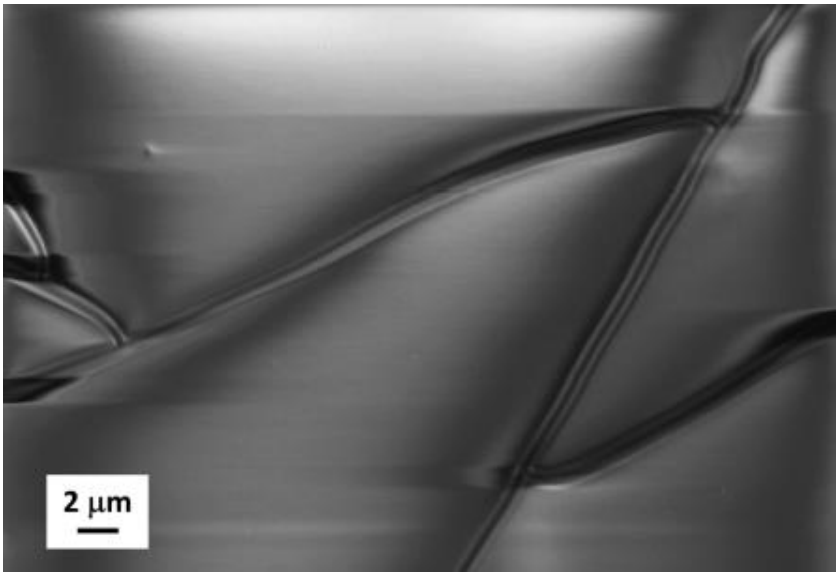

Figure 14. Micrograph of Alumina sols deposited on Aluminum substate and annealed at 400°C for 1h

The Alumina deposition and the TT led to the formation of a smooth layer which already presented some cracks along the surface.

Concerning the temperature after an analysis of the literature about alumina films, we inferred that the optimum temperature for the heat treatment of sol-gel alumina treatment was 400°C, in order to guarantee the complete removal of organic ligands [115] and the formation of an amorphous alumina film [144]. The formation of cracks during this process is the main hindrance. Kozuka research group [145–147] studied the cracking phenomenon in gel

films. From their studies, it is evident that the intrinsic stress occurring during heating is maximum when condensation takes place during the treatment. However, in the deposition of a stable nanoparticle suspension, condensation is limited. Thus, cracking will be reduced and will be due mainly to differences in possible thermal expansion coefficients with the substrate (e.g. thermal stress) and capillary pressure caused by solvent vaporization. The same authors emphasized the positive role of chelating agents in diminishing crack formation during heating.

During my project we noticed a smaller number of cracks if the samples were put in the oven already at 400°C if compared with the substrate introduced in temperature ramp. For this reason, all my samples were processed with no temperature ramp.

After the first TT alumina based coated substrate were cooled in air environment and then treated in boiling water. It is known from the literature [116] that alumina Al_2O_3 reacts with hot water to form boehmite AlOOH with a peculiar flower-like structure, resembling a desert rose. Such morphology is able to entrap air and develop a high anti-wetting capillary pressure [148]. In this project, we formed boehmite on alumina-coated surfaces by immersion in boiling DI water. We chose to treat the coated surfaces for 30 minutes following the studies performed by Feng et al. [30] which suggest to be the optimum time for achieving superhydrophobicity on alumina-coated surfaces. A further thermal treatment was performed to complete drying and sinter the coating without losing the flower-like morphology [149]. Treatment temperature was the same as in the previous

annealing step, but treatment time was shortened to 10 minutes as no organic species had to be eliminated.

The boiling process allows us to obtain the right morphology for the superhydrophobicity composed of a hierarchical micro-nanostructure of boehmite.

The final step of the process was the chemical modification of the layer using a fluoroalkylsilane solution named Dynasylan SIVO Clear EC (Evonik, Germany). This modification is needed to obtain superhydrophobic behavior of the substrates, due by the introduction of stable C-F bond. The solution was grafted to the samples by dip coating with the same immersion/withdrawal speed than inorganic sol deposition (2mm/s) but a soaking time increased to 2min, in order to facilitate the reaction between the inorganic layer and the fluorine-based molecules present in the SIVO. The increase of the soaking time has no effect on the final performance.

2.4.2 Silica based coated substrate process

After the deposition on the suspension of fluorine-bearing silica nanoparticles samples underwent to a single thermal treatment in oven at 150°C for 30 min which allows the evaporation of the organic compounds and the stabilization of the coating, improving the mechanical properties.

This is the only step of the process because the coating already achieves the right morphology and the chemical modification was performed during the synthesis, grafting the fluorine molecules on the nanoparticles themselves.

As described in the next chapters of the thesis, the samples presented agglomerated nanoparticles disposed quite homogenously on the whole surface coupled with the presence of voids with different dimensions, able to trap air and giving rise to superhydrophobic behavior. The limited steps necessary for the functionalization with Silica suspension presents huge advantages whit respect to the Alumina one and in particular thinking to the industrial transfer of the technology. The cost of the process is reduced in terms of both energy consummation and reagents needed for the synthesis and functionalization steps. Moreover, the deposition of the Silica nanosuspension resulted less time consuming than the Alumina one, allowing the production of the same number of samples in about half time.

2.5 SLIPS Fabrication process

To prepare SLIP surfaces the Alumina based (LF) and Silica based coated samples underwent to a further infusion in lubricant oils with different viscosity, surface tension and chemical composition.

The list of the used lubricants is shown in the Tab.2:

Table 2. Surface tensions (γ) and viscosity (μ) of the four lubricants used for the fabrication of SLIPS.

Lubricant Oil	γ (mN/m) ± σ (mN/m)	μ (cSt)
Krytox™100	16.60 ± 0.04	12.4[1]
Krytox™103	17.41 ± 0.01	82[1]
Krytox™105	18.35 ± 0.08	522[1]
Silicone Oil 10cst	20.01 ± 0.30	9-11[2]

[1]Chemours Technical Specifications of Krytox™ GPL series oils;

[2]Sigma-Aldrich Product Specification Sheet.

Krytox™ GPL (Dupont) oils are a series of lubricants which contain fluorinated molecules, able to both decrease Surface Energy and replace the air pockets trapped in the nanofeatures of the Cassie-Baxter wetting state typic for LF surfaces. Krytox™ GPL 100, 103 and 105 present difference in their viscosity and Surface Tension.

Krytox™ GPL oils series were applied on both Silica-based and Alumina-based coating while Silicone Oil was infused on only Silica-based materials, trying to exploit the chemical affinity between Si molecules present in both surface and lubricant. After the infusion the samples were left in vertical position for one night to eliminate the oil excess and then tested in terms of anti-wetting and anti-icing properties.

Samples details are summarized in Table 3.

Table 3. Summary of the tested coating compositions.

Sample	Inorganic layer	Organic layer	Lubricant
LF	Alumina	FAS	/
Al_2O_3Kr100	Alumina	FAS	Krytox™ GPL 100
Al_2O_3Kr103	Alumina	FAS	Krytox™ GPL 103
Al_2O_3Kr105	Alumina	FAS	Krytox™ GPL 105
SiO_2F SO10	Fluorinated Silica	/	Silicone oil 10cSt
SiO_2FKr100	Fluorinated Silica	/	Krytox™ GPL 100
SiO_2FKr103	Fluorinated Silica	/	Krytox™ GPL 103
SiO_2FKr105	Fluorinated Silica	/	Krytox™ GPL 105

The schematic drawing of the obtained SLIPS is shown in Figure 15:

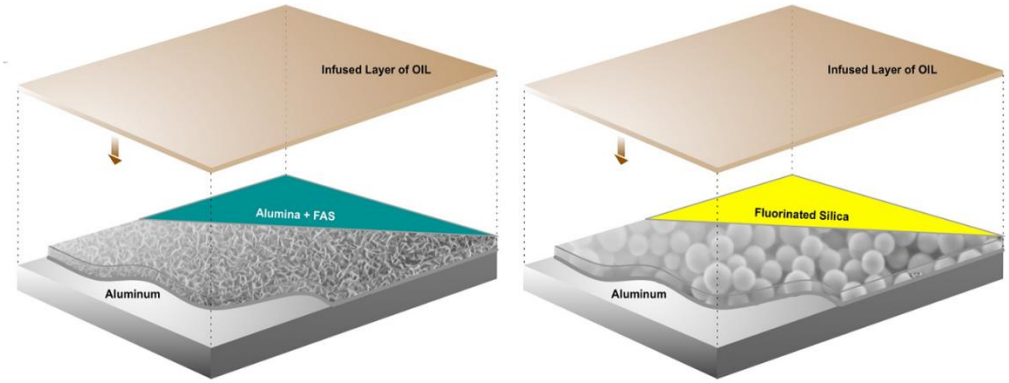

Figure 15. Schematic drawing of the process used to obtain SLIPS

2.6 Wetting Models and Anti-wetting properties characterization

The first study concerning wetting properties was developed by Young (1 tesi fede), published in 1805. However, he never formalized his theory. It was Gauss [150] who wrote the Young equation for the first time in 1830:

$$\cos\theta = \frac{\gamma SG - \gamma SL}{\gamma LG}$$

Where θ represents the contact angle, γSL is the interfacial tension between solid and liquid phases, γLG is the interfacial tension between liquid and gas phases (also known as liquid surface tension) while γSG is the solid surface energy (SE). All the forces interact at the three-phase contact line. The contact

angle θ is defined as the angle formed by the tangent to the liquid-gas interface at the three-phase contact line [5]. In Figure 16 is shown a schematization of all the below cited forces which contribute in the contact angle:

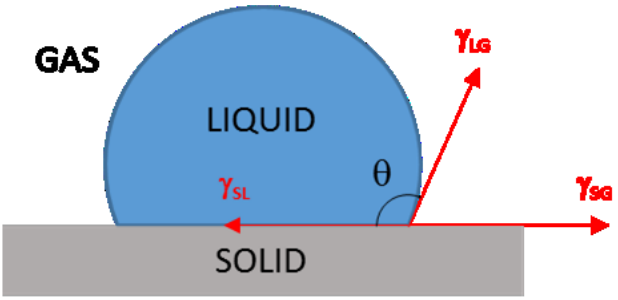

Figure 16. Diagram of the three-phase line of a liquid drop on a solid surface

From contact angle we can define hydrophobic a surface which presents θ > 90°, while if θ < 90° the substrate exhibits a hydrophilic nature.

Young equation is validated only for smooth surfaces. If the substrate presents roughness the liquid can penetrate between the features. The first study concerning rough surfaces were carried out by Wenzel, which developed a new theory based on the studies of not smooth and homogeneous surfaces. In his work he demonstrated that in rough surfaces, the solid-liquid interfacial area is increased by a roughness factor *r*, defined as the ratio between the actual contact area and the geometric one.

Such situation is defined as Wenzel wetting state and the relative Wenzel equation is:

$$cos\theta w = r * cos\theta$$

The schematization of the Wenzel Contact Angle is shown in Figure 17:

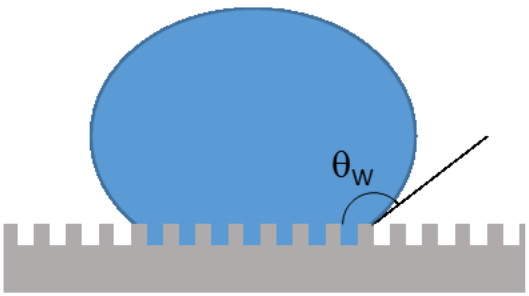

Figure 17. Sketch of a liquid drop resting on a rough surface in Wenzel wetting state

By Wenzel equation, it is clear that an increase of surface roughness led to an enhancement of Contact angle. In the case of superhydrophobic materials the θ has to be higher than 150° and the achievement of this performance is facilitating by roughening the surface.

If the surface presents a peculiar combination of morphology and chemistry the liquid is not able to penetrate inside the surface features. This phenomenon is due to the formation of air pocket trapped between the

structural voids of the surface, acting as a barrier against liquid penetration and wetting.

By this way a solid-liquid-air interface is formed, described by Cassie and Baxter [2] by the following equation:

$$\cos\theta CB = f1cos\theta 1 + f2cos\theta 2$$

The drop deposited in a Cassie-Baxter wetting regime surface is shown in Figure 18:

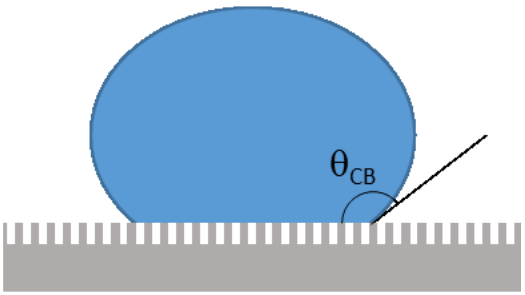

Figure 18. Sketch of a liquid drop resting on a rough surface in Cassie-Baxter wetting state.

In the equation, *f1* and *f2* are the surface fractions with phase 1 and phase 2, respectively. θ*1* and θ*2* are the contact angles (as per Young equation) of the liquid on phase 1 and phase 2. If phase 1 is the solid and phase 2 is air, then θ*2* = 180°. Furthermore, if no other phase is present and interfaces are planar [151], *f2* = 1 – *f1*. Therefore, Cassie-Baxter equation becomes:

$$\cos\theta_{CB}=f(1+cos\theta)-1$$

As per Cassie-Baxter equation, the smaller the value of *f*, the larger the value of θ_{CB}.

Both Wenzel and Cassie-Baxter models have some limits. For example, the latter considers a flat liquid-gas interface beneath the drop, but Herminghaus [152] introduced some corrections accounting for smaller-scale roughness superimposed on the surface structure. This correction is useful to explain the wetting behavior of hierarchically structured surfaces. Milne and Amirfazli tried to reconsider the common use of Cassie-Baxter equation [151], showing that for non-planar interfaces $f2 \neq 1 - f1$. Spiked surface asperities, high hydrostatic pressure and partial penetration of the liquid in the larger scale features of surface morphology are some of the reasons that lead to non-planarity of liquid-gas and liquid-solid interfaces. The authors suggested using the original form of the Cassie-Baxter equation, in which the sum of the area fractions *f1* and *f2* is greater than or equal to 1:

$$\cos\theta_{CB} = f1\cos\theta 1 - f2$$

Gao and McCarthy even tried to confute Wenzel and Cassie-Baxter models [153]. They brought evidence that the observed contact angle depends on the interplay of tension forces at contact line, rather than contact area. Eventually, much more refined wetting models were elaborated [154]. Nonetheless, Wenzel and Cassie-Baxter models remain the most widely used ones for the description of wetting behavior on solid surfaces.

Transition between different wetting states is highly debated in literature. Many works [151,155] focus on quasi-static conditions, identifying a critical contact angle θ_{cr}:

$$cos\ \theta_{Cr} = \frac{-f_2}{r - f_1}$$

A surface needs to have intrinsic (Young) $\theta_1 > \theta_{cr}$ to make Cassie-Baxter state thermodynamically favored over Wenzel state. This criterion shows how a proper design of surface morphology can lead to the desired wetting properties. However, such quasi-static conditions do not represent what happens in real wetting conditions. During operation, liquids drops strike surfaces with non-zero velocity, thus applying a relevant pressure. If we consider a rough surface favoring Cassie-Baxter wetting, air is trapped within its features. One can calculate a related capillary pressure P_C, which the surfaces opposes against wetting by impacting drops [156]:

$$P_c \propto \gamma_{LG} = \frac{-\cos \Theta_A}{r_p}$$

In the equation, γ_{LG} is liquid surface tension, θ_A is the advancing contact angle (defined in the next section) of the smooth surface and r_P reflects length scale of the cavities on the surface. The smaller the cavities on the surface, the higher is the anti-wetting pressure exerted by the surface. If impinging drops can overcome this pressure, liquid phase will replace air within surface features and an irreversible Cassie-to-Wenzel transition will occur. Therefore, the wetting state of a surface depends on many aspects, which must be considered while designing the surface.

Using SLIPS the concept does not change, considering the lubricant layer as a smooth surface governed by the Wenzel wetting model. The difference is due to the dynamic behavior of the drop; in a typical Wenzel surface the water is strongly stick to the material with high values of CAH. On SLIPS water and the lubricant oil are immiscible which lead to a complete absence of adhesion between. The drop deposited on lubricated surfaces is schematize in Figure 19:

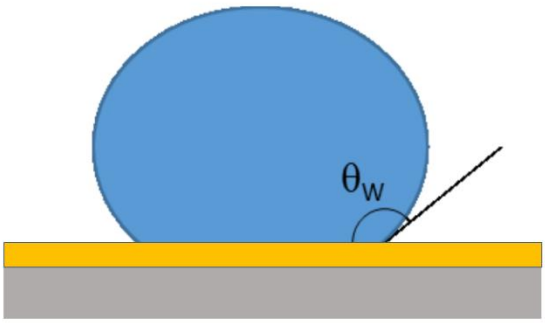

Figure 19. Sketch of a liquid drop resting on a lubricated surface in a Wenzel state regime.

During my Ph.D project the wetting behavior of the prepared surfaces was characterized in term of Static Water Contact Angle (WCA) and Contact angle Hysteresis.

There are many methods for contact angle measurement [101], but the most widespread one is sessile drop method. This technique is simple and many commercially available, automated systems can perform it in a very short time with good reproducibility. In this technique, a liquid drop of known volume is deposited on the surface. A light source (e.g. a lamp) irradiates the

drop from a side, projecting an image in the objective of a camera. In automated systems, a software automatically detects drop profile and fits it with the chosen method. The angle between the baseline and the tangent to the fitting curve in the contact point is the measured contact angle.

For an ideal surface (e.g. homogeneous, rigid, smooth, chemically inert), the contact angle with a certain liquid is constant and depends only on interfacial tensions as described by Young equation. However, real surfaces will always be chemically inhomogeneous and/or rough. For this reason, apparent contact angle will assume different values over the surface. Furthermore, if the drop is inclined or its volume changes in time, two different angles will be observed: the advancing contact angle ACA, referred to the movement of contact line towards a non-wetted area; the receding contact angle RCA, referred to the movement of contact line towards a wetted part of the surface [101]. It will always be true that ACA ≥ RCA. The difference ACA - RCA is called contact angle hysteresis CAH and is related to drop mobility on the surface: the lower CAH, the higher the mobility. Contact angle hysteresis is the main tool to recognize a Wenzel state from a Cassie-Baxter state: in the sooner, the liquid phase penetrates surface structures and is firmly pinned, thus has high CAH. On the other hand, Cassie-Baxter drops are free to move on the mixed solid-gaseous surface, therefore hysteresis will be low, usually below 10°. As already hinted, there are mainly two methods for measuring ACA and RCA. The first one consists in depositing a drop on the surface and tilt it until the drop starts to move. At the onset of movement, the contact angle measured uphill is RCA, the angle measured downhill is ACA. This is

the tilted plate technique [157]. However, the most common method for the measurement of CAH is based on a sessile drop still technique. Drop volume is increased by injection; the CA value observed when the contact point starts to move is defined as ACA. This value should be constant as drop volume increases over a certain threshold. Then, drop volume is decreased by suction and the contact line starts to recede. From that moment on, the plateau value of θ is RCA. An example of ACA and RCA measurement is reported in Figure 20:

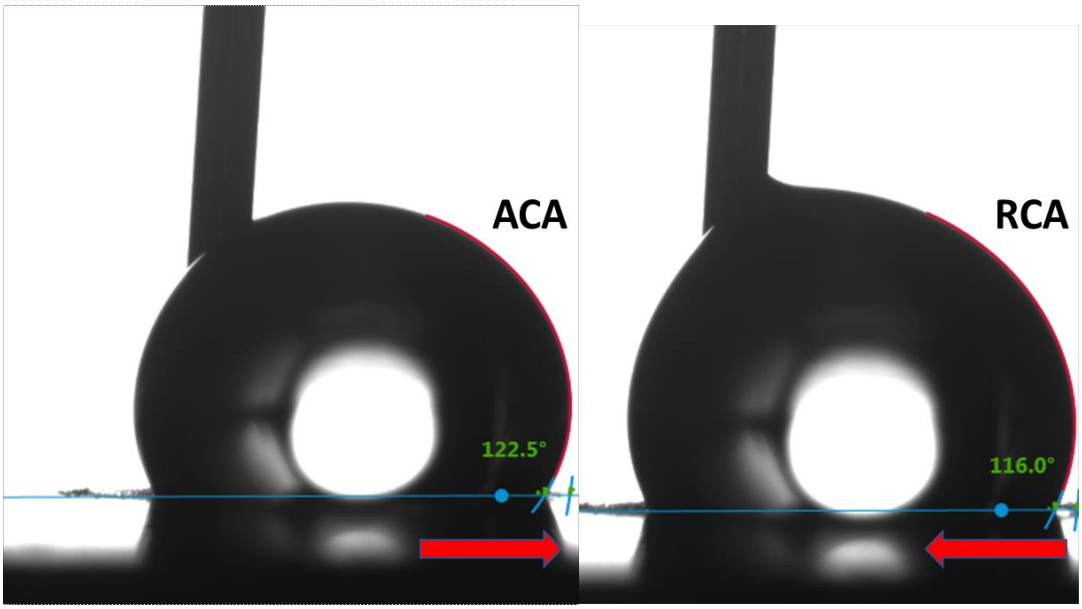

Figure 20. Measurement of advancing (left) and receding (right) contact angle for a water drop on a surface.

The characterization of both WCA and CAH was carried out using a drop shape analyzer (DSA) purchase by Kruss (Germany), shown in Figure 21:

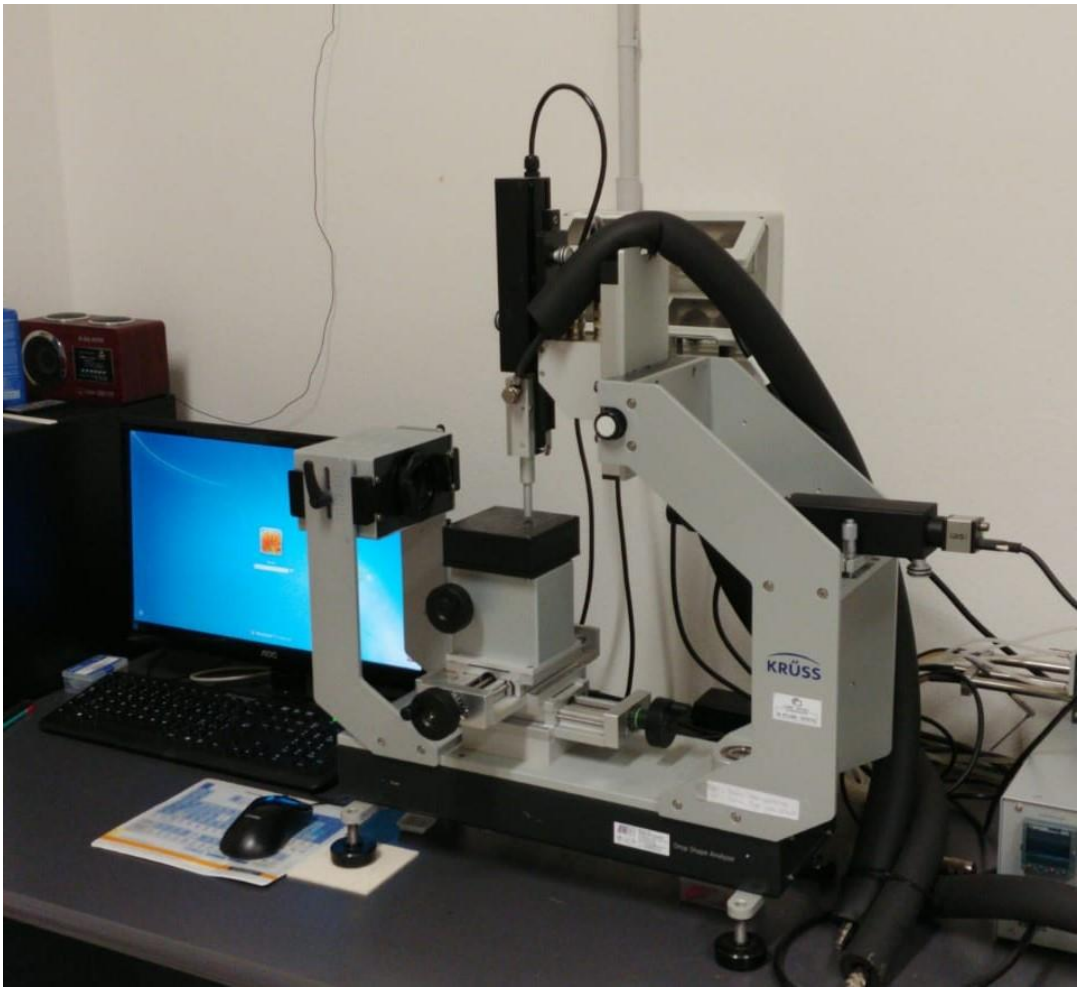

Figure 21. Drop Shape Analyzer instrument (DSA30, Kruss, Germany)

The instrument is equipped with an automatized dispense compartment which included the needle and the motorized volume controller. The needle is able to move in vertical while the stage allows the movement in the horizontal axes for the complete mapping of the characterized surfaces. The drop visualization is carried out by a CCD camera linked with a CPU. The software is able to fit the drops giving WCA and CAH values. In my project

I used drops volume of 10 μL for both static and dynamic contact angles using the fitting method named *"tangent leaning"* [158].

2.7 Anti-icing abilities assessment

The anti-icing properties of the materials prepared during my Ph.D. project were evaluated via different test:

- Anti-wetting behavior at T lower than 0°C
- Ice nucleation delay at T = -5°C
- Ice adhesion test
- Icing wind tunnel test

2.7.1 Anti-wetting behavior a T lower than 0°C

The WCA and the CAH of coatings were evaluated at temperatures of -2.5, -5, -7.5 and -10 °C via goniometric analysis. To reach the analysis temperature, the samples were placed in an environmental chamber equipped with a Peltier plate (Temperature Control Chamber TC40, Krüss GmbH). The Peltier system is liquid-cooled with a thermo-cryostat AC150 immersion circulator (Thermo Scientific) able to control the temperature in a range from -20 to 80 °C. Surface temperature was monitored with a built-in Pt100 thermocouple. The temperature of water droplets was set at 5 °C. The apparatus is shown in Figure 22:

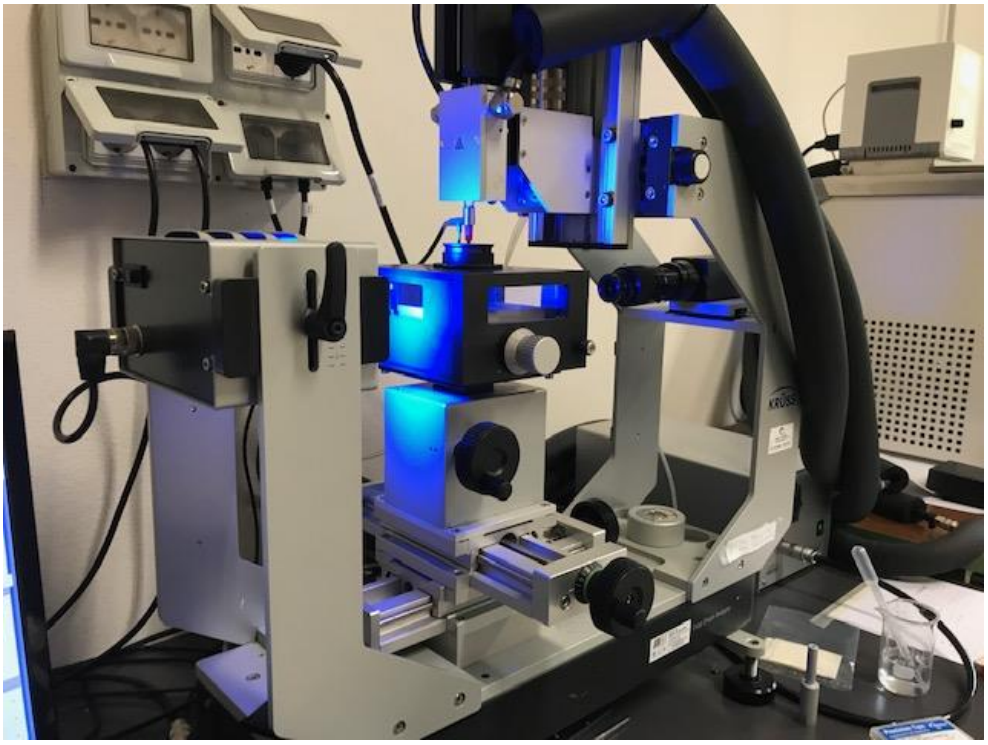

Figure 22. Drop shape analyzer equipped with Peltier chamber which allows the temperature control

The static water contact angle was evaluated via sessile drop method depositing the liquid when the thermocouple indicated the right analysis temperature. To fit the drop the *"tangent-leaning"* fitting method was adopted. After the measurement the Peltier plate was extracted from the chamber and put in an oven at 100°C to limit as better as possible the humidity content in the analysis environment. For each sample, 3 measures were performed for all the temperatures took into account.

Contact angle Hysteresis was carried out using the same procedure described before in the thesis, exploiting the calculation of ACA and RCA. The values of CAH are an average of 3 measures for each sample at the

different temperatures adopted for the test. As for the static WCA, between two different measurements the plate was put in an oven to eliminate the moisture excess.

2.7.2 Ice nucleation delay at T = -5°C

The delay of ice nucleation on anti-wetting surfaces was evaluated via optical and video analysis using the same equipment adopted for the anti-wetting ability test at temperature lower than 0°C. The samples were placed in the Peltier chamber and the temperature was drop down to -5°C using the T controller. The syringe was cooled at 5°C and the drops had a volume of 10μL. When the Peltier plate reached the proper temperature, the drop was dispensed and the video recording was activated. As soon as ice nucleation starts the test is complete and the time from the drop deposition and the formation of ice nuclei was taken as ice nucleation time. After a first cycle of measurement the experiment was interrupted due to the poor reproducibility of the measure. The cause of this is the formation of an quasi-equilibrium of the liquid water in supercooling environment, which can remain in a liquid state until -40°C in absence of some external perturbation able to ignite the ice nucleation and growth [46]. With the absence of control of the external perturbations it is impossible to have a good enough reproducibility of the tests so we decided to interrupt the analysis after the first cycle of ice nucleation delay calculation.

2.7.3 Ice adhesion test

The substate adopted for ice adhesion test is shown in Figure 23:

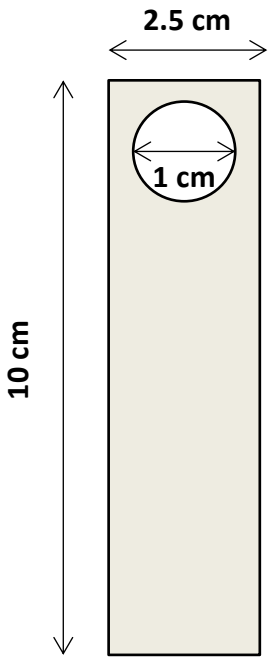

Figure 23. Schematization of the substate used for ice adhesion tests

The coatings which underwent to ice adhesion tests are reported in Table 4:

Table 4. Composition of coatings for ice adhesion tests

Sample	Inorganic layer	Organic layer	Lubricant
Al_2O_3Kr103	Alumina	FAS	Krytox™ GPL 103
Al_2O_3Kr105	Alumina	FAS	Krytox™ GPL 105
SiO_2F SO10	Fluorinated Silica	/	Silicone oil 10cSt
SiO_2FKr103	Fluorinated Silica	/	Krytox™ GPL 103
SiO_2FKr105	Fluorinated Silica	/	Krytox™ GPL 105

To standardized the experiment the samples were polished in order to have a constant surface roughness of 0.5 μm. After the deposition of all the designed coatings the samples were send to INTA, located in Madrid to perform the ice adhesion experiments. The Institute is equipped whit an Instrom 5882 Universal Machine (Barcelona, Spain) with a 5 KN loading cell placed inside a climate chamber (refrigerated with liquid nitrogen), used to performed the proves. The loading cell was calibrated in the 5%–95% range. The ice layer on the surface of the coupons was formed inside an ultra-low temperature freezer (Arctiko ULTF series).

The day before the test, ice was formed on the samples employing the following procedure: initially, the sides of the test block were sealed with transparent adhesive tape to prevent water from leaking, then the mold was filled with water and finally, the specimen was placed inside ensuring that

the level of water on both sides of the specimen was the same, reaching 6 mm below the top edge of the mold (Figure 24a). The surface was then placed in a low temperature fridge at −10 °C (Arctiko ULTF series) for 16 h before the test.

One hour before the test, the adhesive tape was removed, and the rest of ice accreted over the sample edges was carefully, but quickly, removed using a blade. The molds were placed again in the freezer for one more hour.

The test block was then fixed to the universal machine, previously cooled to the test temperature (Figure 24b). After the selected test temperature was reached in the chamber, the samples were left for five more minutes before beginning the test.

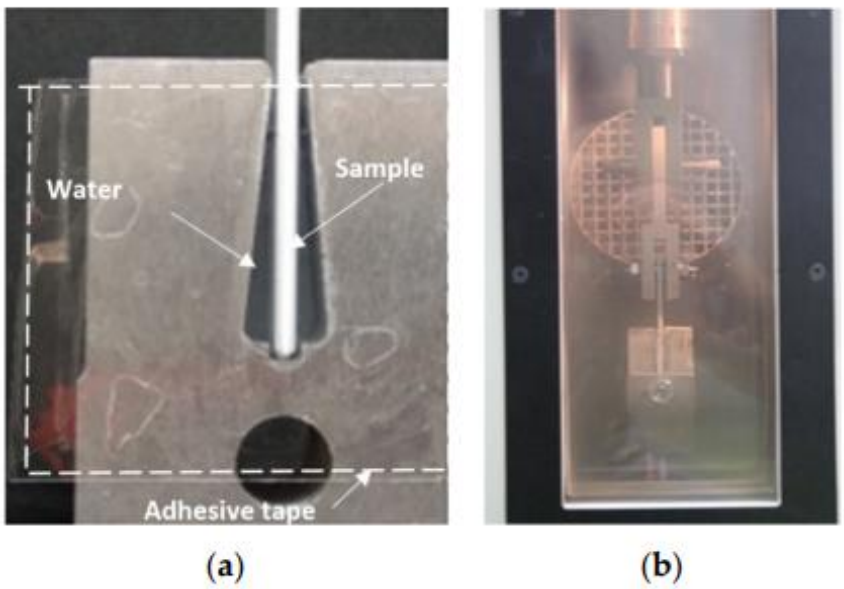

Figure 24. (a) Test block employed to form ice on both sides of the sample. (b) Block attached to the Universal machine ready to start a test. [159]

The displacement speed was set, and the test initialized until the sample was completely out of the mold.

Plots of the measured load (N) as a function of displacement (mm) were obtained during the test, and the maximum load peak is the load needed to overcome the adhesion strength, therefore a measure of the adhesion between ice and the surface of the sample in the corresponding ice accretion conditions. Three specimens of every coating were tested to obtain the mean value and the standard deviation. Bare substrate, aluminum alloy typically used for aircraft features production (AA6061-T6) and foils coated with PTFE usually exploited as anti-icing passive method in aeronautic field) are used as references.

2.7.4 Icing Wind Tunnel (IWT) tests

As for the ice adhesion test, also icing wind tunnel instrument is located in INTA which performed all the experiments on its facility.

NACA 0012 wing profiles with a roughness of 0.5μm were adopted as substate for the tests in the tunnel. After the deposition of the anti-wetting coatings the samples was characterized in INTA, in terms of ice accumulation reduction if compared whit bare aluminum profiles.

The coatings deposited for icing wind tunnel test are listed in Table 5:

Table 5. Composition of coatings tested in Icing Wind Tunnel

Sample	Inorganic layer	Organic layer	Lubricant
Al_2O_3Kr103	Alumina	FAS	Krytox™ GPL 103
Al_2O_3Kr105	Alumina	FAS	Krytox™ GPL 105
SiO_2F SO10	Fluorinated Silica	/	Silicone oil 10cSt
SiO_2FKr103	Fluorinated Silica	/	Krytox™ GPL 103
SiO_2FKr105	Fluorinated Silica	/	Krytox™ GPL 105

The test section of the icing wind tunnel is shown in Figure 25:

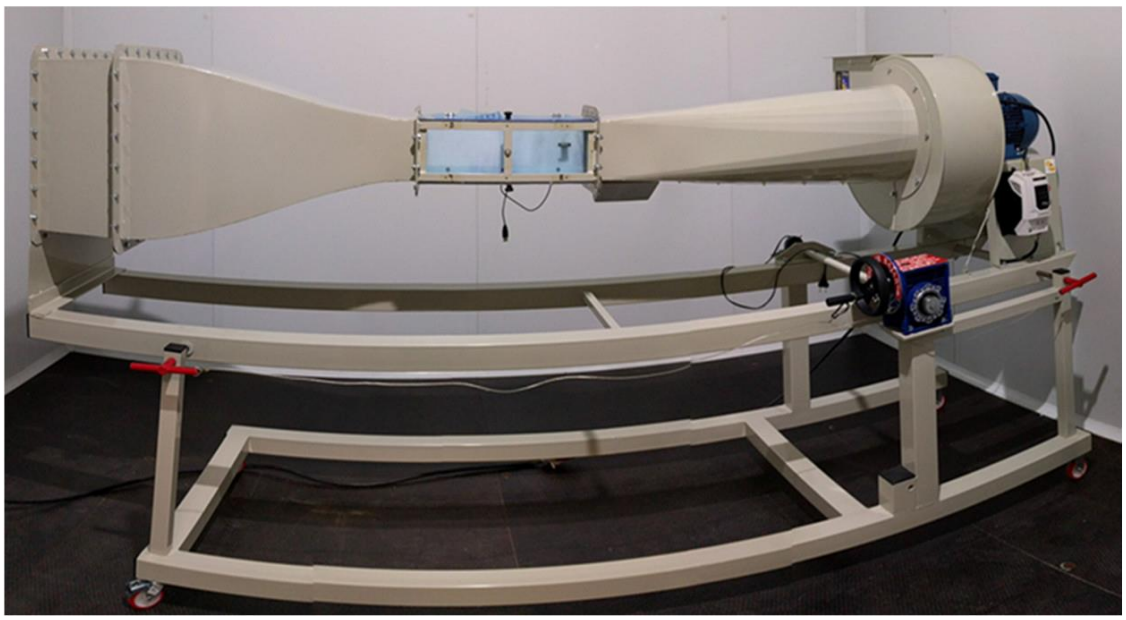

Figure 25. Icing Wind Tunnel test section.

The instrument is located in a cold climate chamber that allows temperature stability during the tests. The precooled samples were fixed in the center of the chamber (15 x 15 cm^2). Two icing conditions were simulated: glaze and rime ice regimes.

The parameters of both tests are highlighted in Table 6:

Table 6. Adopted parameters to test materials in graze or rime ice regimes

Regime	Temperature (°C)	Median Volume Diameter (MVD, μm)	LWC (g/m3)	Wind speed (m/s)
Glaze ice	-5	20	1	50
Rime ice	-10	20	0.5	50

The wind speed was measured using a PCE-PFM 2 probe with a range from 1 to 80 m/s and an accuracy of 2.5%. The MVD was evaluated using a Malvern Spraytec system, equipped with a 300 mm lens able to measure droplets from 0.1 to 900 μm and determine MVD from 0.5 to 600 μm in sprayed atmospheres, with an accuracy of 1%. LWC was calculated via icing blade method [160].

Five one-minute trials of each sample were performed in each condition (rime and glaze), and the ice accretion was evaluated by direct weight measurement before and after the experiment.

The mean values of the five measurements were used to compared the behavior between the coated samples and the bare NACA profile, used as reference.

2.8 Durability tests

Since the liquid repellent surfaces described in this paper are expected to be applied at subzero temperature, they were subjected to freeze/ and frost/thaw cycles performed, respectively, in presence or absence of liquid water in contact with the samples. For each condition, the total number of cycles was equal to 10 and they were established in order to evaluate the resistance with respect to the final use environment. Three samples per type were tested to guarantee reproducibility.

In the freeze/thaw cycles, a plastic cylinder was placed on the surfaces and water was poured inside with a liquid column of about 1 cm. Then the samples were transferred into a lab freezer at a temperature of -10 °C ± 1 °C and kept there for 3 h. After, the samples were taken out, ice was allowed to melt and the surfaces were subjected to WCA and CAH measurements.

The experimental set up is represented in Figure 26:

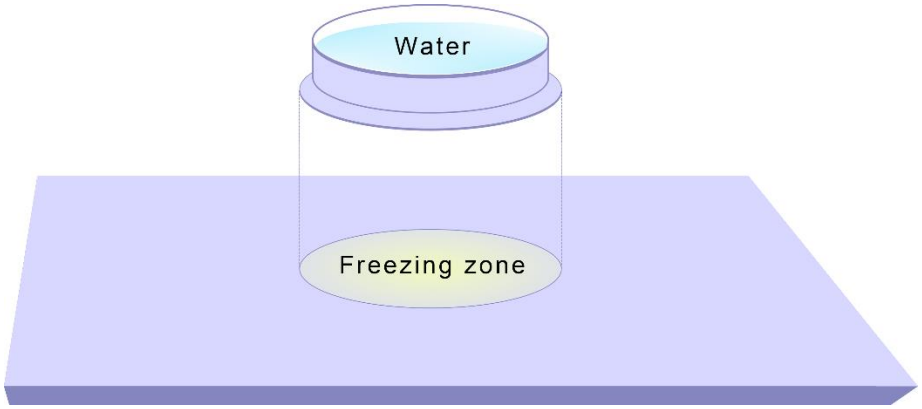

Figure 26. Experimental set up for freeze/thaw test. Water contained in the plastic cylinder was allowed to ice in contact with the surfaces.

In the case of frost/thaw cycles, sample surfaces were simply kept in a lab freezer at T of -10 °C ± 1 °C for 3 h, allowing frost formation Then, the samples were taken out, ice was allowed to melt and the samples were subjected to WCA and CAH measurements.

3. Results and discussion

3.1. Wetting behavior at room temperature and surface morphology

The wetting data of the different coating typologies are shown in Table 7 together with those referring to an uncoated aluminum surface taken as reference.

Table 7. Average static contact angle with water (WCA) and contact angle hysteresis (CAH) at T_{amb}

Sample	WCA (°) ± σ (°)	CAH (°) ± σ (°)
Uncoated sample (Ref.)	89 ± 2	59 ± 7
LF	171 ± 2	7 ± 2
Al_2O_3 Kr100	121 ± 1	2 ± 1
Al_2O_3 Kr103	122 ± 1	3 ± 1
Al_2O_3 Kr105	119 ± 2	9 ± 1
SiO_2F SO10	112 ± 2	10 ± 2
SiO_2F Kr100	123 ± 4	6 ± 2
SiO_2F Kr103	123 ± 4	6 ± 2
SiO_2F Kr105	119 ± 5	9 ± 1

LF samples clearly stand out for their super-hydrophobic and behavior brought about by the flaky structure of the oxide coating and the low surface energy molecules.

WCA of LF surfaces reached values of about 170 ° and CAH < 10 °. Meanwhile, SLIPS samples showed WCA values as high as 120 ° and CAH in any case equal to or lower than 10 °. This effect is due to the change of working interface from solid-liquid-air typical for LF samples to liquid-liquid for SLIPS. The water drop deposited on the lubricant liquid layer have a first settling which leads the WCA drop to values close to 120°. On the other hand, SLIPS exhibited an outstanding dynamic repellence, with complete absence of drop adhesion on it. The deposition of the lubricant oils also increases the homogeneity of the coating with respect to LF composition which presents some sticking phenomena on some points of the surface.

The wetting behavior of SLIPS is linked with the chemical-physical characteristics of the adopted lubricants oils and in particular surface tension and viscosity, shown in Table 8:

Table8. Surface tensions (γ) and viscosity (μ) of the four lubricants used for the fabrication of SLIPS.

Lubricant Oil	**γ (mN/m) ± σ (mN/m)**	**μ (cSt)**
Krytox™100	16.60 ± 0.04	12.41
Krytox™103	17.41 ± 0.01	821
Krytox™105	18.35 ± 0.08	5221
Silicone Oil 10cst	20.01 ± 0.30	9-112

[1]Chemours Technical Specifications of Krytox™ GPL series oils;
[2]Sigma-Aldrich Product Specification Sheet.

More in detail, while the different viscosity of Krytox™ oils seems not to affect the static performance (WCA) of coated surfaces, their dynamic behavior is optimized (CAH as low as 2-3 °) when low viscosity lubricants (Kr100 and Kr103) are infused. On these surfaces, drag forces against the sliding of the water drops are particularly reduced so that the sticking of the liquid can be almost completely avoided.

Silica-based SLIPS infused with Krytox™ GPL oils exhibited quite the same wetting behavior compared with the Al_2O_3-based SLIPS samples. Using silicone oil as lubricant leads to a little decrease of WCA to 112 ° and a slight increase of CAH to 10 ° respectively. The decrease of WCA might be explained considering the surface tension, γ, of the different oils. Silicone oil has a slightly higher γ than Krytox™ oils (see Table 7). As known in

literature, the higher the gap in surface tension between the lubricant and water (γ = 72 mN/m at T = 20 °C), the higher the WCA.

As shown in the table, silicone oil has a higher surface tension than Krytox™ oils which means a lower gap in γ between water and the lubricant. This leads to a decrease of anti-wetting performance for SiO_2-based SLIPS infused with silicone oil, anyway these surfaces maintained an acceptable degree of both static and dynamic repellence.

Figure 27 shows the morphology obtained after deposition of alumina layer. Alumina nanoparticles, after the structuring process in boiling water, lead to the formation of the typical hierarchically organized "flower-like" structure. The surface structure presents voids with dimensions of about 50 nm [161] able to host and trap either air pockets (LF surfaces) or lubricants (SLIPS).

The following functionalization with FAS molecules did not alter the coating morphology. FAS molecules form a monolayer on boehmite surfaces, as demonstrated in a previous work of my research group [162].

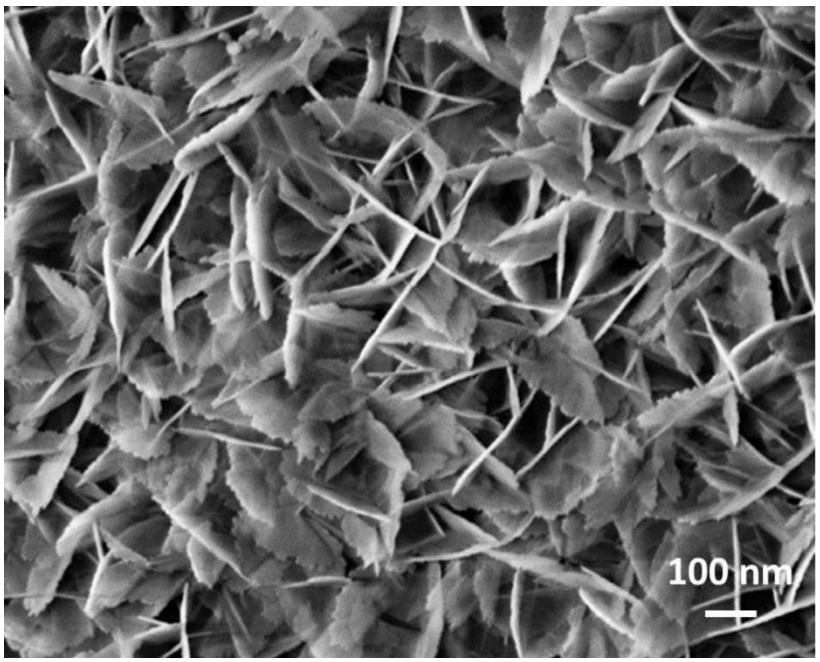

Figure 27. Micrograph of nanostructured Al_2O_3 inorganic layer.

Figure 28 shows a finer detail of a nanoflake on the boehmite surface. This lamella was expected to be just few nanometers thick.

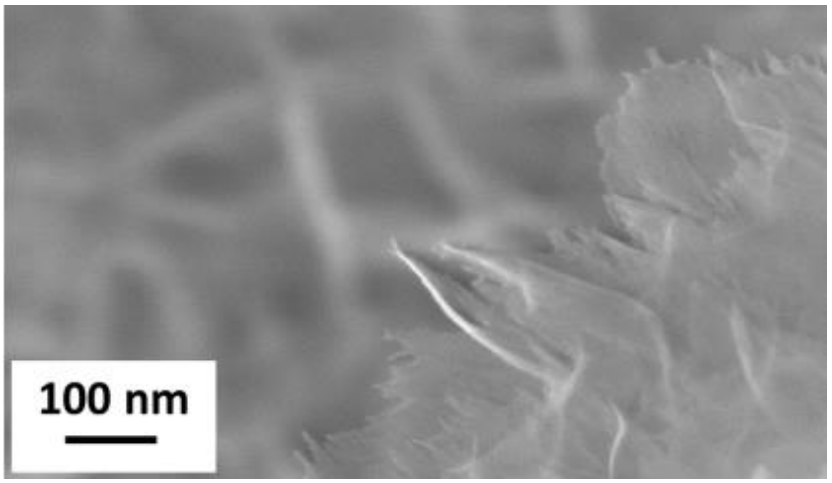

Figure 28. FESEM image at high magnification of a single lamella in the flower-like boehmite nanostructure.

The average thickness of the Alumina-based coating is about 500nm, as shown by the Figure 29:

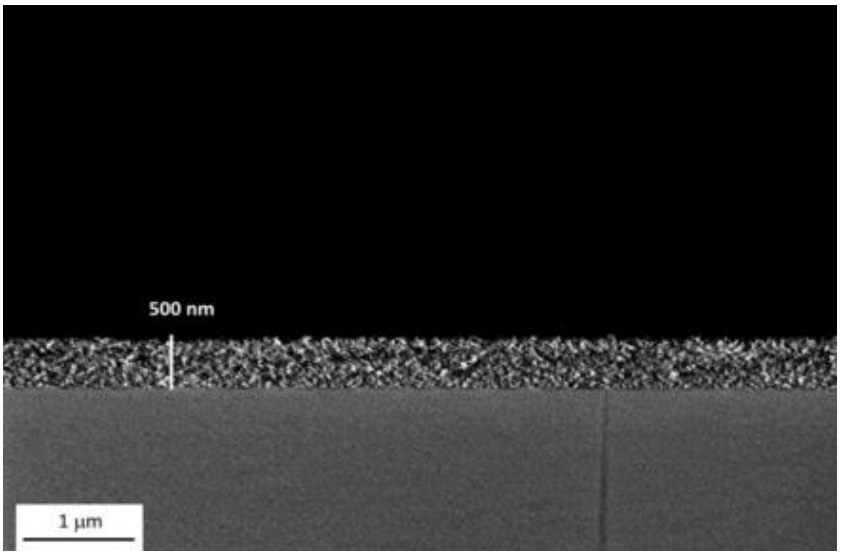

Figure 29. FE-SEM image of the boehmite film thickness

The deposition of fluorinated silica involves the formation of nanoparticle agglomerates well distributed on the whole surface area, as shown in Figure 30:

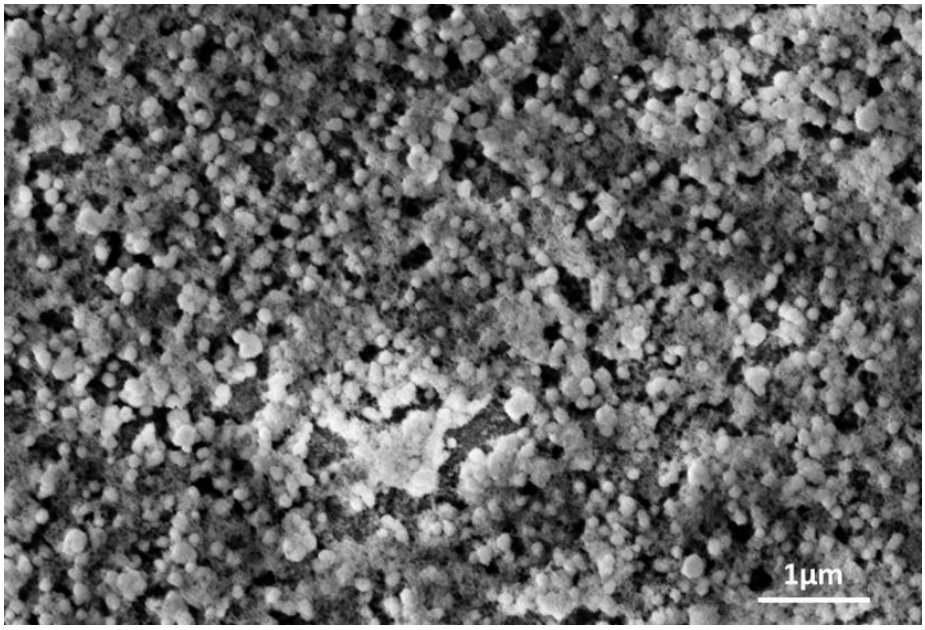

Figure 30. Micrograph of nanostructured SiO_2 inorganic layer.

The coating thickness of the Silica-based coating has not observed due to the impossibility to have a homogeneous cross section of the samples. As shown by the SEM image silica nanostructure presents large voids all over the surface, which could be not suitable for the infusion with fluorinated lubricants Krytox™ GPL. The large size of the holes (around 1µm) should lead to a decrease of the capillarity forces, fundamental to retain oils into the porosity. In order to foster oil retention, also weak interactions (e.g., van der Waals forces) can be exploit. Therefore, the chemical composition of the infused oil is also relevant to optimize retention. In this perspective, we chose to investigate also non-fluorinated moieties like silicone oil: due to its Si-O bonds, this liquid is expected to have high affinity for the silica nanoparticles. The effect of chemical composition of the oil on the coating performance will be discussed in the next chapters.

The samples were also observed via Atomic force microscopy; AFM measurements were acquired with an A.P.E. Research A100 microscope equipped with a closed loop sample positioning system. For what concerns tapping mode, the detection scheme of the AFM used is based on laser beam deflection off a microfabricated n-type silicon probe with stiffness of 40 N/m and length of 125 micrometers. Sample were characterized at ambient condition with a resolution of 256x256 pixel per image.

The Instrument utilized for AFM characterization is shown in Figure 31:

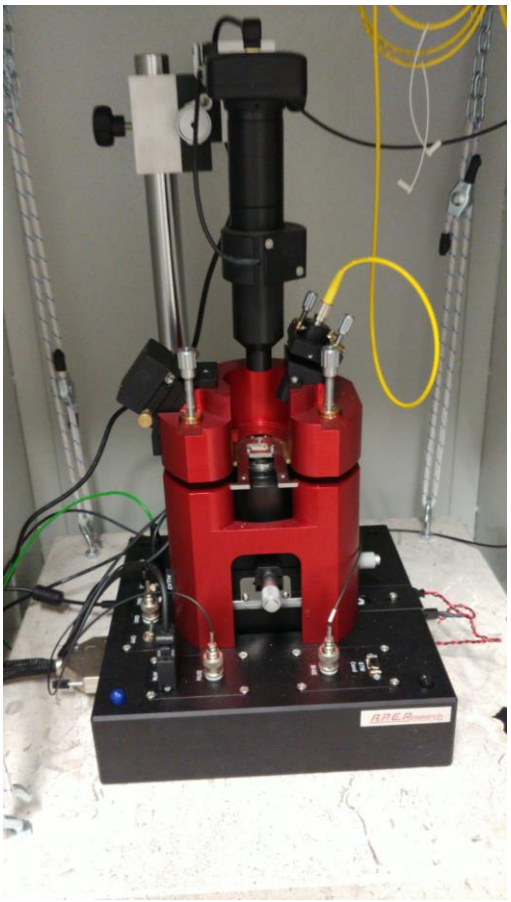

Figure 31. A.P.E. Research A100 microscope

Figure 32 shows the schematic drawing of the cantilever;

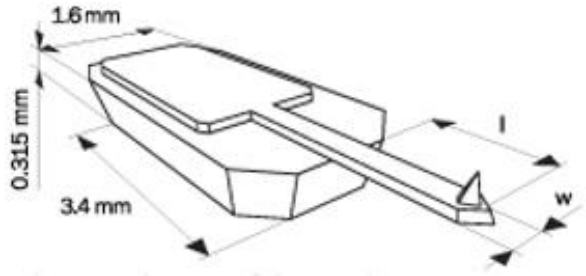

Figure 32. Schematic drawing of the utilized cantilever

The parameters adopted for the images acquisition are shown in Figure 33:

Cantilever	Resonance Frequency, kHz			Force Constant, N/m			Length l ± 5, µm	Width w ± 3, µm	Thickness t ± 0.5, µm
	min	**typ**	max	min	**typ**	max			
15 Series	265	**325**	410	20	**40**	80	125	30	4.0

Figure 33. Set parameters for AFM images acquisition

The AFM micrograph of Alumina-based coating is shown in Figure 34:

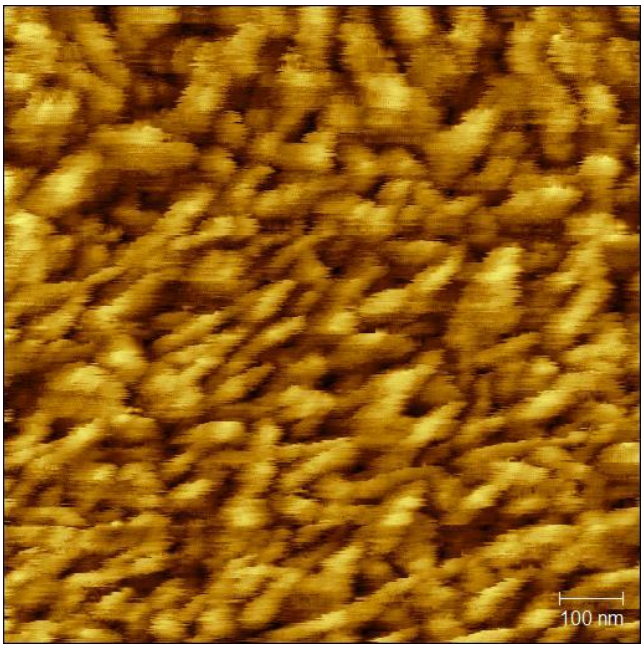

Figure 34. AFM image of "flower-like" hierarchical structure of Al_2O_3 coating

The acquired image clearly highlights the presence of the nano-flakes on the surfaces deposited with Alumina suspension, with a dimension of about 50nm, as exhibited before by SEM images.

Silica-based coating AFM image is shown instead in Figure 35:

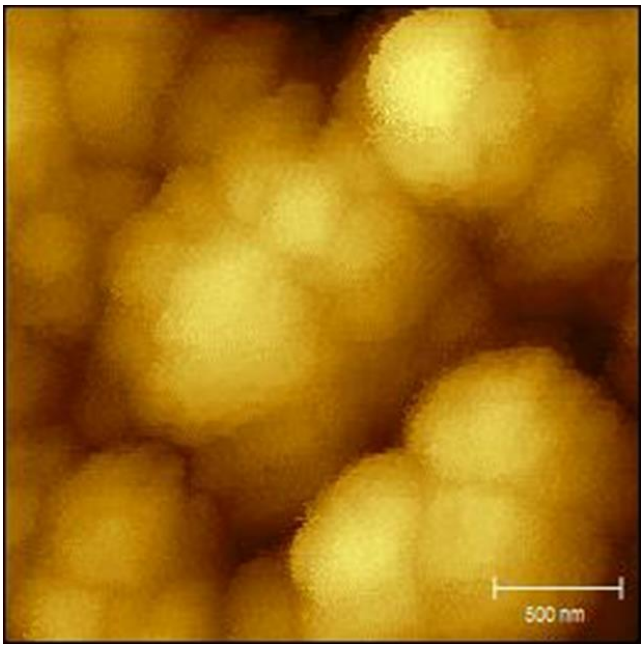

Figure 35. AFM image of SiO_2F coating

The micrograph exhibits the typical morphology obtained by deposition of fluorinated Silica suspension, made of NPs agglomerates which cover quite uniformly the surface. For both Alumina and Silica analysis, AFM acquisition confirmed the results obtained after SEM surfaces visualization.

3.2. Ice nucleation delay

The study of the ice nucleation delay was the first anti-icing test carried out during my Ph.D. project. The analysis was performed on Alumina-based coating infused in Krytox™ GPL series lubricant oil and fluorinated Silica-based surfaces infused with either Silicone oil and Krytox™ GPL lubricants.

The next figures (36-40) show the different moments of the freezing process, as recorded with the CCD camera of DSA Kruss; in particular, the snapshots related to drop deposition (t=0), beginning of ice nucleation and completion of drop freezing are reported for different surfaces.

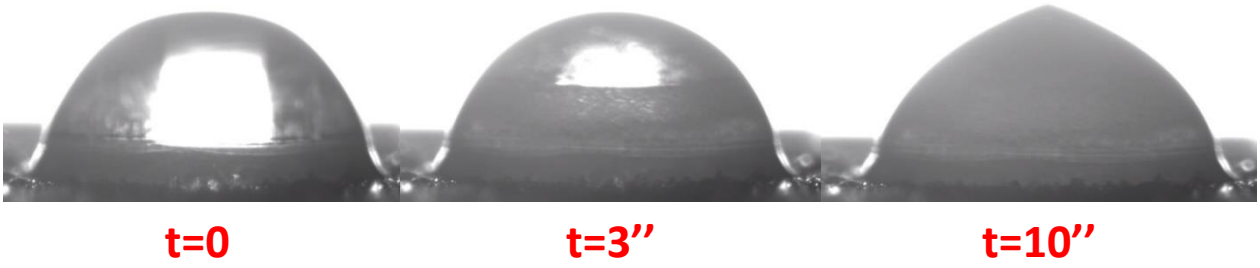

Figure 36. Drop freezing process on bare aluminum foil

Figure 37. Drop freezing process on LF surface

Figure 38. Drop freezing process on Al_2O_3 Kr100 surface

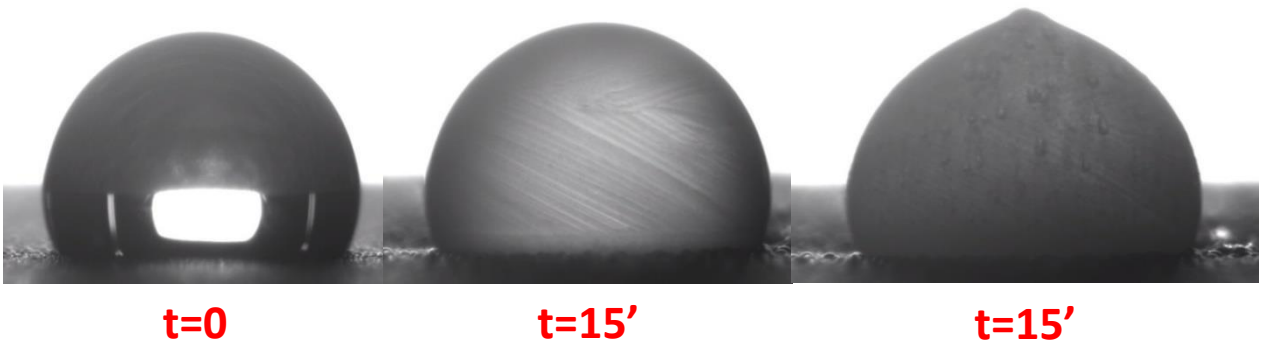

Figure 39. Drop freezing process on Al_2O_3 Kr103 surface

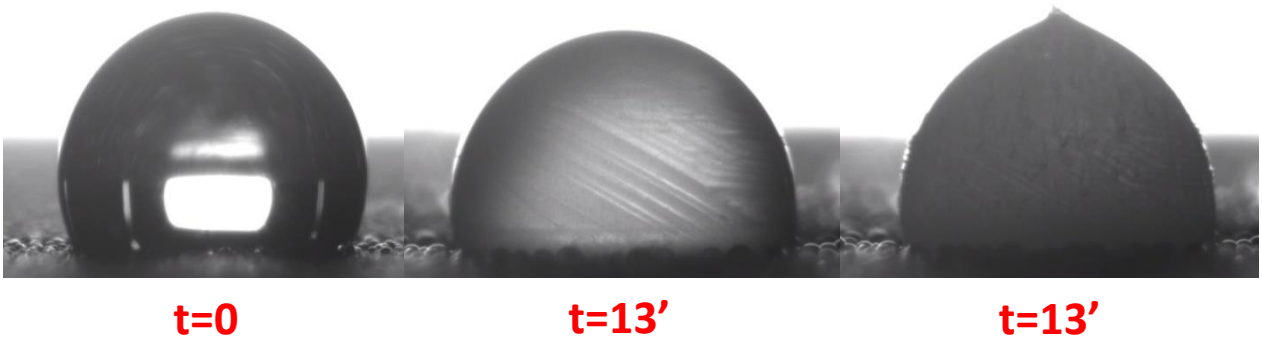

Figure 40. Drop freezing process on Al_2O_3 Kr105 surface

Silica-based coatings showed the same ice nucleation process as Alumina-based ones. The icing delay time, defined as the time interval between drop deposition and complete freezing, was calculated 5 times for each sample in order to evaluate the reproducibility and the coating resistance at the low temperature. In every run of icing delay test, heterogeneous nucleation has been observed, due to its lower activation energy barrier compared to the one of homogeneous nucleation.

The results of ice delay time tests are shown in Table 9:

Table9. Ice delay times of coated samples for each test repetition.

Sample	Icing delay 1°cycle (min)	Icing delay 2°cycle (min)	Icing delay 3°cycle (min)	Icing delay 4°cycle (min)	Icing delay 5°cycle (min)
Uncoated	0	0	0	0	0
LF	4	0	0	0	0
Al_2O_3 Kr100	13	10	5	18	7
Al_2O_3 Kr103	15	12	8	10	8
Al_2O_3 Kr105	13	10	9	12	5
SiO_2F SO10	13	15	3	3	5
SiO_2F Kr100	10	9	10	5	2
SiO_2F Kr103	17	23	11	10	6
SiO_2F Kr105	19	21	12	8	4

As shown by the Table 9, all the samples present an ice nucleation delay time in the first cycle with respect to the uncoated substrate, where the nucleation started in the precise moment the drop got in contact with the cooled surface.

LF sample had a delay time of 4 minutes during the first icing cycle while from the second one no delay was observed. This is probably due to the poor resistance at low temperature and the low mechanical resistance of the LF samples. During icing process the lamellae were flatted by the forming ice,

leading to a transition from Cassie-Baxter to Wenzel wetting regimes (Cassie-to-Wenzel transition, CWT) [36–39,66,70,163–166].

Such phenomenon consists in the loss of the air pockets trapped between the nanofeatures of the "flower-like" structure due to the penetration of the condensed water which replaced the trapped air, and the destruction of the hierarchical micro-nano structure. The change of morphology responsible of the CWT was observed via SEM analysis and will be shown in the chapter concerning the samples resistance to freezing/frosting cycles.

SLIPS samples maintained an ice nucleation delay for each test cycle but the delay time values are pretty inhomogeneous. The trend of the results is highlighted in the graphs show in Figures 41 and 42:

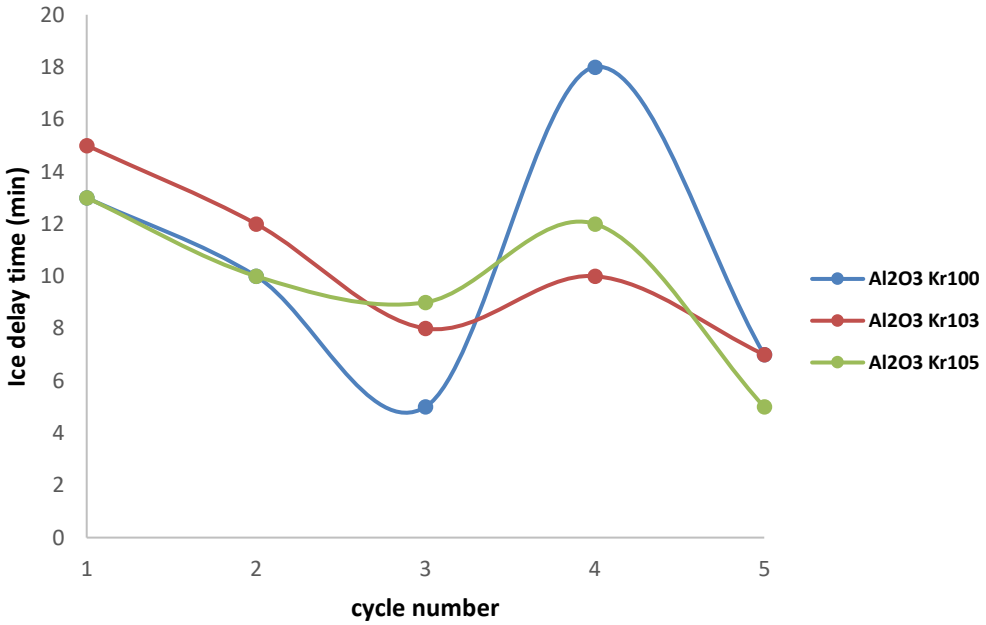

Figure 41. Ice nucleation delay time of Alumina-based coated samples along test cycles

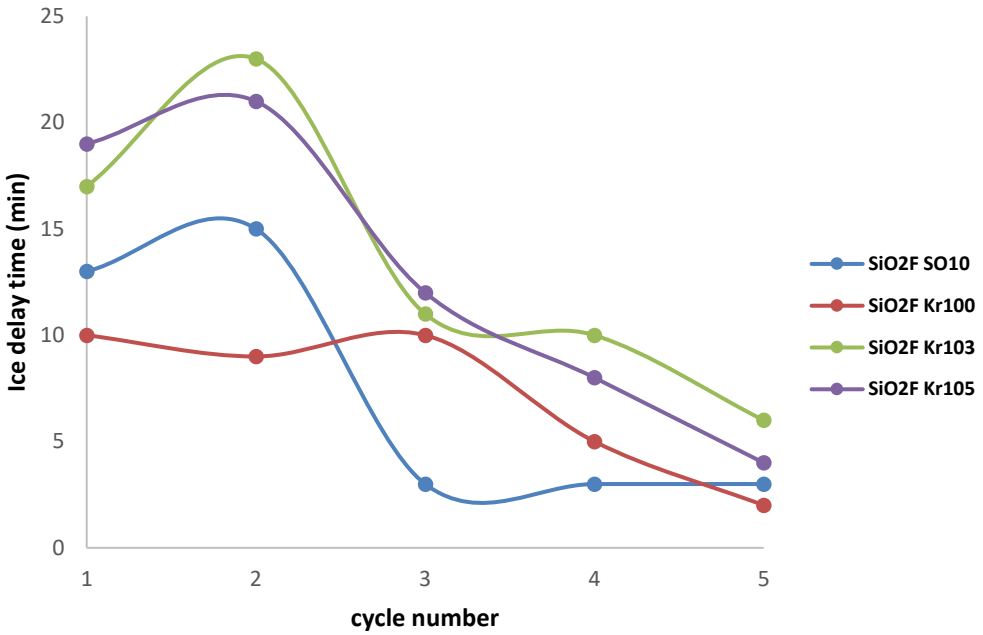

Figure 42. Ice nucleation delay time of Silica-based coated samples along test cycles

The graphs present very variable data, with poor reproducibility. This inhomogeneity should be due to the physical properties of water. It is known that liquid water can stay in a semi-equilibrium state in the liquid phase till -40°C [53]. To break this semi-equilibrium state, an external input is needed to overcome the activation energy. At the test temperature (-5°C) and without significant perturbation, water can remain in the liquid state for a very long time. For the other tested surfaces (uncoated and LF) the perturbation which ignite the ice nuclei formation could be the surface roughness which create low energy barrier nucleation point [93,167]. In the case of completely homogeneous SLIPS, the perturbation due to a morphology effect is not present, allowing liquid water to remain in the quasi-equilibrium discussed before in the thesis, and in absence of external

perturbation can remain in the liquid state until the temperature of -40°C. The nucleation should be due to other effects such us humidity variation or some oscillation in the Peltier plate temperature. For these reasons, it was not possible to adequately describe the effect of anti-wetting coatings in icing nucleation delay and this kind of analysis was abandoned after the first year and a half of the Ph.D. project.

3.3 Anti-wetting behavior at temperature < 0°C

The anti-wetting behavior of the designed surfaces at temperature lower than 0°C was evaluated via drop shape analysis using Krüss DSA30. Both WCA and CAH were calculated in a range of temperature from -2.5°C to -10°C.

The average values of WCA detected on the different coated samples in this temperature range are collected in the histogram of Figure 43 (WCA @T < 0 °C, green bars). WCA of each surface coating was stable over this range of temperatures. The spreading and retraction dynamics of the droplets at subzero temperatures are instead reported in Figure 36 showing the CAH values. The retraction dynamic of drops is particularly interesting. The change in the receding contact angle resulting from ice nucleation de facto reduces the surface tension–based retraction force that acts radially inward. Such force mimics the desired de-wetting behavior [168].

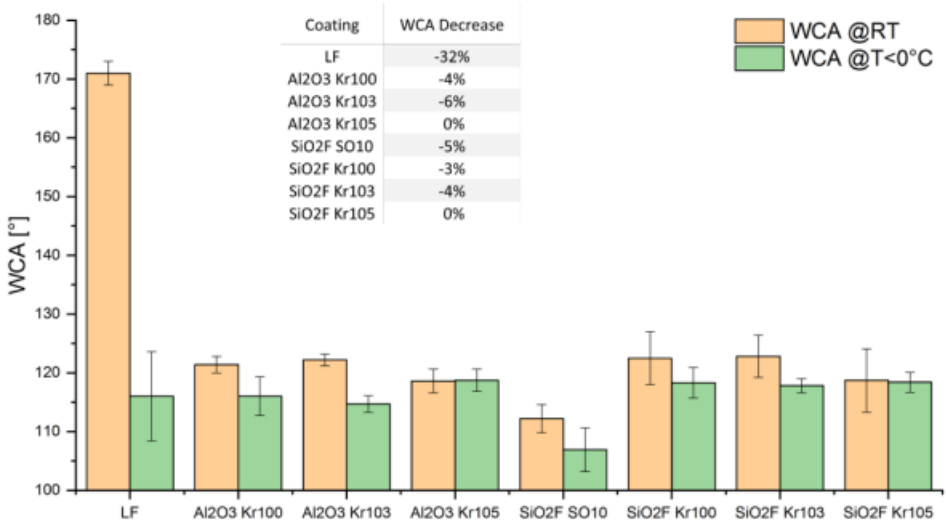

Figure 43. Static Water Contact Angle (WCA) measurements at ambient temperature (WCA @RT in the graph legend) and the average values of WCA detected on the different coated samples in the temperature range between -2.5°C and-10°C (WCA @T < 0°C in the graph legend). The table produced as inset reports the percentage decrease of WCA between RT and T<0°C. Standard deviations are reported as errors bars.

In particular, when the temperature is decreasing LF surfaces suffer from a greater reduction of liquid repellency with respect to the SLIPS ones. In particular, LF suffered a decrease of WCA between ambient temperature and freezing environment of about 32%, with the loss of the superhydrophobic behavior. This can be ascribed to the previously cited Cassie-to-Wenzel transition (CWT), which leads to the penetration of the water drops inside the nanostructure, eliminating the air pockets needed to suspend the liquids with the consequent adhesion between the liquid and the surface. This phenomenon has been proved by non-restored initial values of WCA and

CAH when the samples returned at room temperature, which confirm the irreversible CWT just after a single exposure at temperature lower than 0°C.

Also, the dynamic anti-wetting ability of LF samples suffered a huge decrease, with an increase of the CAH from 7° to 35°, which led to a loss of mobility of the drops. The poor stability of LF coatings at low temperature makes them unsuitable for applications in cold environments. As far as SLIPS approach, the wetting behavior detected at subzero temperature resulted quite similar to that observed at room temperature.

The maximum drop in WCA observed in SLIPS samples was only by 6%. The application of Krytox™ GPL 105 as lubricant layer had an extremely positive effect on the anti-wetting performance below 0°C, keeping unchanged the WCA values before and after exposure in freezing environment.

Moreover, compared to LF samples all SLIPS exhibited much lower CAH at each subzero temperature, maintaining the values below 15°. This means that a proper dynamic anti-wetting ability was kept also in a supercooling environment.

The minimum decrease of CAH compared to LF samples has been measured for coatings with Al_2O_3 as inorganic layer and Krytox™ 105 oil as infused lubricant; furthermore, Krytox™ 105 gives the worst performance on both underlying silica and alumina layers due to its large viscosity (see Table 3) that hinders drop mobility [169].

Despite the satisfactory results in terms of wetting behavior at each tested temperature with both alumina and fluorinated silica as inorganic layer, Krytox™ 100 presented issues regarding the depletion of the oil during the course of the experiment.

This was probably due to the evaporation of Krytox™ 100 that even at room temperature has more tendency to leave uncovered the underlying structure. Hence, after the tests the samples lubricated with Krytox™ 100 lost their liquid repellency. SLIPS infused with Krytox™ GPL 103 and 105 did not exhibit this issue, due to the low evaporation rate of these oils [82]. The same wetting behavior is observed with both inorganic phases infused with lubricant oils, with no particular differences between samples coated with SiO_2 or Al_2O_3 NPs. Surfaces infused with silicone oil exhibited the same durability of samples infused with fluorinated lubricants, keeping WCA and CAH unchanged along time. All the coatings reported in Figure 44 have been selected as candidate coating to undergo through the durability test of Section 3.3, except for Al_2O_3Kr100 and SiO_2FKr100 coatings due to the aforementioned oil evaporation issues.

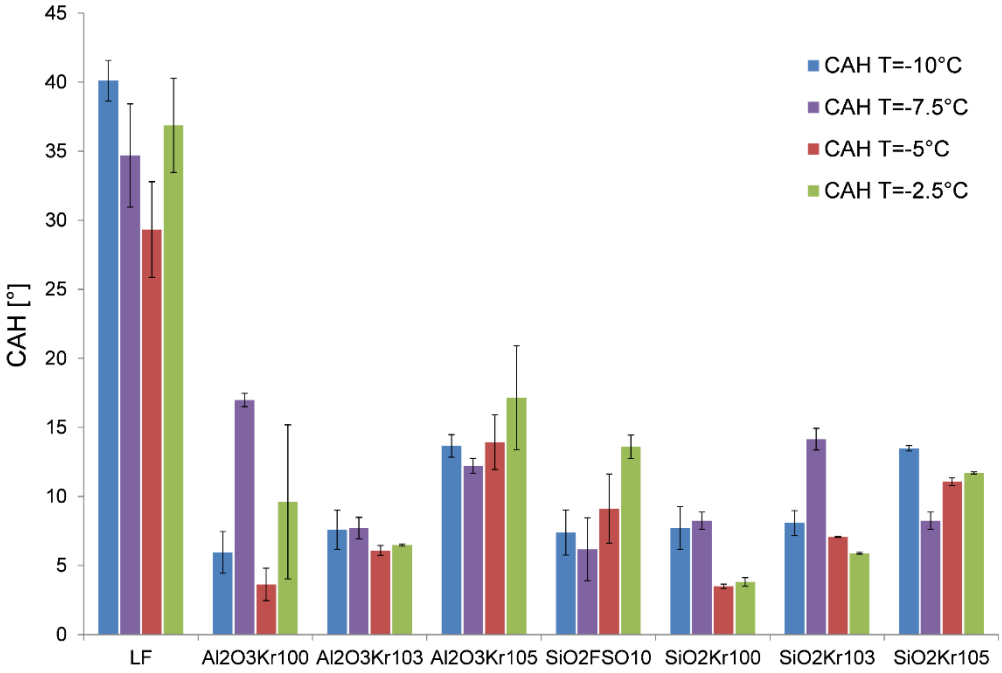

Figure 44. Contact angle hysteresis (CAH) of the surface coatings grouped by coating type. Standard deviations are reported as error bars.

3.4 Durability

The durability of coated surfaces is a key issue in view of practical applications, because it influences the end use of the designed materials or the environment to which they could be exposed. In particular we refer to durability as the ability to withstand degradation or wearing out in use. Very often the loss of performances over the time and/or under harsh conditions represent a very severe limitation for the technology transfer from the lab to the production scale. In addition, in many cases the understanding of the environmental conditions to be simulated is critical so that the choice of appropriate tests allowing to evaluate the retention of material performances over its lifecycle is not obvious.

We chose to analyze two different ice accretion conditions, namely freezing (e.g., solidification of liquid water) and frosting (condensation of humid air), and their effect on the wetting properties of the coatings.

3.4.1 Freeze/thaw test

The results of freeze/thaw tests are here discussed as a function of the different design approaches and coating composition.

In details, the sampling included the following surfaces:

- **LF (used as reference);**
- **Al_2O_3 Kr103 and Al_2O_3 Kr105;**
- **SiO_2F Kr103 and SiO_2F Kr105;**

- **SiO_2F SO10.**

CAH on the different sample surfaces was measured after one freeze/thaw cycle and compared with that of untreated samples (Figure 45). CAH value has been calculated as the average of 10 different measurements performed on the surface area in contact with water along the test.

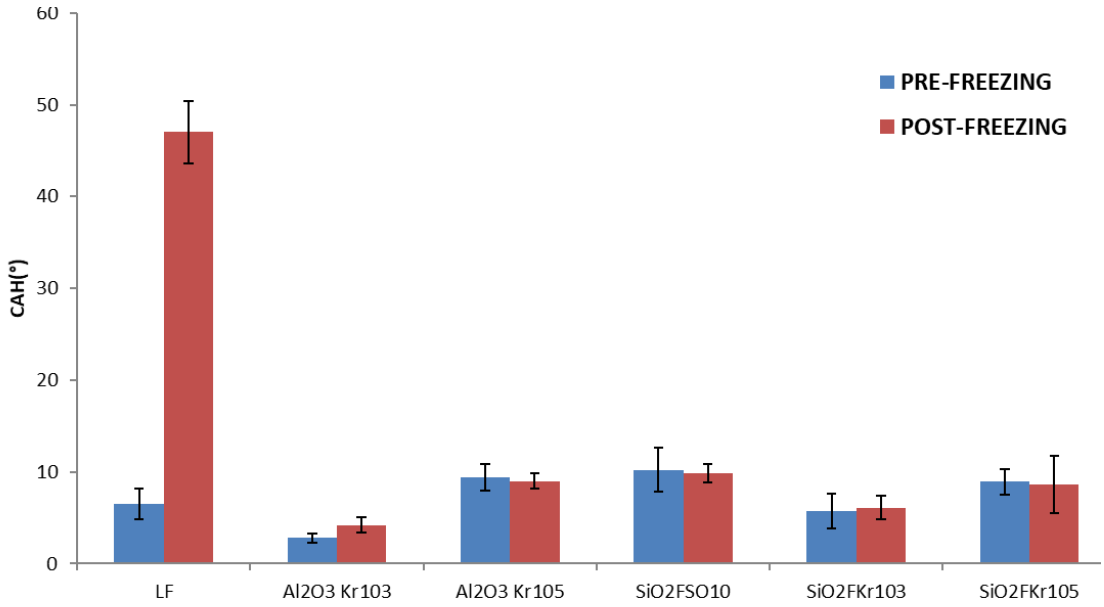

Figure 45. Average values of Contact Angle Hysteresis (CAH) for selected coated samples before (blue) and after a single freeze/thaw cycle (red). Standard deviations are reported as errors bars.

According to CAH results, LF samples lost their dynamic liquid repellency after performing a single freeze/thaw cycle, with a huge increase of CAH. As expected on the basis of the current literature[163,166], LF coatings revealed to be heavily affected by ice formation. SEM images of Figure 46 clearly show a significant flattening of the flower-like structures, which become unable to trap air between its features with the consequent Cassie-to-Wenzel transition

leading to a complete absence of drop mobility on the surface due to the increasing of liquid-solid adhesion forces. Specifically, Figure 46b shows a damaged area of the LF sample where only a small portion (light spots) of the nanostructured boehmite is still intact, while darker areas no longer possess the flower-like nanostructure.

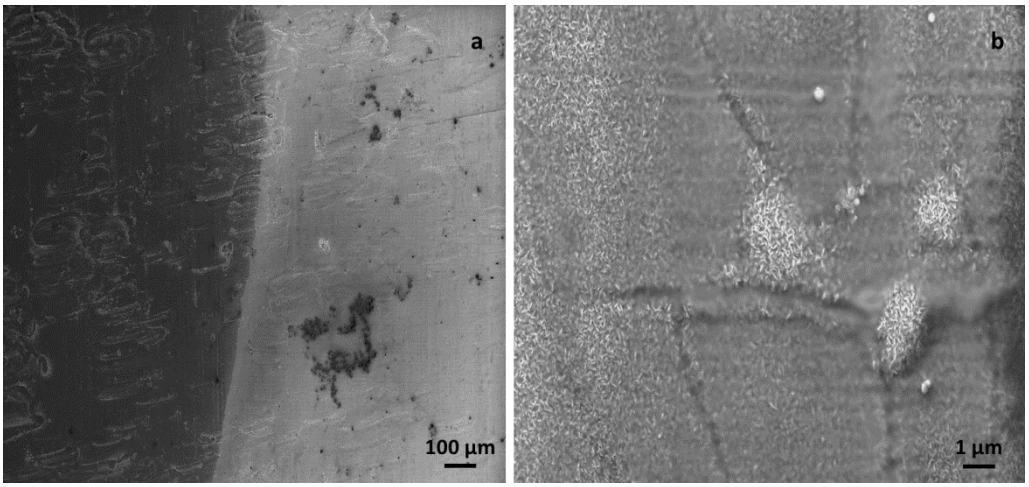

Figure 46. a) Micrographs of LF surfaces after freeze/thaw test; the dark zone was in contact with water during icing while the clear one was water-free during the test. b) High magnification of the frozen zone which exhibits the flattening of the flower-like structure after the test.

On the contrary, Al_2O_3 and SiO_2-based SLIPS preserved both static and dynamic anti-wetting performances after the first freeze/thaw cycle. SLIPS samples underwent 10 freeze/thaw cycles to evaluate the resistance of the surfaces. The values of CAH after each cycle are shown in Figure 47.

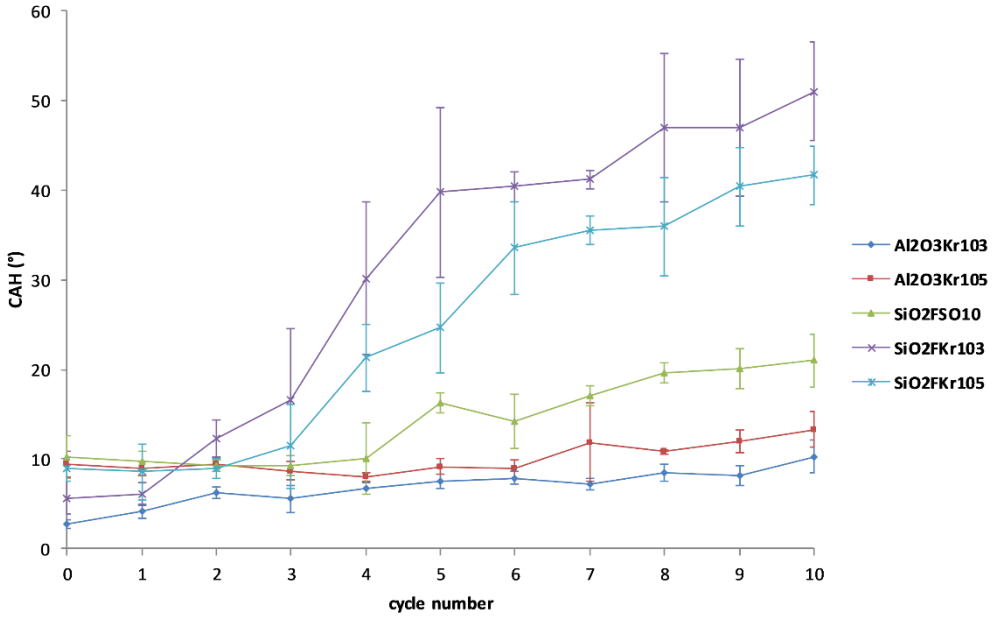

Figure 47. Contact angle hysteresis (CAH) as a function of the freeze/thaw cycle number. Standard deviations are reported as error bars.

Even if the surfaces have been interested in a clear depletion of the lubricant with respect to the initial state, the nanostructures remain partly infused as shown by Figure 48.

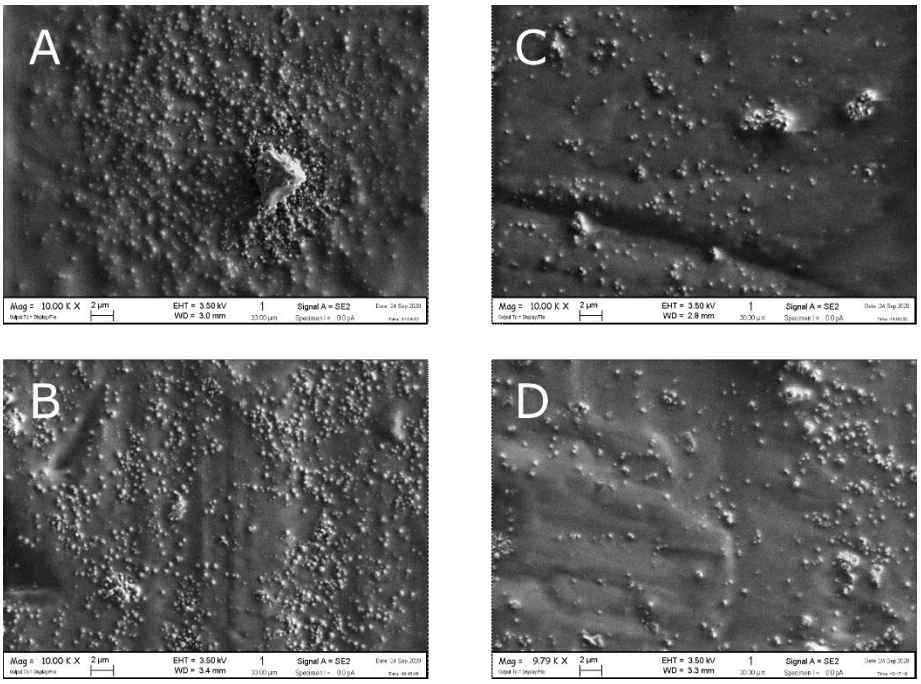

Figure 48. a) SEM micrograph of the freezing zone of SiO_2SO10 surface after freeze/thaw test; b) SEM micrograph of the freezing zone of SiO_2Kr105 surface after freeze/thaw test; c) and d) are reported as example of lubricant accumulation on the border zones for SiO_2SO10 and SiO_2Kr105 respectively.

Alumina-based SLIPS maintained their performance after 10 freeze/thaw cycles, with a slight increase of CAH which, however, never exceeded 15°. This means that after the test the drop mobility on Al_2O_3 SLIPS surfaces was preserved.

Using SiO_2 as inorganic layer and Krytox™ as lubricant, samples exhibit a remarkable increase of CAH after 3 freeze/thaw cycles, passing from about 10° to 20/30°. After the last cycle the CAH of SiO_2F SLIPS overcame 40°, with complete absence of drop mobility on the surface. The different behavior

could be due to the large pores in SiO_2F nanostructure (see Figure 31) which might cause a low capillary pressure and therefore a weak retention of the oil between the surface features. The formation of these holes is probably due to the formation of agglomerates of nanoparticles, unable to cover homogeneously the whole surface. The dimensions of the holes observed by SEM analysis might be a confirming evidence of this hypothesis. The Al_2O_3 "flower-like" nanostructure presents interstitial cavities with size close to 50 nm (see Figure 27), while the deposition of SiO_2F suspension leads to the formation of holes with size up to 1 μm (see Figure 30).

In the latter case, the cavities might be not narrow enough to guarantee the right anchorage of the lubricants and at the same time they allow water to penetrate within the surface structure.

At the scale of the surface nanostructures, the main responsible for the immobilization of the lubricant is the capillary force. In particular, over the top of the nanostructures, it is the capillary force that determines the nanoscale wettability, e.g., whether or not a continuous layer of lubricant is formed over the surface topography. The equilibrium film thickness is in fact the result of the balancing of the cohesive surface tension that draws the lubricant away and adhesive forces that stabilize the film. Through the cycles of the durability tests, the lubricant can be increasingly removed from the top of the nanostructures. If not "healed", the lubricant depletion will lead to the loss of hydrophobic behavior. Just in case of lubricant depletion from the top of the nanostructures, the lubricant that remains within the nanostructures might more or less easily restore the original film if it has

more or less tendency to spread "uphill". The more is this tendency, the more self-healing the SLIPS will be.

Samples coated with SiO_2F nanoparticles and infused with silicone oil (SiO_2FSO10) exhibited an increase of CAH after the 4^{th} freezing cycle, passing from 10° to about 16°. After the 4th cycle, the CAH remained quite constant in a range of around 16-20°, which means an acceptable mobility of the drops on the surfaces. The chemical affinity between silica and silicone oil provides a better adsorption compared to the Krytox™ fluoro-based lubricant. We presume that this effect promotes the silicone oil retention on the surface. The silicone layer is a barrier that prevents the water from getting in contact with the nanostructure below, in a way to preserve the hydrophobic property along the freezing cycles.

In the case of freeze/thaw process on SLIPS samples, water drops are free to move in every direction and they first nucleate on the free surface of the lubricant[1]. Since the drops are small, in the early stage one can neglect gravity. After some time, the drops grow in size. Due to gravity the drops begin to sink until their bottom come into contact with the substrate forming a three-phase, water/lubricant/substrate contact line. The creation of this solid contact line is the cause of the of the surface pinning. If pinned neighboring drops grow large enough that the lubricant menisci start overlapping a net attractive force between each other arises. Such phenomenon is similar to the lateral attraction between two particles which

are suspended on a free liquid surface [170]. The consequent coalescence drives lubricant transport to the lateral directions as shown by Figure 49.

During the freeze/thaw cycles the same lubricant transport to the lateral direction is extreme so as it is the lubricant drainage from the surface porosity because of the amount of pressure exerted by the water column, i.e. the drop.

As seen from the SEM micrograph a Figure 48, the transport phenomena during the freezing cycle leads to the accumulation of lubricant on the border of the freezing zone. We presume that the drainage of lubricant out the freezing area is the main responsible for the loss of anti-wetting properties.

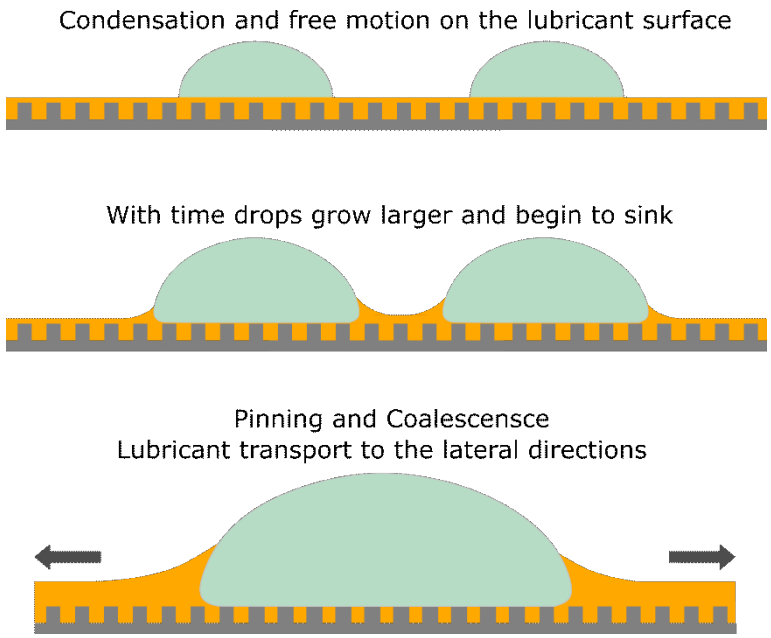

Figure 49. Scheme of the pinning and coalescence of water drops during the freezing process

Using a simple macroscopic model (the Dzyaloshinskii-Lifshitz-Pitaevskii or DLP model) we can calculate a rough estimate of the van der Waals interaction portion of the interface potential for Krytox™-infused SLIPS with both fluorinated silica and alumina as inorganic layer.

The original Dzyaloshinskii-Lifshit-Pitaevskii (DLP) theory [171] is a classical theory derived as a generalization of quantum field theory. Within this theory the atomic structure is ignored and the forces between large bodies - now treated as continuous media - are derived in terms of bulk properties as dielectric constants and refractive indices. In the planar "asymmetric configuration", i.e. two phases *a* and *c* interacting across medium *b* (e.g. the solid surface, the water drop and the infused lubricant in

Figure 49), the complete expression for the non-retarded Hamaker constant [172] based on the DLP theory is [173]:

$$A \approx \frac{3}{4} k_B T \frac{(\varepsilon_a - \varepsilon_c)(\varepsilon_b - \varepsilon_c)}{(\varepsilon_a + \varepsilon_c)(\varepsilon_b + \varepsilon_c)} + \frac{3h}{4\pi} \int_{\xi_1}^{\infty} \left[\frac{\varepsilon_a(i\xi) - \varepsilon_c(i\xi)}{\varepsilon_a(i\xi) + \varepsilon_c(i\xi)} \right] \left[\frac{\varepsilon_b(i\xi) - \varepsilon_c(i\xi)}{\varepsilon_b(i\xi) + \varepsilon_c(i\xi)} \right] d\xi$$

Where:

ε_i are the static dielectric constants with index $i = a, b, c$ (the three media);

$\varepsilon_i(i\xi)$ are the values of ε_i at imaginary frequencies with index $i = a, b, c$;

k_B is the Boltzmann Constant;

h is the Plank Constant.

The first term of the equation gives the zero-frequency energy of the van der Waals interaction and includes the Keesom and Debye contributions. The second term gives the dispersion energy and it includes the London energy contribution. The equation is not exact, because it is the first term in an infinite series, anyhow the other terms are small and they generally contribute no more than 5%.

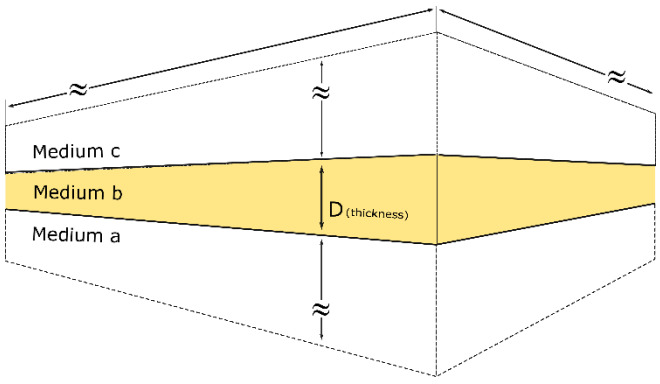

Figure 50. Schematization of the interaction between phases a and c across medium b

If we assume that i) the dispersion energy is largely determined by the electronic absorption only, and ii) the absorption frequencies of all three media are assumed to be the same, we obtain the following approximate expression for the non-retarded Hamaker constant for two macroscopic phases **a** and **c** interacting across a medium **b**:

$$\mathrm{A}_{abc} = \frac{3}{4} k_B T \left(\frac{\varepsilon_a - \varepsilon_b}{\varepsilon_a + \varepsilon_b} \right) \left(\frac{\varepsilon_c - \varepsilon_b}{\varepsilon_c + \varepsilon_b} \right) + \frac{3h\nu_e}{8\sqrt{2}} \cdot \frac{\left(n_a^2 - n_b^2 \right)\left(n_c^2 - n_b^2 \right)}{\sqrt{\left(n_a^2 + n_b^2 \right)\left(n_c^2 + n_b^2 \right)} \left[\sqrt{\left(n_a^2 + n_b^2 \right)} + \sqrt{\left(n_c^2 + n_b^2 \right)} \right]}$$

Where:

ν_e is the plasma frequency of free-electron gas;

n_a, n_b, n_c are the refractive index of material *a*, *b*, and *c*.

The interface potential on the non-retarded van der Waals (VdW) free energy interaction between two semi-infinite layers *a* and *c* acting across a medium *b*, as a function of layer separation *D* (see Figure 51), is:

$$E_{vdw} = -\frac{\mathrm{A}_{abc}}{12\pi} \cdot \frac{1}{D^2}$$

It is important to bear in mind that the DLP theory is a continuum theory, therefore it might only be safely used when the interacting surfaces are farther apart than the molecular dimensions of the surface structures. The systems we considered in our experiments are on the edge of the DLP's limit. The results obtained are indeed of qualitative nature only, because the nanostructures on the inorganic layers of the developed coating are on the

same scale as the thickness of the lubricant film covering the top region of the inorganic layers.

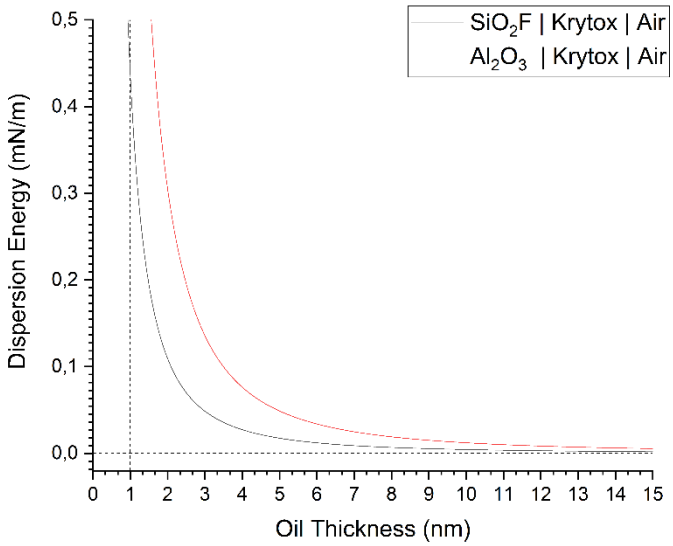

Figure 51. Dispersion energy term as a function of lubricant layer thickness with both Silica (blue) and Alumina (red) layers

The sign of the Hamaker constant indicates the nature of the interaction between flat layers. If the Hamaker constant is negative, then the VdW force is positive (repulsive), and the system results with a stable sandwiched layer of infused oil. Though the considered system is on the edge of the DLP's limit, the obtained repulsive forces for alumina SLIPS result to be of an order of magnitude larger than those one for the silica (see Figure 51).

The more repulsive the VdW forces are, the more wetting tendency of the infused oil there will be, and the underneath surface might easily recover the pristine oil-infused state. Even if rough, this model seems to describe why the silica SLIPSs show a less pronounced capillary action than the alumina SLIPSs., and the observed loss of performance of the silica SLIPSs after only a few freeze/thaw cycles might in part be due to such a phenomenon.

3.4.2 Frost/thaw test

The same samples used for freeze/thaw test underwent a frost/thaw test, also carried out in the freezer at -10°C±1°C but with no water put in contact with the surfaces. The frost/thaw durability test results are shown in Figure 52.

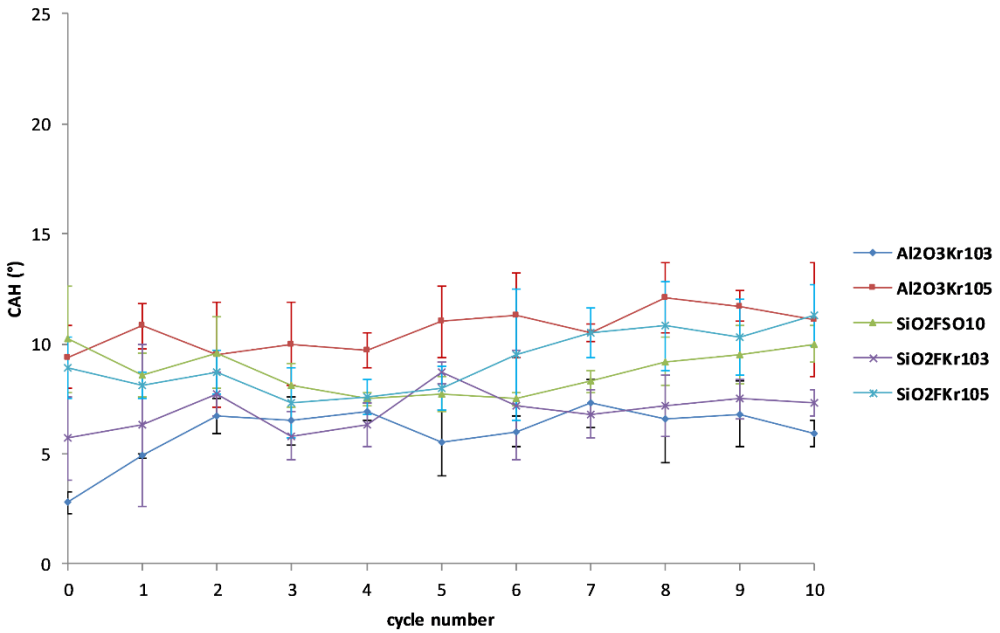

Figure 52. CAH as a function of the frost/thaw cycle number. Standard deviations are reported as error bars.

As for freeze/thaw test, LF samples presented a big increase of adhesion forces between water and surfaces just after a single frost/thaw cycle, with CAH passing from 6° to 66°. This is due to the replacement of the air pockets trapped in the nanostructure led by the condensation of environment water

at temperature below 0°C as discussed before. The same phenomenon has been observed during the CAH measurements at T < 0°C, in which the LF samples irreversibly lost their performance just after a single exposure in a freezing environment. Concerning SLIPS samples, all the surfaces maintained the CAH quite unchanged after 10 frost/thaw cycles, with CAH values oscillating between 5° and 10°. In this case the lubricant layer acts like an insulator which avoids the contact between the environmental water vapor and the nanostructure and consequent condensation.

Comparing the frosting results with the freezing ones, a remarkable effect of the freezing water in contact with the surfaces is noticed, especially when using SiO_2 as inorganic layer. The values of CAH for SiO_2 infused with fluorinated lubricant were retained throughout the entire frost/thaw tests, while during freeze/thaw tests the performance was lost after a few cycles. This different behavior, coupled with the presumed capillary effect discussed before, may be explained considering the penetration of water in the pores of the coatings. When putting liquid water in contact with the surface as in freeze/thaw tests, the lubricant layer has to support a much higher pressure with respect to the force applied with no liquid water in contact.

Probably the pressure applied during freezing was too high with the consequent lubricant film collapse, allowing the transport of lubricant out of the freezing zone, i.e. the area of contact between water and the surface. In addition, the penetration of the water inside the pores led to a further loss of anti-wetting performance because of the drainage of lubricant reservoir. Due

to the size of the pores, the flower-like structure offered by the Al_2O_3 inorganic coating results to be more suitable to support the pressure applied by the liquid water coupled with less drainage of lubricant oils and a consequent effective self-healing capacity. The design of Al_2O_3 SLIPS led to a complete stability of CAH values over both freezing and frosting cycles.

3.5 Icing Wind tunnel test

Concerning the aeronautic field, the repellence of supercooled drops is a key aspect for the safety of the aircraft. The limitation of the contact time between supercooled liquid drops and the surfaces is highly desired in order to decrease the ice accretion during the flight. Differently to the previous anti-icing test which were performed in static environment, the effect of the impact of drops at T lower than 0°C requested a dynamic evaluation leading to the utilization of an icing wind tunnel (IWT) to purchase this scope.

The samples subjected to IWT testing were characterized in term of weight of attached ice before and after the exposure on super cooled droplets, in conditions mimicking the glaze and rime icing regimes.

The results in term of ice weight and percentage of ice accretion for both regimes are shown in Table 10 and 11:

Table 10. Ice weight and percentage of ice accretion after IWT tests in glaze regime

Sample	Ice weight (g)	σ (g)	% of ice accretion	σ (%)
Reference	3.07	0.17	100.00	5.54
SiO_2F SO10	1.69	0.14	55.00	8.05
SiO_2F Kr103	1.89	0.05	61.63	2.42
SiO_2F Kr105	1.69	0.22	55.22	12.73
Al_2O_3 Kr103	1.98	0.21	64.46	10.40
Al_2O_3 Kr105	2.26	0.12	73.69	5.36

Table 11. Ice weight and percentage of ice accretion after IWT tests in rime regime

Sample	Ice weight (g)	σ (g)	% of ice accretion	σ (%)
Reference	1.45	0.10	100.00	6.87
SiO_2F SO10	1.30	0.12	89.58	9.53
SiO_2F Kr103	1.25	0.12	85.68	9.80
SiO_2F Kr105	1.20	0.27	82.47	22.38
Al_2O_3 Kr103	1.53	0.02	105.38	1.00
Al_2O_3 Kr105	1.54	0.19	105.84	12.17

LF samples were excluded from the IWT test due to the poor anti-icing abilities highlighted during the preliminary laboratory tests. The reported data are average values derived from measurements performed on three samples for each coating composition. Considering the bare NACA profile as reference, the effect of the anti-wetting coatings on ice accretion is remarkable, in particular for glaze ice test conditions. The next graphs exhibit the differences in term of ice accretion between the exposed samples in glaze (Figure 53) and rime (Figure 54) regimes:

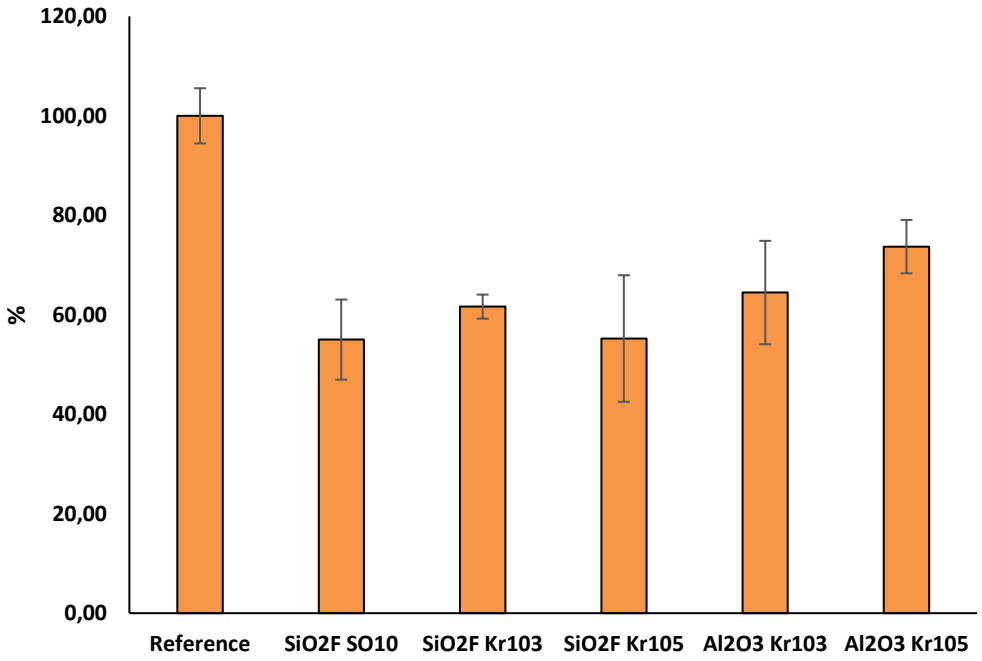

Figure 53. Percentage of ice accretion after IWT tests in glaze regime for uncoated reference and coated samples

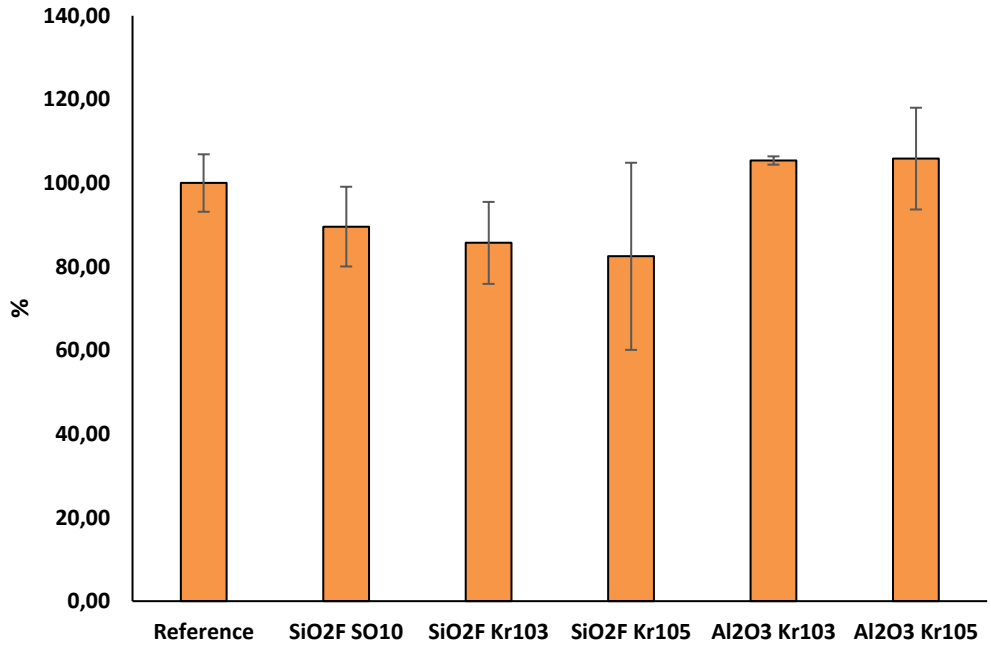

Figure 54. Percentage of ice accretion after IWT tests in rime regime for uncoated reference and coated samples

As shown in Figure 53 (glaze regime) all the coated samples presented a significant decrease of the percentage of ice accretion during the IWT test. The best result has been given by the samples covered with fluorinated silica nanoparticles and infused in silicon oil or Krytox™ GPL 105. The other samples present a higher amount of ice on them, nonetheless the weight of accreted ice was lower compared to the reference one. Passing from glaze to rime regime, the decrease of ice accretion become less significant. Only the surfaces coated with Silica NPs and Krytox™ GLP 105 resulted in a decrease of ice of about 20%. The other samples achieved no improvement with respect to the reference profiles. This fact could be explained considering the physical properties of the super cooled droplets in each regime. In glaze conditions the Liquid Water Content (LWC) is higher than in the rime ice regime, i.e. there is a higher amount of liquid water in the impacting particles. As previously demonstrated, SLIPS can effectively repel such liquid drops, limiting their adhesion and the consequent formation and growth of ice. In rime regime the LWC was lower (0.5 g/m^3 instead of 1 g/m^3); SLIPS are less effective in repeling the impacting particles, thus leading to a non-slippery interaction between the supercooled droplets and the surfaces.

This theory seems to be confirmed by the images captured during the IWT tests.

Figure 55 shown different moments of the IWT test in glaze ice conditions for SiO_2FSO10 sample:

Figure 55. Icing wind tunnel test of SiO_2FSO10 sample in glaze ice conditions.

From t=0 and 11s the supercooled drops presented a good mobility on the surface. After 11s the glaze ice began to nucleate on the sample, but the poor adhesion led to the formation of a fractured ice layer as shown by the Figure 56:

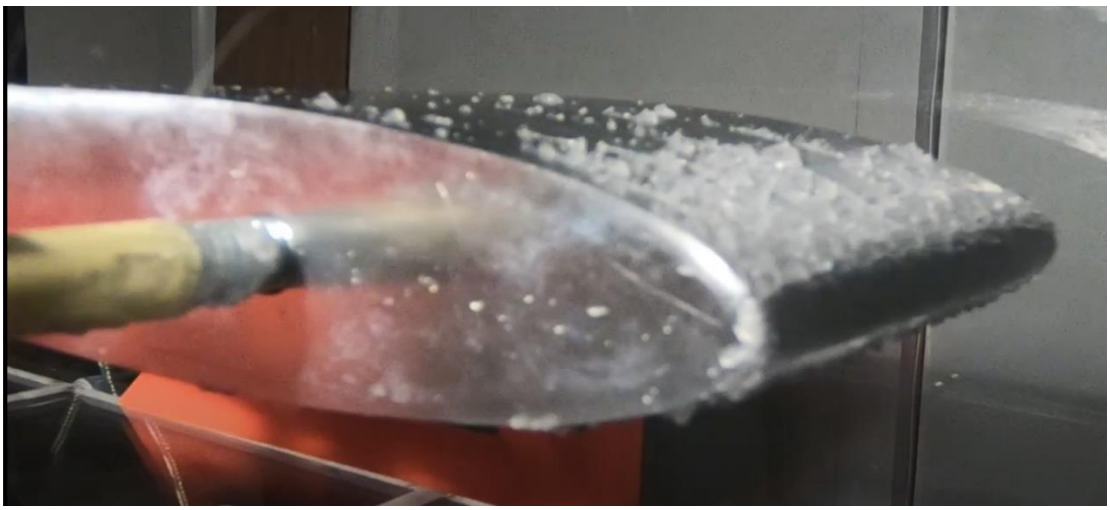

Figure 56. SiO_2FSO10 sample after icing wing tunnel test in glaze ice conditions.

In rime ice conditions the slippery behavior of the functionalized samples is not observed, with the complete ice layer formation in the first seconds of the test as highlighted by Figure 57:

Figure 57. Icing wind tunnel test of SiO_2FSO10 sample in glaze ice conditions.

The formation of ice layer began just after 3 seconds in the test, localized on the sample area more exposed to the flux (i.e. the leading edge), due to the poor mobility of the supercooled droplets and the quickness of the nucleation of the ice. At the end of the test the rime ice layer is completely formed with a typical opaque resemblance as shown by Figure 58:

Figure 58. SiO_2FSO10 sample after icing wing tunnel test in rime ice conditions.

The same behavior is noticed for all coated samples, with no particular visible differences between Alumina and Silica SLIPS or surfaces infused with different lubricants.

In rime conditions, the limited droplet mobility on the surfaces leads to an ice accretion similar to the uncoated NACA profile, in particular for samples deposited with Alumina as inorganic layer.

The results confirm the better efficiency of the designed non-wetting surfaces in glaze ice environment with respect to the rime ice one, mainly due to the LWC of the super cooled particles which collide with the sample. The anti-wetting coatings produced during this project, due to their ability on decrease ice accumulation in glaze ice regime, could find application in the aeronautic field because the aircrafts interface glaze ice environment during the major part of the flight (i.e. take off and landing).

3.6 Ice adhesion test

SLIPS were also analyzed in terms of ice adhesion. The ice adhesion data measured on uncoated reference samples, AA6061-T6 aeronautic aluminum alloy (a common aeronautic material), both bare and PTFE coated and SLIPS surfaces are shown in Table 11. As for IWT test, LF samples were excluded from ice adhesion test analysis due to the poor anti-icing abilities highlighted during the analysis of ice nucleation delay and wetting behavior at temperature lower than 0°C.

Table 12. Ice adhesion force of references and coated surfaces

Sample	Ice Adhesion Force (KPa)	σ (KPa)
Reference	403	61.5
AA6061-T6	374	12.5
PTFE	76	6
SiO_2F SO10	58	4.5
SiO_2F Kr103	35	4
SiO_2F Kr105	82	24
Al_2O_3 Kr103	23	3
Al_2O_3 Kr105	23	1.5

All SLIPS showed much lower ice adhesion force compared to the uncoated samples and the AA6160-T6 Aluminum alloy surface. Moreover, SLIPS

samples had a better anti-icing behavior than surfaces coated with PTFE especially when Alumina was used as inorganic layer.

The differences between reference and coated samples are shown in Figure 59:

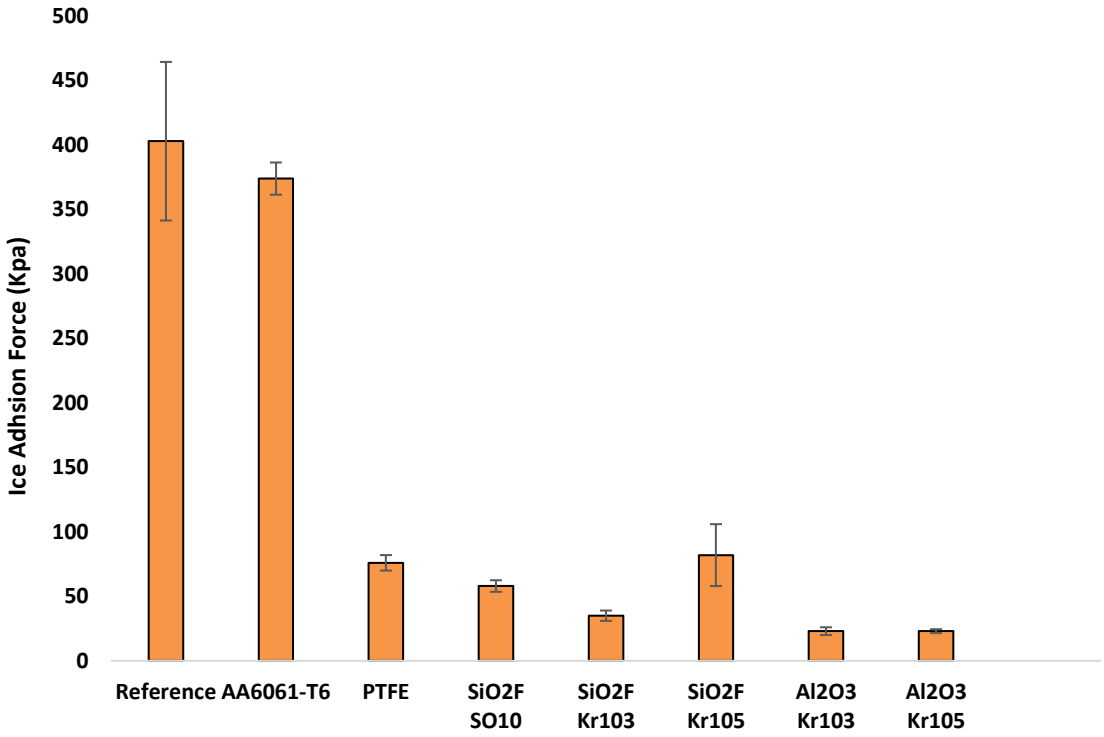

Figure 59. Ice adhesion force measured for reference and coated samples. Standard deviations are reported as error bars.

The graph highlights the huge difference between coated and uncoated samples. Alumina SLIPS reduced the ice adhesion force of around 95% if compared to the uncoated surface and 94% compared to AA6061-T6. Using

Silica as inorganic layer, the values showed a little increase but still displayed excellent de-icing, having the ice adhesion force lower than 100KPa.

All SLIPS samples, excluding SiO_2 Kr105, present a significant adhesion force reduction also compared to PTFE coated surfaces.

SiO_2 Kr105 exhibited hindrances in terms of reproducibility showed by the high standard deviation in the measurements. This is probably due to the inhomogeneity of the substrate. The presence of some kind of scratch on the bare material can provoke the depletion of the lubricant with the consequent creation of sites favorable for the ice attachment and increase of adhesion force.

Considering that PTFE is adopted in the last years as typical passive de-icing method, SLIPS samples overcome their ice adhesion and they could become good candidate to be applied as anti-icing layers in many industrial fields which need surfaces able to easily detach ice from them, especially in aeronautics.

Conclusions

The present thesis was aimed at the design and development of biomimetic coatings with a potential for the mitigation of icing issues. The process started with the synthesis of different suspensions of ceramic oxide nanoparticles via sol-gel route. We first designed a hybrid inorganic-organic coating based on nanostructured alumina and a grafted fluorinated organic polymer, and a facile coating based on fluorinated SiO_2 nanoparticles deposited by a single step process. We also explored a different approach to liquid repellency, as per the so-called SLIPS approach. We added low surface tension lubricants - different types of fluorinated Krytox™ GPL and a silicone oil - with different viscosities and chemical compositions to explore their different behavior when infused in the hybrid-coated surfaces.

The designed samples presented outstanding anti-wetting abilities in both static and dynamic conditions, with WCA close to 170° (especially for LF samples) and CAH lower than 15°.

Subsequently, we investigated the potential of these low-wettable surfaces for application in cold environments, thus we tested them in a wide variety of experimental setups and conditions. We first studied the static and dynamic wetting behavior on the fabricated low-wettable coatings at subzero temperatures. In particular we report evidence of stable static water contact angle and low water contact angle hysteresis of all SLIPS coatings in the temperature range from -10°C to 0°C. Quite remarkably, high drop mobility was also achieved at temperature below 0°C. Comparing the

performance of different coatings, it was noticed that SLIPS infused in Krytox™ GPL 103 oil provided the best wetting properties at subzero temperature. Differently from SLIPS, LF samples presented a huge decrease in their anti-wetting properties just after a single exposure to freezing environment. This loss of performance is probably due to the replacement of the air pockets trapped in the hierarchical structure by condensed water.

Moreover, the designed samples were characterized in term of ice nucleation delay at temperature of -5°C. The anti-wetting coatings had been proven as nucleation delayer, exploiting their capacity to increase the energy barrier to start the freezing process. Despite that, the results exhibited a poor reproducibility, probably due to the instauration of a quasi-equilibrium state of the supercooled water, which can remain liquid until -40°C, in absence of an external perturbation. For these reasons this test was quit after the first year and half of the Ph.D. project.

On the other hand, coated samples exhibited an outstanding decrease of ice adhesion with respect to common aeronautic materials, both uncoated and PTFE coated. The ice adhesion forces lower than 100KPa make SLIPS samples a suitable anti-icing passive system where the facile detachment of ice is crucial for the real application, as in aircraft.

To replicate the dynamic environment which aircraft features undergo during a flight, Icing Wing Tunnel tests were performed. All the fabricated SLIPS exhibited a decrease in ice accretion during exposure in glaze ice regime environment if compared with the uncoated profiles. These

differences were not observed when the materials interfaced supercooled drops in rime ice regime, showing ice accumulation results comparable with those of the bare substrate.

Finally, the durability of fabricated low-wettable surfaces was also investigated by monitoring the evolution of their wetting properties after ice accretion in two different conditions (i.e. freezing and frosting). All the investigated surfaces showed a good resistance along frosting test, with the only exception of LF samples. After 10 frost/thaw cycles, the CAH values resulted unchanged using both SiO_2 and Al_2O_3 nanoparticles as inorganic layers.

Concerning freezing test, only Al_2O_3-based SLIPS kept the CAH values stable along cycles while SiO_2F SLIPS infused with Krytox™ oils lost their performance after few exposures in the icing environment. SiO_2F SLIPS infused in silicone oil suffered a slight increase of CAH after the third cycle but then the values remained stable until the last exposure.

These results highlight the potential of SLIPS in those application fields in which dynamic water repellency at subzero temperature is crucial (e.g., aeronautics, telecommunications, etc.). Moreover, it is important to carefully consider the icing environments that low-wettable surfaces will face once in operation. The results of the different tests showed that different coating formulations can display the best properties depending on the environmental conditions. SLIPS design and engineering must account for possible oil depletion phenomena in order to achieve durable water

repellency when exposed at subzero temperature. In perspective of future large-scale application of the presented solutions, it must be said that SLIPS formulations have a higher cost than LF ones due to the addition of the lubricant; moreover, fluorinated lubricants like Krytox™ have a significantly higher price than fluorine-free liquids like silicone oil. However, their excellent repellence and enhanced durability at subzero temperatures can justify such cost difference, especially for high-added value applications, i.e. aircraft surfaces.

References

1. Wenzel, R.N. Resistance of solid surfaces to wetting by water. *Ind. Eng. Chem.* **1936**, *28*, 988–994, doi:10.1021/ie50320a024.
2. Cassie, B.D. Of porous surfaces. *Physics (College. Park. Md).* **1944**, *40*, 546–551.
3. Barthlott, W.; Ehler, N. Raster-Elektronenmikroskopie der Epidermis-Oberflachen von Spermatophyten. *Trop. Subtrop. Pflanzenwelt* **1977**.
4. Barthlott, W.; Neinhuis, C. Purity of the sacred lotus, or escape from contamination in biological surfaces. *Planta* **1997**, *202*, 1–8, doi:10.1007/s004250050096.
5. Celia, E.; Darmanin, T.; Taffin de Givenchy, E.; Amigoni, S.; Guittard, F. Recent advances in designing superhydrophobic surfaces. *J. Colloid Interface Sci.* 2013.
6. Herbertson, D.L.; Evans, C.R.; Shirtcliffe, N.J.; McHale, G.; Newton, M.I. Electrowetting on superhydrophobic SU-8 patterned surfaces. *Sensors Actuators, A Phys.* **2006**, doi:10.1016/j.sna.2005.12.018.
7. Chou, S.Y.; Keimel, C.; Gu, J. Ultrafast and direct imprint of nanostructures in silicon. *Nature* **2002**, doi:10.1038/nature00792.
8. Bhushan, B.; Koch, K.; Jung, Y.C. Fabrication and characterization of the hierarchical structure for superhydrophobicity and self-cleaning. *Ultramicroscopy* **2009**, doi:10.1016/j.ultramic.2009.03.030.
9. Zhong, W.; Li, Y.; Wang, Y.; Chen, X.; Wang, Y.; Yang, W. Superhydrophobic polyaniline hollow bars: Constructed with

nanorod-arrays based on self-removing metal-monomeric template. *J. Colloid Interface Sci.* **2012**, doi:10.1016/j.jcis.2011.08.083.

10. Vandencasteele, N.; Merche, D.; Reniers, F. XPS and contact angle study of N2 and O2 plasma-modified PTFE, PVDF and PVF surfaces. In Proceedings of the Surface and Interface Analysis; 2006.
11. Wohlfart, E.; Fernández-Blázquez, J.P.; Arzt, E.; Del Campo, A. Nanofibrillar patterns on PET: The influence of plasma parameters in surface morphology. *Plasma Process. Polym.* **2011**, doi:10.1002/ppap.201000164.
12. Qian, B.; Shen, Z. Fabrication of superhydrophobic surfaces by dislocation-selective chemical etching on aluminum, copper, and zinc substrates. *Langmuir* **2005**, doi:10.1021/la051308c.
13. Bernagozzi, I.; Antonini, C.; Villa, F.; Marengo, M. Fabricating superhydrophobic aluminum: An optimized one-step wet synthesis using fluoroalkyl silane. *Colloids Surfaces A Physicochem. Eng. Asp.* **2014**, doi:10.1016/j.colsurfa.2013.05.042.
14. Choi, H.J.; Shin, J.H.; Choo, S.; Ryu, S.W.; Kim, Y.D.; Lee, H. Fabrication of superhydrophobic and oleophobic Al surfaces by chemical etching and surface fluorination. *Thin Solid Films* **2015**, doi:10.1016/j.tsf.2015.03.046.
15. Feng, L.; Zhang, H.; Mao, P.; Wang, Y.; Ge, Y. Superhydrophobic alumina surface based on stearic acid modification. *Appl. Surf. Sci.* **2011**, *257*, 3959–3963, doi:10.1016/j.apsusc.2010.11.143.
16. Fan, Y.; Li, C.; Chen, Z.; Chen, H. Study on fabrication of the

superhydrophobic sol-gel films based on copper wafer and its anti-corrosive properties. *Appl. Surf. Sci.* **2012**, doi:10.1016/j.apsusc.2012.03.072.

17. Cengiz, U.; Avci, M.Z.; Erbil, H.Y.; Sarac, A.S. Superhydrophobic terpolymer nanofibers containing perfluoroethyl alkyl methacrylate by electrospinning. *Appl. Surf. Sci.* **2012**, doi:10.1016/j.apsusc.2012.02.107.
18. Ma, W.; Wu, H.; Higaki, Y.; Otsuka, H.; Takahara, A. A "non-sticky" superhydrophobic surface prepared by self-assembly of fluoroalkyl phosphonic acid on a hierarchically micro/nanostructured alumina gel film. *Chem. Commun. (Camb).* **2012**, *48*, 6824–6, doi:10.1039/c2cc32513f.
19. Gao, L.; He, J. Surface hydrophobic co-modification of hollow silica nanoparticles toward large-area transparent superhydrophobic coatings. *J. Colloid Interface Sci.* **2013**, *396*, 152–159, doi:10.1016/j.jcis.2013.01.014.
20. Li, Y.; Li, L.; Sun, J. Bioinspired self-healing superhydrophobic coatings. *Angew. Chemie - Int. Ed.* **2010**, *49*, 6129–6133, doi:10.1002/anie.201001258.
21. Li, Y.; Chen, S.; Wu, M.; Sun, J. All spraying processes for the fabrication of robust, self-healing, superhydrophobic coatings. *Adv. Mater.* **2014**, *26*, 3344–3348, doi:10.1002/adma.201306136.
22. Song, M.; Liu, Y.; Cui, S.; Liu, L.; Yang, M. Fabrication and icing property of superhydrophilic and superhydrophobic aluminum

surfaces derived from anodizing aluminum foil in a sodium chloride aqueous solution. *Appl. Surf. Sci.* **2013**, doi:10.1016/j.apsusc.2013.05.088.

23. Darmanin, T.; De Givenchy, E.T.; Amigoni, S.; Guittard, F. Superhydrophobic surfaces by electrochemical processes. *Adv. Mater.* **2013**, *25*, 1378–1394, doi:10.1002/adma.201204300.
24. Wang, Z.; Zhu, L.; Li, W.; Liu, H. Bioinspired in situ growth of conversion films with underwater superoleophobicity and excellent self-cleaning performance. *ACS Appl. Mater. Interfaces* **2013**, *5*, 10904–10911, doi:10.1021/am4030966.
25. Yao, L.; Zheng, M.; He, S.; Ma, L.; Li, M.; Shen, W. Preparation and properties of ZnS superhydrophobic surface with hierarchical structure. *Appl. Surf. Sci.* **2011**, *257*, 2955–2959, doi:10.1016/j.apsusc.2010.10.098.
26. Ishizaki, T.; Hieda, J.; Saito, N.; Saito, N.; Takai, O. Corrosion resistance and chemical stability of super-hydrophobic film deposited on magnesium alloy AZ31 by microwave plasma-enhanced chemical vapor deposition. *Electrochim. Acta* **2010**, *55*, 7094–7101, doi:10.1016/j.electacta.2010.06.064.
27. Pareo, P.; De Gregorio, G.L.; Manca, M.; Pianesi, M.S.; De Marco, L.; Cavallaro, F.; Mari, M.; Pappadà, S.; Ciccarella, G.; Gigli, G. Ultra lightweight PMMA-based composite plates with robust super-hydrophobic surfaces. *J. Colloid Interface Sci.* **2011**, *363*, 668–675, doi:10.1016/j.jcis.2011.07.075.

28. Psarski, M.; Marczak, J.; Grobelny, J.; Celichowski, G. Superhydrophobic surface by replication of laser micromachined pattern in epoxy/alumina nanoparticle composite. *J. Nanomater.* **2014**, *2014*, doi:10.1155/2014/547895.
29. Milionis, A.; Languasco, J.; Loth, E.; Bayer, I.S. Analysis of wear abrasion resistance of superhydrophobic acrylonitrile butadiene styrene rubber (ABS) nanocomposites. *Chem. Eng. J.* **2015**, *281*, 730–738, doi:10.1016/j.cej.2015.06.086.
30. Feng, L.; Zhang, H.; Wang, Z.; Liu, Y. Superhydrophobic aluminum alloy surface: Fabrication, structure, and corrosion resistance. *Colloids Surfaces A Physicochem. Eng. Asp.* **2014**, doi:10.1016/j.colsurfa.2013.09.014.
31. Ou, J.; Hu, W.; Liu, S.; Xue, M.; Wang, F.; Li, W. Superoleophobic textured copper surfaces fabricated by chemical etching/oxidation and surface fluorination. *ACS Appl. Mater. Interfaces* **2013**, doi:10.1021/am402531m.
32. Van Ooij, W.J.; Zhu, D.Q.; Prasad, G.; Jayaseelan, S.; Fu, Y.; Teredesai, N. Silane based chromate replacements for corrosion control, paint adhesion, and rubber bonding. *Surf. Eng.* **2000**, doi:10.1179/026708400101517369.
33. Zhang, X.; Shi, F.; Niu, J.; Jiang, Y.; Wang, Z. Superhydrophobic surfaces: From structural control to functional application. *J. Mater. Chem.* **2008**, doi:10.1039/b711226b.
34. Manca, M.; Cannavale, A.; De Marco, L.; Aricò, A.S.; Cingolani, R.;

Gigli, G. Durable superhydrophobic and antireflective surfaces by trimethylsilanized silica nanoparticles-based sol-gel processing. *Langmuir* **2009**, *25*, 6357–6362, doi:10.1021/la804166t.

35. Xu, L.; He, J. Fabrication of highly transparent superhydrophobic coatings from hollow silica nanoparticles. *Langmuir* **2012**, doi:10.1021/la301420p.
36. Papadopoulos, P.; Mammen, L.; Deng, X.; Vollmer, D.; Butt, H.J. How superhydrophobicity breaks down. *Proc. Natl. Acad. Sci. U. S. A.* **2013**, *110*, 3254–3258, doi:10.1073/pnas.1218673110.
37. Bormashenko, E.; Pogreb, R.; Whyman, G.; Erlich, M. Cassie-Wenzel wetting transition in vibrating drops deposited on rough surfaces: Is the dynamic Cassie-Wenzel wetting transition a 2D or 1D affair? *Langmuir* **2007**, *23*, 6501–6503, doi:10.1021/la700935x.
38. Lafuma, A.; Quéré, D. Superhydrophobic states. *Nat. Mater.* **2003**, *2*, 457–460, doi:10.1038/nmat924.
39. Bartolo, D.; Bouamrirene, F.; Verneuil, É.; Buguin, A.; Silberzan, P.; Moulinet, S. Bouncing or sticky droplets: Impalement transitions on superhydrophobic micropatterned surfaces. *Europhys. Lett.* **2006**, *74*, 299–305, doi:10.1209/epl/i2005-10522-3.
40. Wong, T.S.; Kang, S.H.; Tang, S.K.Y.; Smythe, E.J.; Hatton, B.D.; Grinthal, A.; Aizenberg, J. Bioinspired self-repairing slippery surfaces with pressure-stable omniphobicity. *Nature* **2011**, *477*, 443–447, doi:10.1038/nature10447.
41. Bohn, H.F.; Federle, W. Insect aquaplaning: Nepenthes pitcher plants

capture prey with the peristome, a fully wettable water-lubricated anisotropic surface. *Proc. Natl. Acad. Sci. U. S. A.* **2004**, doi:10.1073/pnas.0405885101.

42. Laforte, J.L.; Allaire, M.A.; Laflamme, J. State-of-the-art on power line de-icing. *Atmos. Res.* **1998**, *46*, 143–158, doi:10.1016/S0169-8095(97)00057-4.
43. Farzaneh, M.; Volat, C.; Leblond, A. Anti-icing and de-icing techniques for overhead lines. In *Atmospheric Icing of Power Networks*; 2008; pp. 229–268 ISBN 9781402085307.
44. Egbert, R.I.; Schrag, R.L.; Bernhart, W.D.; Zumwalt, G.W.; Kendrew, T.J. An investigation of power une de-icing by electro-impulse methods. *IEEE Trans. Power Deliv.* **1989**, *4*, 1855–1861, doi:10.1109/61.32682.
45. Gent, R.W.; Dart, N.P.; Cansdale, J.T. Aircraft icing. *Philos. Trans. R. Soc. A Math. Phys. Eng. Sci.* **2000**, *358*, 2873–2911, doi:10.1098/rsta.2000.0689.
46. Schutzius, T.M.; Jung, S.; Maitra, T.; Eberle, P.; Antonini, C.; Stamatopoulos, C.; Poulikakos, D. Physics of icing and rational design of surfaces with extraordinary icephobicity. *Langmuir* **2015**, *31*, 4807–4821, doi:10.1021/la502586a.
47. Whale, T.F.; Rosillo-Lopez, M.; Murray, B.J.; Salzmann, C.G. Ice Nucleation Properties of Oxidized Carbon Nanomaterials. *J. Phys. Chem. Lett.* **2015**, doi:10.1021/acs.jpclett.5b01096.
48. Moore, E.B.; Molinero, V. Structural transformation in supercooled

water controls the crystallization rate of ice. *Nature* **2011**, doi:10.1038/nature10586.

49. Maitra, T.; Antonini, C.; Tiwari, M.K.; Mularczyk, A.; Imeri, Z.; Schoch, P.; Poulikakos, D. Supercooled water drops impacting superhydrophobic textures. *Langmuir* **2014**, *30*, 10855–10861, doi:10.1021/la502675a.
50. Eberle, P.; Tiwari, M.K.; Maitra, T.; Poulikakos, D. Rational nanostructuring of surfaces for extraordinary icephobicity. *Nanoscale* **2014**, *6*, 4874–4881, doi:10.1039/c3nr06644d.
51. Li, Q.; Guo, Z. Fundamentals of icing and common strategies for designing biomimetic anti-icing surfaces. *J. Mater. Chem. A* **2018**, *6*, 13549–13581, doi:10.1039/c8ta03259a.
52. Bi, Y.; Cao, B.; Li, T. Enhanced heterogeneous ice nucleation by special surface geometry. *Nat. Commun.* **2017**, doi:10.1038/ncomms15372.
53. Jung, S.; Tiwari, M.K.; Doan, N.V.; Poulikakos, D. Mechanism of supercooled droplet freezing on surfaces. *Nat. Commun.* **2012**, doi:10.1038/ncomms1630.
54. Hartmann, S.; Niedermeier, D.; Voigtländer, J.; Clauss, T.; Shaw, R.A.; Wex, H.; Kiselev, A.; Stratmann, F. Homogeneous and heterogeneous ice nucleation at LACIS: Operating principle and theoretical studies. *Atmos. Chem. Phys.* **2011**, doi:10.5194/acp-11-1753-2011.
55. Hoose, C.; Möhler, O. Heterogeneous ice nucleation on atmospheric aerosols: A review of results from laboratory experiments. *Atmos.*

Chem. Phys. 2012.

56. Michaelides, A.; Morgenstern, K. Ice nanoclusters at hydrophobic metal surfaces. *Nat. Mater.* **2007**, doi:10.1038/nmat1940.
57. Koehler, K.A.; Demott, P.J.; Kreidenweis, S.M.; Popovicheva, O.B.; Petters, M.D.; Carrico, C.M.; Kireeva, E.D.; Khokhlova, T.D.; Shonija, N.K. Cloud condensation nuclei and ice nucleation activity of hydrophobic and hydrophilic soot particles. *Phys. Chem. Chem. Phys.* **2009**, doi:10.1039/b905334b.
58. Alizadeh, A.; Yamada, M.; Li, R.; Shang, W.; Otta, S.; Zhong, S.; Ge, L.; Dhinojwala, A.; Conway, K.R.; Bahadur, V.; et al. Dynamics of ice nucleation on water repellent surfaces. *Langmuir* **2012**, *28*, 3180–3186, doi:10.1021/la2045256.
59. Momen, G.; Jafari, R.; Farzaneh, M. Ice repellency behaviour of superhydrophobic surfaces: Effects of atmospheric icing conditions and surface roughness. *Appl. Surf. Sci.* **2015**, doi:10.1016/j.apsusc.2015.04.180.
60. Tishkova, V.; Demirdjian, B.; Ferry, D.; Johnson, M. Neutron diffraction study of water freezing on aircraft engine combustor soot. *Phys. Chem. Chem. Phys.* **2011**, doi:10.1039/c1cp21109a.
61. Xu, W.; Lan, Z.; Peng, B.; Wen, R.; Ma, X. Evolution of transient cluster/droplet size distribution in a heterogeneous nucleation process. *RSC Adv.* **2014**, doi:10.1039/c4ra03074e.
62. Boreyko, J.B.; Collier, C.P. Delayed frost growth on jumping-drop superhydrophobic surfaces. *ACS Nano* **2013**, doi:10.1021/nn3055048.

63. Nosonovsky, M.; Hejazi, V. Why superhydrophobic surfaces are not always icephobic. *ACS Nano* 2012.
64. Farhadi, S.; Farzaneh, M.; Kulinich, S.A. Anti-icing performance of superhydrophobic surfaces. *Appl. Surf. Sci.* **2011**, *257*, 6264–6269, doi:10.1016/j.apsusc.2011.02.057.
65. Chen, J.; Li, K.; Wu, S.; Liu, J.; Liu, K.; Fan, Q. Durable Anti-Icing Coatings Based on Self-Sustainable Lubricating Layer. *ACS Omega* **2017**, *2*, 2047–2054, doi:10.1021/acsomega.7b00359.
66. Stamatopoulos, C.; Hemrle, J.; Wang, D.; Poulikakos, D. Exceptional Anti-Icing Performance of Self-Impregnating Slippery Surfaces. *ACS Appl. Mater. Interfaces* **2017**, *9*, 10233–10242, doi:10.1021/acsami.7b00186.
67. Rykaczewski, K.; Anand, S.; Subramanyam, S.B.; Varanasi, K.K. Mechanism of frost formation on lubricant-impregnated surfaces. *Langmuir* **2013**, *29*, 5230–5238, doi:10.1021/la400801s.
68. Subramanyam, S.B.; Rykaczewski, K.; Varanasi, K.K. Ice adhesion on lubricant-impregnated textured surfaces. *Langmuir* **2013**, doi:10.1021/la402456c.
69. Yeong, Y.H.; Wang, C.; Wynne, K.J.; Gupta, M.C. Oil-infused superhydrophobic silicone material for low ice adhesion with long-term infusion stability. *ACS Appl. Mater. Interfaces* **2016**, *8*, 32050–32059, doi:10.1021/acsami.6b11184.
70. Wilson, P.W.; Lu, W.; Xu, H.; Kim, P.; Kreder, M.J.; Alvarenga, J.; Aizenberg, J. Inhibition of ice nucleation by slippery liquid-infused

porous surfaces (SLIPS). *Phys. Chem. Chem. Phys.* **2013**, doi:10.1039/c2cp43586a.

71. Parent, O.; Ilinca, A. Anti-icing and de-icing techniques for wind turbines: Critical review. *Cold Reg. Sci. Technol.* **2011**, doi:10.1016/j.coldregions.2010.01.005.
72. Na, B.; Webb, R.L. A fundamental understanding of factors affecting frost nucleation. *Int. J. Heat Mass Transf.* **2003**, doi:10.1016/S0017-9310(03)00194-7.
73. Chang, Y.S. Performance analysis of frostless heat exchanger by spreading antifreeze solution on heat exchanger surface. *J. Therm. Sci. Technol.* **2011**, doi:10.1299/jtst.6.123.
74. Makkonen, L. Models for the growth of rime, glaze, icicles and wet snow on structures. *Philos. Trans. R. Soc. A Math. Phys. Eng. Sci.* **2000**, *358*, 2913–2939, doi:10.1098/rsta.2000.0690.
75. Amendola, A.; Mingione, G. On the problem of icing for modern civil aircraft. *Air Sp. Eur.* **2001**, *3*, 214–217, doi:https://doi.org/10.1016/S1290-0958(01)90098-X.
76. Cebeci, T.; Kafyeke, F. Aircraft icing. *Annu. Rev. Fluid Mech.* **2003**, *35*, 11–21, doi:10.1146/annurev.fluid.35.101101.161217.
77. Kraj, A.G.; Bibeau, E.L. Phases of icing on wind turbine blades characterized by ice accumulation. *Renew. Energy* **2010**, *35*, 966–972, doi:https://doi.org/10.1016/j.renene.2009.09.013.
78. Giuseppe Mingione, M.B. Flight in icing conditions. **2010**, 188.
79. Varanasi, K.K.; Deng, T.; Smith, J.D.; Hsu, M.; Bhate, N. Frost

formation and ice adhesion on superhydrophobic surfaces. *Appl. Phys. Lett.* **2010**, *97*, doi:10.1063/1.3524513.

80. Cao, L.; Jones, A.K.; Sikka, V.K.; Wu, J.; Gao, D. Anti-Icing Superhydrophobic Coatings. *Langmuir* **2009**, *25*, 12444–12448, doi:10.1021/la902882b.
81. He, M.; Wang, J.; Li, H.; Song, Y. Super-hydrophobic surfaces to condensed micro-droplets at temperatures below the freezing point retard ice/frost formation. *Soft Matter* **2011**, doi:10.1039/c0sm01504k.
82. Zhang, Q.; Jin, B.; Wang, B.; Fu, Y.; Zhan, X.; Chen, F. Fabrication of a Highly Stable Superhydrophobic Surface with Dual-Scale Structure and Its Antifrosting Properties. *Ind. Eng. Chem. Res.* **2017**, doi:10.1021/acs.iecr.6b04650.
83. Lynch, F.T.; Khodadoust, A. Effects of ice accretions on aircraft aerodynamics. *Prog. Aerosp. Sci.* 2001.
84. Song, J.; Zhao, D.; Han, Z.; Xu, W.; Lu, Y.; Liu, X.; Liu, B.; Carmalt, C.J.; Deng, X.; Parkin, I.P. Super-robust superhydrophobic concrete. *J. Mater. Chem. A* **2017**, doi:10.1039/c7ta03526h.
85. Zheng, S.; Li, C.; Fu, Q.; Hu, W.; Xiang, T.; Wang, Q.; Du, M.; Liu, X.; Chen, Z. Development of stable superhydrophobic coatings on aluminum surface for corrosion-resistant, self-cleaning, and anti-icing applications. *Mater. Des.* **2016**, doi:10.1016/j.matdes.2015.12.155.
86. Ganne, A.; Lebed, V.O.; Gavrilov, A.I. Combined wet chemical etching and anodic oxidation for obtaining the superhydrophobic meshes with anti-icing performance. *Colloids Surfaces A Physicochem.*

Eng. Asp. **2016**, doi:10.1016/j.colsurfa.2016.04.019.

87. Zhang, Y.; Anim-Danso, E.; Bekele, S.; Dhinojwala, A. Effect of Surface Energy on Freezing Temperature of Water. *ACS Appl. Mater. Interfaces* **2016**, doi:10.1021/acsami.6b02094.
88. Boinovich, L.; Emelyanenko, A.M.; Korolev, V. V.; Pashinin, A.S. Effect of wettability on sessile drop freezing: When superhydrophobicity stimulates an extreme freezing delay. *Langmuir* **2014**, doi:10.1021/la403796g.
89. Ou, J.F.; Shi, Q.W.; Wang, Z. Le; Wang, F.J.; Xue, M.S.; Li, W.; Yan, G.L. Sessile droplet freezing and ice adhesion on aluminum with different surface wettability and surface temperature. *Sci. China Physics, Mech. Astron.* **2015**, doi:10.1007/s11433-015-5646-y.
90. Rahimi, M.; Afshari, A.; Thormann, E. Effect of Aluminum Substrate Surface Modification on Wettability and Freezing Delay of Water Droplet at Subzero Temperatures. *ACS Appl. Mater. Interfaces* **2016**, doi:10.1021/acsami.6b02321.
91. Arianpour, F.; Farzaneh, M.; Kulinich, S.A. Hydrophobic and ice-retarding properties of doped silicone rubber coatings. *Appl. Surf. Sci.* **2013**, doi:10.1016/j.apsusc.2012.11.042.
92. Liu, Y.; Li, X.; Jin, J.; Liu, J.; Yan, Y.; Han, Z.; Ren, L. Anti-icing property of bio-inspired micro-structure superhydrophobic surfaces and heat transfer model. *Appl. Surf. Sci.* **2017**, *400*, 498–505, doi:10.1016/j.apsusc.2016.12.219.
93. Yue, X.; Liu, W.; Wang, Y. Freezing delay, frost accumulation and

droplets condensation properties of micro- or hierarchically-structured silicon surfaces. *Int. J. Heat Mass Transf.* **2018**, *126*, 442–451, doi:10.1016/j.ijheatmasstransfer.2018.04.165.

94. Guo, P.; Zheng, Y.; Wen, M.; Song, C.; Lin, Y.; Jiang, L. Icephobic/Anti-Icing Properties of Micro/Nanostructured Surfaces. *Adv. Mater.* **2012**, *24*, 2642–2648, doi:10.1002/adma.201104412.
95. Chen, J.; Dou, R.; Cui, D.; Zhang, Q.; Zhang, Y.; Xu, F.; Zhou, X.; Wang, J.; Song, Y.; Jiang, L. Robust prototypical anti-icing coatings with a self-lubricating liquid water layer between ice and substrate. *ACS Appl. Mater. Interfaces* **2013**, doi:10.1021/am401004t.
96. Macner, A.M.; Daniel, S.; Steen, P.H. Condensation on surface energy gradient shifts drop size distribution toward small drops. *Langmuir* **2014**, doi:10.1021/la404057g.
97. Dou, R.; Chen, J.; Zhang, Y.; Wang, X.; Cui, D.; Song, Y.; Jiang, L.; Wang, J. Anti-icing coating with an aqueous lubricating layer. *ACS Appl. Mater. Interfaces* **2014**, doi:10.1021/am501252u.
98. Coady, M.J.; Wood, M.; Wallace, G.Q.; Nielsen, K.E.; Kietzig, A.M.; Lagugné-Labarthet, F.; Ragogna, P.J. Icephobic Behavior of UV-Cured Polymer Networks Incorporated into Slippery Lubricant-Infused Porous Surfaces: Improving SLIPS Durability. *ACS Appl. Mater. Interfaces* **2018**, doi:10.1021/acsami.7b14433.
99. Wei, C.; Jin, B.; Zhang, Q.; Zhan, X.; Chen, F. Anti-icing performance of super-wetting surfaces from icing-resistance to ice-phobic aspects: Robust hydrophobic or slippery surfaces. *J. Alloys Compd.* **2018**,

doi:10.1016/j.jallcom.2018.06.041.

100. Golovin, K.; Kobaku, S.P.R.; Lee, D.H.; DiLoreto, E.T.; Mabry, J.M.; Tuteja, A. Designing durable icephobic surfaces. *Sci. Adv.* **2016**, *2*, doi:10.1126/sciadv.1501496.

101. Yuan, Y.; Lee, T.R. Contact angle and wetting properties. *Springer Ser. Surf. Sci.* **2013**, doi:10.1007/978-3-642-34243-1_1.

102. Hao, P.; Lv, C.; Zhang, X. Freezing of sessile water droplets on surfaces with various roughness and wettability. *Appl. Phys. Lett.* **2014**, doi:10.1063/1.4873345.

103. Zeng, X.; He, M.; Li, H.; Wang, J.; Song, Y.; Jiang, L. Investigating the adhesion of water droplets at low temperatures. *Langmuir* **2011**, doi:10.1021/la2036136.

104. Maitra, T.; Tiwari, M.K.; Antonini, C.; Schoch, P.; Jung, S.; Eberle, P.; Poulikakos, D. On the nanoengineering of superhydrophobic and impalement resistant surface textures below the freezing temperature. *Nano Lett.* **2014**, *14*, 172–182, doi:10.1021/nl4037092.

105. Meuler, A.J.; Smith, J.D.; Varanasi, K.K.; Mabry, J.M.; McKinley, G.H.; Cohen, R.E. Relationships between water wettability and ice adhesion. *ACS Appl. Mater. Interfaces* **2010**, *2*, 3100–3110, doi:10.1021/am1006035.

106. Gao, L.; McCarthy, T.J. Teflon is hydrophilic. Comments on definitions of hydrophobic, shear versus tensile hydrophobicity, and wettability characterization. *Langmuir* **2008**, doi:10.1021/la8014578.

107. Ling, E.J.Y.; Uong, V.; Renault-Crispo, J.S.; Kietzig, A.M.; Servio, P.

Reducing Ice Adhesion on Nonsmooth Metallic Surfaces: Wettability and Topography Effects. *ACS Appl. Mater. Interfaces* **2016**, doi:10.1021/acsami.6b00187.

108. Wei, C.; Jin, B.; Zhang, Q.; Zhan, X.; Chen, F. Anti-icing performance of super-wetting surfaces from icing-resistance to ice-phobic aspects: Robust hydrophobic or slippery surfaces. *J. Alloys Compd.* **2018**, *765*, 721–730, doi:10.1016/j.jallcom.2018.06.041.
109. Subramanyam, S.B.; Rykaczewski, K.; Varanasi, K.K. Ice adhesion on lubricant-impregnated textured surfaces. *Langmuir* **2013**, *29*, 13414–13418, doi:10.1021/la402456c.
110. Irajizad, P.; Hasnain, M.; Farokhnia, N.; Sajadi, S.M.; Ghasemi, H. Magnetic slippery extreme icephobic surfaces. *Nat. Commun.* **2016**, *7*, 1–7, doi:10.1038/ncomms13395.
111. Chen, J.; Li, K.; Wu, S.; Liu, J.; Liu, K.; Fan, Q. Durable Anti-Icing Coatings Based on Self-Sustainable Lubricating Layer. *ACS Omega* **2017**, doi:10.1021/acsomega.7b00359.
112. Sarshar, M.A.; Swarctz, C.; Hunter, S.; Simpson, J.; Choi, C.H. Effects of contact angle hysteresis on ice adhesion and growth on superhydrophobic surfaces under dynamic flow conditions. *Colloid Polym. Sci.* **2013**, *291*, 427–435, doi:10.1007/s00396-012-2753-4.
113. Mishchenko, L.; Hatton, B.; Bahadur, V.; Taylor, J.A.; Krupenkin, T.; Aizenberg, J. Design of ice-free nanostructured surfaces based on repulsion of impacting water droplets. *ACS Nano* **2010**, *4*, 7699–7707, doi:10.1021/nn102557p.

114. Khedir, K.R.; Kannarpady, G.K.; Ishihara, H.; Woo, J.; Asar, M.P.; Ryerson, C.; Biris, A.S. Temperature-dependent bouncing of super-cooled water on teflon-coated superhydrophobic tungsten nanorods. *Appl. Surf. Sci.* **2013**, *279*, 76–84, doi:10.1016/j.apsusc.2013.04.038.
115. TADANAGA, K.; IWAMI, T.; MINAMI, T.; TOHGE, N. Microstructure of Al2O3 Xerogels and Aerogels from Aluminum-tri-sec-Butoxide Modified with Ethylacetoacetate. *J. Ceram. Soc. Japan* **1995**, doi:10.2109/jcersj.103.582.
116. Tadanaga, K.; Katata, N.; Minami, T. Super-water-repellent Al2O3 coating films with high transparency. *J. Am. Ceram. Soc.* **1997**, doi:10.1111/j.1151-2916.1997.tb02943.x.
117. Uchihashi, H.; Tohge, N.; Minami, T. Preparation of amorphous Al2O3 thin films from stabilized Al-alkoxides by the sol-gel method. *Nippon Seramikkusu Kyokai Gakujutsu Ronbunshi/Journal Ceram. Soc. Japan* **1989**, doi:10.2109/jcersj.97.396.
118. Jung, S.; Dorrestijn, M.; Raps, D.; Das, A.; Megaridis, C.M.; Poulikakos, D. Are superhydrophobic surfaces best for icephobicity? *Langmuir* **2011**, *27*, 3059–3066, doi:10.1021/la104762g.
119. Verho, T.; Bower, C.; Andrew, P.; Franssila, S.; Ikkala, O.; Ras, R.H.A. Mechanically Durable Superhydrophobic Surfaces. *Adv. Mater.* **2011**, *23*, 673–678, doi:10.1002/adma.201003129.
120. Liu, X.; Niu, C.; Zhen, X.; Wang, J.; Su, X. Novel approach for synthesis of boehmite nanostructures and their conversion to aluminum oxide nanostructures for remove Congo red. *J. Colloid*

Interface Sci. **2015**, doi:10.1016/j.jcis.2015.04.037.

121. Brinker, C.J.; Frye, G.C.; Hurd, A.J.; Ashley, C.S. Fundamentals of sol-gel dip coating. *Thin Solid Films* **1991**, doi:10.1016/0040-6090(91)90158-T.
122. Wang, S.D.; Luo, S.S. Fabrication of transparent superhydrophobic silica-based film on a glass substrate. *Appl. Surf. Sci.* **2012**, doi:10.1016/j.apsusc.2012.02.032.
123. Wang, X.; Zhao, X.; Jing, C.; Tao, H.; Han, J. Effects of nitric acid concentration on the stability of alumina sols. *J. Wuhan Univ. Technol. Mater. Sci. Ed.* **2006**, doi:10.1007/BF02861483.
124. Liu, H.; Chen, J.; Ge, H. Chemical modification of ethylacetoacetate with ASB in aqueous medium. *J. Wuhan Univ. Technol. Mater. Sci. Ed.* **2009**, doi:10.1007/s11595-009-1068-x.
125. Xu, Q.F.; Wang, J.N.; Sanderson, K.D. Organic-inorganic composite nanocoatings with superhydrophobicity, good transparency, and thermal stability. *ACS Nano* **2010**, doi:10.1021/nn901581j.
126. Sanchez, J.; McCormick, A. Kinetic and thermodynamic study of the hydrolysis of silicon alkoxides in acidic alcohol solutions. *J. Phys. Chem.* **1992**, doi:10.1021/j100201a051.
127. Qiao, Z.A.; Zhang, L.; Guo, M.; Liu, Y.; Huo, Q. Synthesis of mesoporous silica nanoparticles via controlled hydrolysis and condensation of silicon alkoxide. *Chem. Mater.* **2009**, doi:10.1021/cm901335k.
128. Loy, D.A.; Mather, B.; Straumanis, A.R.; Baugher, C.; Schneider, D.A.;

Sanchez, A.; Shea, K.J. Effect of pH on the gelation time of hexylene-bridged polysilsesquioxanes. *Chem. Mater.* **2004**, doi:10.1021/cm0498640.

129. *Transformation of Organometallics into Common and Exotic Materials: Design and Activation*; 1988;
130. Wan, Y.; Yu, S.H. Polyelectrolyte controlled large-scale synthesis of hollow silica spheres with tunable sizes and wall thicknesses. *J. Phys. Chem. C* **2008**, doi:10.1021/jp710990b.
131. Sheen, Y.C.; Huang, Y.C.; Liao, C.S.; Chou, H.Y.; Chang, F.C. New approach to fabricate an extremely super-amphiphobic surface based on fluorinated silica nanoparticles. *J. Polym. Sci. Part B Polym. Phys.* **2008**, doi:10.1002/polb.21535.
132. Antonelli, D.M.; Ying, J.Y. Synthesis of Hexagonally Packed Mesoporous TiO2 by a Modified Sol–Gel Method. *Angew. Chemie Int. Ed. English* **1995**, doi:10.1002/anie.199520141.
133. Wang, C.C.; Ying, J.Y. Sol-gel synthesis and hydrothermal processing of anatase and rutile titania nanocrystals. *Chem. Mater.* **1999**, doi:10.1021/cm990180f.
134. Shane, M.; Mecartney, M.L. Sol-gel synthesis of zirconia barrier coatings. *J. Mater. Sci.* **1990**, doi:10.1007/BF01045347.
135. Kamalasanan, M.N.; Chandra, S. Sol-gel synthesis of ZnO thin films. *Thin Solid Films* **1996**, doi:10.1016/S0040-6090(96)08864-5.
136. Mahadik, S.A.; Kavale, M.S.; Mukherjee, S.K.; Rao, A.V. Transparent superhydrophobic silica coatings on glass by sol-gel method. *Appl.*

Surf. Sci. **2010**, doi:10.1016/j.apsusc.2010.06.062.

137. Phelps, C.F. Dynamic light scattering, with application to chemistry, biology and physics. *Biochem. Educ.* **1977**, doi:10.1016/0307-4412(77)90025-5.
138. Goldburg, W.I. Dynamic light scattering Dynamic light scattering. *Am. J. Phys.* **1999**.
139. Landau, L.; Levich, B. Dragging of a Liquid by a Moving Plate. In *Dynamics of Curved Fronts*; 1988.
140. Faustini, M.; Louis, B.; Albouy, P.A.; Kuemmel, M.; Grosso, D. Preparation of sol-gel films by dip-coating in extreme conditions. *J. Phys. Chem. C* **2010**, doi:10.1021/jp9114755.
141. Grosso, D. How to exploit the full potential of the dip-coating process to better control film formation. *J. Mater. Chem.* **2011**, doi:10.1039/c1jm12837j.
142. Kavale, M.S.; Mahadik, D.B.; Parale, V.G.; Wagh, P.B.; Gupta, S.C.; Rao, A.V.; Barshilia, H.C. Optically transparent, superhydrophobic methyltrimethoxysilane based silica coatings without silylating reagent. *Appl. Surf. Sci.* **2011**, doi:10.1016/j.apsusc.2011.08.023.
143. Phani, A.R.; Santucci, S. Evaluation of structural and mechanical properties of aluminum oxide thin films deposited by a sol-gel process: Comparison of microwave to conventional anneal. *J. Non. Cryst. Solids* **2006**, doi:10.1016/j.jnoncrysol.2006.06.013.
144. Nass, R.; Schmidt, H. Synthesis of an alumina coating from chelated aluminium alkoxides. *J. Non. Cryst. Solids* **1990**, doi:10.1016/0022-

3093(90)90153-D.

145. Kurisu, T.; Kozuka, H. Effects of heating rate on stress evolution in alkoxide-derived silica gel-coating films. *J. Am. Ceram. Soc.* **2006**, doi:10.1111/j.1551-2916.2006.01107.x.

146. Yahata, R.; Kozuka, H. Stress evolution of sol-gel-derived silica coatings during heating: The effects of the chain length of alcohols as solvents. *Thin Solid Films* **2009**, doi:10.1016/j.tsf.2008.08.117.

147. Kozuka, H. Stress evolution on gel-to-ceramic thin film conversion. In Proceedings of the Journal of Sol-Gel Science and Technology; 2006.

148. Malavasi, I.; Veronesi, F.; Caldarelli, A.; Zani, M.; Raimondo, M.; Marengo, M. Is a knowledge of surface topology and contact angles enough to define the drop impact outcome? *Langmuir* **2016**, doi:10.1021/acs.langmuir.6b01117.

149. Zhou, R. -S; Snyder, R.L. Structures and transformation mechanisms of the η, γ and θ transition aluminas. *Acta Crystallogr. Sect. B* **1991**, doi:10.1107/S0108768191002719.

150. Gauss, C.F.; Gauss, C.F. Principia generalia theoriae figurae fluidorum in statu aequilibrii. In *Werke*; 1877.

151. Milne, A.J.B.; Amirfazli, A. The Cassie equation: How it is meant to be used. *Adv. Colloid Interface Sci.* 2012.

152. Herminghaus, S. Roughness-induced non-wetting. *Europhys. Lett.* **2000**, doi:10.1209/epl/i2000-00418-8.

153. Gao, L.; McCarthy, T.J. How Wenzel and Cassie were wrong. *Langmuir* **2007**, doi:10.1021/la062634a.

154. Lipowsky, R.; Lenz, P.; Swain, P.S. Wetting and dewetting of structured and imprinted surfaces. *Colloids Surfaces A Physicochem. Eng. Asp.* **2000**, doi:10.1016/S0927-7757(99)00321-0.
155. Bico, J.; Thiele, U.; Quéré, D. Wetting of textured surfaces. In Proceedings of the Colloids and Surfaces A: Physicochemical and Engineering Aspects; 2002.
156. Deng, T.; Varanasi, K.K.; Hsu, M.; Bhate, N.; Keimel, C.; Stein, J.; Blohm, M. Nonwetting of impinging droplets on textured surfaces. *Appl. Phys. Lett.* **2009**, doi:10.1063/1.3110054.
157. Surface energy relations in liquid/solid systems I. The adhesion of liquids to solids and a new method of determining the surface tension of liquids. *Proc. R. Soc. London. Ser. A. Math. Phys. Sci.* **1942**, doi:10.1098/rspa.1942.0031.
158. Neumann, A.W.; Good, R.J. Techniques of Measuring Contact Angles. In *Surface and Colloid Science*; 1979.
159. Mora, J.; García, P.; Muelas, R.; Agüero, A. Hard quasicrystalline coatings deposited by hvof thermal spray to reduce ice accretion in aero-structures components. *Coatings* **2020**, *10*, 1–22, doi:10.3390/coatings10030290.
160. Goswami, S.; Klaus, S.; Benziger, J. Wetting and absorption of water drops on nafion films. *Langmuir* **2008**, doi:10.1021/la800799a.
161. Raimondo, M.; Blosi, M.; Caldarelli, A.; Guarini, G.; Veronesi, F. Wetting behavior and remarkable durability of amphiphobic aluminum alloys surfaces in a wide range of environmental

conditions. *Chem. Eng. J.* **2014**, *258*, 101–109, doi:10.1016/j.cej.2014.07.076.

162. Motta, A.; Cannelli, O.; Boccia, A.; Zanoni, R.; Raimondo, M.; Caldarelli, A.; Veronesi, F. A mechanistic explanation of the peculiar amphiphobic properties of hybrid organic-inorganic coatings by combining XPS characterization and DFT modeling. *ACS Appl. Mater. Interfaces* **2015**, doi:10.1021/acsami.5b04376.
163. Kulinich, S.A.; Farhadi, S.; Nose, K.; Du, X.W. Superhydrophobic surfaces: Are they really ice-repellent? *Langmuir* **2011**, *27*, 25–29, doi:10.1021/la104277q.
164. Tsai, P.; Lammertink, R.G.H.; Wessling, M.; Lohse, D. Evaporation-triggered wetting transition for water droplets upon hydrophobic microstructures. *Phys. Rev. Lett.* **2010**, *104*, 2–3, doi:10.1103/PhysRevLett.104.116102.
165. McCarthy, M.; Gerasopoulos, K.; Enright, R.; Culver, J.N.; Ghodssi, R.; Wang, E.N. Biotemplated hierarchical surfaces and the role of dual length scales on the repellency of impacting droplets. *Appl. Phys. Lett.* **2012**, *100*, 1–6, doi:10.1063/1.4729935.
166. Karmouch, R.; Ross, G.G. Experimental study on the evolution of contact angles with temperature near the freezing point. *J. Phys. Chem. C* **2010**, *114*, 4063–4066, doi:10.1021/jp911211m.
167. Lo, C.W.; Sahoo, V.; Lu, M.C. Control of Ice Formation. *ACS Nano* **2017**, *11*, 2665–2674, doi:10.1021/acsnano.6b07348.
168. Bahadur, V.; Mishchenko, L.; Hatton, B.; Taylor, J.A.; Aizenberg, J.;

Krupenkin, T. Predictive model for ice formation on superhydrophobic surfaces. *Langmuir* **2011**, *27*, 14143–14150, doi:10.1021/la200816f.

169. Smith, J.D.; Dhiman, R.; Anand, S.; Reza-Garduno, E.; Cohen, R.E.; McKinley, G.H.; Varanasi, K.K. Droplet mobility on lubricant-impregnated surfaces. *Soft Matter* **2013**, *9*, 1772–1780, doi:10.1039/C2SM27032C.
170. Kralchevsky, P.A.; Nagayama, K. Capillary interactions between particles bound to interfaces, liquid films and biomembranes. *Adv. Colloid Interface Sci.* 2000.
171. Dzyaloshinskii, I.E.; Lifshitz, E.M.; Pitaevskii, L.P. The general theory of van der Waals forces. *Adv. Phys.* **1961**, doi:10.1080/00018736100101281.
172. Hamaker, H.C. The London-van der Waals attraction between spherical particles. *Physica* **1937**, doi:10.1016/S0031-8914(37)80203-7.
173. Owais, A.; Smith-Palmer, T.; Gentle, A.; Neto, C. Influence of long-range forces and capillarity on the function of underwater superoleophobic wrinkled surfaces. *Soft Matter* **2018**, doi:10.1039/c8sm00709h.